TECHNISCHE UNIVERSITÄT WIEN
Vienna University of Technology

Diplomarbeit

AbinitioDΓA for $SrVO_3$: Effects of non-local interactions, temperature and dimensionality

ausgeführt am Institut für Festkörperphysik
der Technischen Universität Wien

unter der Anleitung von
Univ.Ass. Dr. Jan Tomczak
Univ.Prof. Dr. Karsten Held

durch
Matthias Pickem, BSc
Matrikelnummer: 01125476

Breitenbrunn, März 2018

Deutsche Kurzfassung

Die vorliegende Diplomarbeit befasst sich mit starken elektronischen Korrelationen in Materialien, sowie Modellen und Methoden welche diese effektiv beschreiben. Materialien mit starken Korrelationen zeigen unterschiedlichste Phänomene, wie zum Beispiel den Mott Metall-Isolator-Übergang, Supraleitung oder riesige Massen in Schwere-Fermionen-Verbindungen. Aufgrund des wissenschaftlichen Fortschritts der letzten Zeit ist die Hoffnung gewachsen, dass eines Tages die derzeit vorhandenen Technologien (Halbleiterphysik etc.) durch Anwendungen ersetzt oder verbessert werden können, welche die genannten Korrelationseffekte ausnutzen. Die vielversprechendste Materialgruppe in diesem Zusammenhang sind die sogenannten Übergangsmetalloxide, welche ein zentrales Thema dieser Arbeit sind.

Um die dazu relevante Physik zu beschreiben, wird im ersten Teil dieser Arbeit der Übergang vom Vielteilchenproblem in erster Quantisierung zum Formalismus der Greenschen Funktionen gebildet. Mit der dadurch entstehenden Methode der Feynman-Diagramme ist man in der Lage die moderne Elektronenstrukturmethode Dichtefunktional-Theorie (DFT) + Dynamische Molekularfeld-Theorie (DMFT) einzuführen. Diese ermöglicht es lokale Korrelationseffekte zu beschreiben. Diese Lokalität ist eines der Merkmale von DFT+DMFT. Effekte nicht-lokaler Korrelationen spielen jedoch eine wichtige Rolle in zweidimensionalen Strukturen (z.B. in dünnen Schichten) oder in der Nähe von Phasenübergängen. Zu diesem Zweck wurden in den vergangen Jahren mehrere Theorien und Methoden entwickelt, um DFT+DMFT formell zu erweitern. Diese Erweiterungen erlauben es sowohl lokale als auch nicht-lokale Korrelationen zu beschreiben. Die Dynamische Vertex Approximation (DΓA) ist eine dieser Methoden, welche DMFT diagrammatisch erweitert, und bildet den Schwerpunkt dieser Arbeit.

Im zweiten Teil dieser Arbeit wird mit DΓA ein Standardbeispiel stark korrelierter Materialien, Strontium-Vanadat ($SrVO_3$), untersucht. Genauer wird der Einfluss der Temperatur und nicht-lokaler Wechselwirkungen in „bulk“ $SrVO_3$, als auch die Effekte von reduzierter Dimensionalität, untersucht. Letzteres basiert auf jüngsten experimentellen und theoretischen Untersuchungen von zweilagigem $SrVO_3$ auf einem Strontium-Titanat ($SrTiO_3$) Substrat, das potenziell als ein sogenannter „Mott Transistor“ verwendet werden kann. Der beteiligte Mott Metall-Isolator-Übergang kann durch unterschiedliche externe Einflüsse, wie zum Beispiel einer Gate-Spannung, Druck oder Temperatur ausgelöst werden. Die DΓA Ergebnisse für bulk $SrVO_3$ zeigen, dass die nicht-lokalen Effekte der Symmetrie der Fermi-Fläche folgen. Die vielversprechenden Ergebnisse für das genannte Schichtsystem können als Grundlage für zukünftige Untersuchungen von dünnen Schichten oder Heterostrukturen verwendet werden. Die divergierenden Suszeptibilitäten indizieren einen Übergang in eine geordnete Phase im isolierenden Bereich.

Abstract

Strong electronic correlations have been in the focus of solid state research for quite some time. Many interesting phenomena such as the Mott metal-to-insulator transition, superconductivity (both conventional and unconventional) or heavy-fermion systems can only be explained when taking correlation effects into account. In this regard there has always been the hope that applications exploiting these correlation effects will one day replace or enhance current technologies. One of the most promising group of materials with respect to applicability are transition metal oxides which are at the center of this thesis.

In order to be able to describe the involved physics we will, in the first part of this thesis, construct the bridge from the many-body problem in first quantization to the Green's function formalism and subsequently Feynman diagrammatic. With this formalism we are able to introduce the state-of-the-art density functional theory (DFT) + dynamical mean-field theory (DMFT) approach both from a physical point of view and, more importantly, diagrammatically. This technique allows for an accurate description of genuine (local) correlation effects. However due to the underlying mean-field approach in the spatial domain non-local effects are out of its reach. These non-local correlations play an essential role in two-dimensional structures (e.g. ultra-thin films) or near phase transitions. For this reason many theories and techniques have been developed which extend DMFT to capture both the local correlations of DMFT and non-local correlations beyond. The dynamical vertex approximation (DΓA) represents one of the diagrammatic extensions of DMFT and will be our main focus point in this thesis.

With it, in the second part of this thesis, we will further investigate a common testbed material used in electronic structure calculations, namely strontium vanadate ($SrVO_3$). More specifically we will study the effects of temperature and non-local interactions in bulk $SrVO_3$ as well as the effects of the previously mentioned reduced dimensionality. The latter is based on recent findings that two-layered $SrVO_3$ on a substrate of strontium titanate ($SrTiO_3$) could be potentially used as a so-called 'Mott transistor' where the involved Mott metal-to-insulator transition can be triggered via different external perturbations, such as a gate voltage, pressure or temperature.

Contents

List of publications

- A. Galler, J. Kaufmann, P. Gunacker, M. Pickem, P. Thunström, J.M. Tomczak and K. Held, *Towards ab initio Calculations with the Dynamical Vertex Approximation*, Journal of the Physical Society of Japan, **87**, 041004 (2017).

Preprint:

- A. Galler, P. Thunström, J. Kaufmann, M. Pickem, J.M. Tomczak and K. Held, *The AbinitioDΓA Project v1.0: Non-local correlations beyond and susceptibilities within dynamical mean-field theory*, https://arxiv.org/abs/1710.06651.

The publications regarding non-local interactions as well as ultra-thin $SrVO_3$ are in preparation (Pickem et al.).

Introduction

Scope

In recent history massive progress has been made to further the understanding of many puzzles in the area of solid state physics. Many theories, most of which are already taken for granted today, were just developed over the last 60 years. BCS-theory was for example conceived by Bardeen, Cooper and Schrieffer in 1957 [1] (Nobel prize in physics in 1972). The Fermi-liquid theory was first developed by Landau in the same year [2] and first applied by Abrikosov and Khalatnikov in 1959 in the context of liquid ^{3}He [3]. Hohenberg and Kohn invented the building blocks of density functional theory (DFT) in 1964 [4] which was further developed by Kohn and Sham one year later in 1965 [5] (Nobel prize in chemistry in 1998). Kohn-Sham DFT was able to describe many of the until then deemed impossible problems and nowadays builds the de facto working horse of almost all of today's electronic structure calculations. Due to its effective one-particle nature (see chapter 1.2) DFT works well for most main group elements, however it is not equipped to describe electronic correlation effects found in many side group elements. These are composed of partially filled d- or f-orbitals (see Fig. 1) which are naturally more localized, thus exhibiting correlation effects.[1] Around 1990 the dynamical mean-field theory (DMFT) [6, 7] was developed which is capable to solve many problems for which DFT fails, most prominently the Mott metal-to-insulator transition (MIT). However while highly successful, the increasing amount of computational power nowadays allows to even overcome the limits of DMFT, by including non-local correlations. Again the mean-field approach (this time only in the spatial domain) is a too strong simplification in specific cases, e.g. for low-dimensions or near second order phase transitions. Presently many theoreticians try to overcome DMFT's problems by formally extending it. Cluster formulations [8, 9] allow the inclusion of short-range spatial correlation effects, while extensions on a diagrammatic level [10, 11] allow the inclusion of correlation effects on all length scales. These diagrammatic extensions, more specifically the application of the dynamical vertex approximation (DΓA), will be the focus of the present thesis.

[1] The locality of, e.g., the $3d$ or $4f$ elements originates from the involved $l = 3$ and $l = 4$ orbitals respectively. The orthogonality to all fully occupied orbitals (aufbau principle) is assumed by the azimuthal quantum number, allowing the radial part of the orbital to be nodeless and thus more localized.

Motivation

Over the last couple of years metal oxides, metal oxide heterostructures as well as ultra-thin metal oxide films were a major focus point in both theoretical and experimental research. These materials, which include e.g. $SrVO_3$, $SrRuO_3$, $CaTiO_3$, etc., have been studied extensively and showed a wide variety of interesting effects. Colossal magnetoresistance (CMR) in manganese oxide compounds [12], thermoelectric effects in perovskite structures [13], the description of quantum spin liquids [14], superconducting states as found in bismuth strontium calcium copper oxides (BSSCO) [15], the creation of a two-dimensional electron gas with high mobility at the interface of two band insulators, $LaAlO_3$ and $SrTiO_3$ [16], thin VO_2 films which 'intelligently' regulate and utilize solar radiation [17], $LaVO_3$ as efficient solar cell [18, 19], etc., to only name a few effects and examples. So far however non-local correlations were neglected in the theoretical description of most of these effects.[2] These possible non-local corrections in turn represent our starting point. Proceeding from [20] we will further investigate bulk $SrVO_3$ as well as study non-local effects in ultra-thin $SrVO_3$ films consisting only of two layers. The latter represents a way to confound electronics with the physics of metal oxides via the help of the already mentioned Mott metal-to-insulator transition [21].

Outline

For that matter, in chapter 1, we will start from the ab initio solid state description, namely the many-body Hamiltonian in first quantization. Based on the Born-Oppenheimer approximation, DFT will be discussed in a more technical manner from which the bridge to DMFT will be constructed with the help of model Hamiltonians. The formalism necessary to describe DMFT and all its extensions will be discussed in chapter 2, where we introduce the DΓA approach including its implementations, namely parquetDΓA and ladderDΓA. Based on the ladderDΓA approach present in `AbinitioDΓA` [20, 22, 23, 24], we will discuss results for the well-known testbed material $SrVO_3$ (shown in Fig. 2). To this end calculations for bulk $SrVO_3$ will be illustrated in chapter 3 while calculations for two-layered $SrVO_3$ on top of a $SrTiO_3$ substrate will be illustrated in chapter 4. Finally in chapter 5, a summarized discussion with an outlook on future development and applications will be presented.

[2] Superconductivity, described by BCS-theory, obviously being the major exception where one deals with macroscopically sized non-local effects (Cooper pairs).

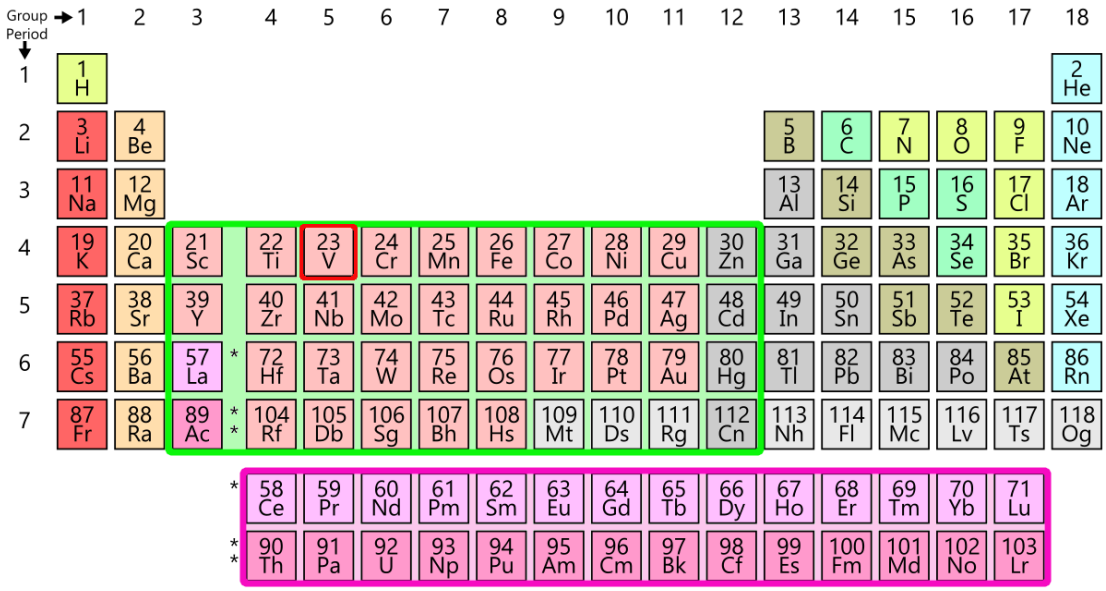

Figure 1: Periodic table with elements containing partially filled d- and f- orbitals highlighted in green and pink, respectively. The former are usually denoted as transition metals (elements) which originates from the fact that each row in the block can be seen as a transition series of elements which, according to their position, gain an increasing number of d-electrons (e.g. scandium $[Ar]3d^14s^2$ to zinc $[Ar]3d^{10}4s^2$). Vanadium ${}^{51}_{23}V$ ($[Ar]3d^34s^2$), as it is the central character of this thesis, is additionally highlighted in red. Adapted and modified from [25].

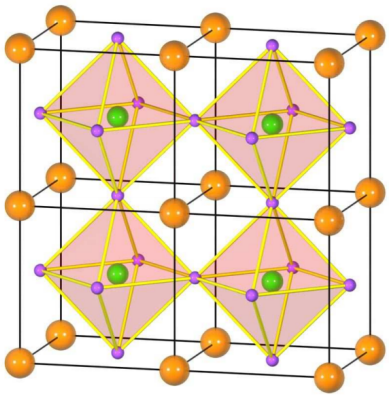

Figure 2: Perovskite crystal structure of the transition metal oxide strontium vanadate ($SrVO_3$). The name perovskite originates from calcium titanate ($CaTiO_3$) which lends its name to all other crystals with the same kind of structure [26]. The spheres placed on the implied cubic grid represent vanadium (orange) which together with oxygen (purple) and strontium (green) build the characteristic perovskite structure. Adapted from [27].

1 Basics of solid state physics

1.1 Many-body Hamiltonian

Solving the full description of an interacting electron system within a realistic environment is an utopian endeavor. In first quantization this problem reads [28]

$$\hat{H}_{tot} = \underbrace{-\sum_{\alpha}^{N_n} \frac{\hbar^2 \Delta_\alpha}{2M_\alpha} + \frac{1}{2}\sum_{\alpha\neq\alpha'} \frac{Z_\alpha Z_{\alpha'} e^2}{|\mathbf{R}_\alpha - \mathbf{R}_{\alpha'}|}}_{\hat{H}_n} \underbrace{- \sum_{\alpha,\mu} \frac{Z_\alpha e^2}{\left|\mathbf{R}_\alpha - \mathbf{r}_\mu\right|}}_{\hat{V}_{ne}} \underbrace{- \sum_{\mu}^{N_e} \frac{\hbar^2 \Delta_\mu}{2m} + \frac{1}{2}\sum_{\mu\neq\mu'} \frac{e^2}{\left|\mathbf{r}_\mu - \mathbf{r}_{\mu'}\right|}}_{\hat{H}_e}. \quad (1.1)$$

This equation, in combination with lowest-order relativistic corrections (introduction of spin and therefore magnetism), represents the (complete) theory of atomic and condensed-matter physics, as well as chemistry. Solving Eq. (1.1) within typical three dimensional crystals , which consist of approximately 10^{23} electrons per cubic centimeter, is however impossible. In order to transform this impossible task into a possible one, we have to introduce major simplifications and techniques which allow us to extract the information we are interested in. The latter is important because even if we had access to the exact solution, i.e. the many-body wave function, we would not be able to extract the information we desire. The first of many simplifications of this so-called *many-body-problem* is the Born-Oppenheimer approximation [29]. It is based on the fact that the masses of the particles in our system vary immensely. This results in different time scales for the electrons and nuclei involved. Due to their lower mass ($\frac{m_P}{m_e} \approx 1836$) electrons are much more agile and we are, in a good approximation, allowed to decouple the nuclei part $\hat{H}_n$ of Eq. (1.1) from the rest. We thus arrive at the electronic Hamiltonian

$$\hat{H}_{e,tot} = \hat{H}_e + \hat{V}_{ne}. \quad (1.2)$$

Here we interpret the nuclei-electron interaction $\hat{V}_{ne}$ as static external potential leaving us 'only' with an effective electron-electron Hamiltonian.[3] In this thesis we will restrict ourselves to this electronic part. The nuclei part however is far from boring and contains fascinating physics as well. It describes phonon excitations and their interactions with each other and the electrons involved. These processes are often required to get a satisfying model description of materials used in recent (theoretical and experimental) research.[4]

[3] This also means that the involved wave functions decouple, i.e. $|\Psi_{\text{full}}\rangle = |\Phi_{\text{electrons}}\rangle \times |\eta_{\text{nuclei}}\rangle$.

[4] Conventional superconductivity is for example described by an attractive, effective electron-electron interaction mediated by phonons.

1.2 Density functional theory

Due to the complexity of the remaining terms nothing else can be done but to introduce further simplifications. Typical introductory procedures include ignoring interactions altogether (Fermi gas) or implementing a rather simple self-consistent mean-field approach (Hartree or Hartree-Fock approximation) [30] where plane waves, products of one-electron wavefunctions, or antisymmetrized products of one-electron wavefunctions are used, respectively. However when trying to describe real materials this is not good enough. A major breakthrough in this regard was achieved by Hohenberg and Kohn in 1964 [4]. They were able to formulate theorems that create a one-to-one mapping between the ground state of an interacting system and a general density function. The theorems read as follows:
Theorem 1: The ground state energy of a system of *N indistinguishable* particles in an external potential is a unique functional of the particle density $\rho(r)$

$$E_0 = \min\{E[\rho(\mathbf{r})]\} = E[\rho_0(\mathbf{r})] \tag{1.3}$$

Theorem 2: This functional has its minimum with respect to a variation $\delta\rho(\mathbf{r})$ of the particle density at the ground state density.

$$\left.\frac{\delta E[\rho(\mathbf{r})]}{\delta\rho(\mathbf{r})}\right|_{\rho(\mathbf{r})=\rho_0(\mathbf{r})} = 0 \tag{1.4}$$

These theorems represent the building blocks of density functional theory (DFT). The basic idea within DFT is to separate the total energy functional in more simple terms which we are able to evaluate, namely

$$E[\rho] = \underbrace{T[\rho]}_{\text{kinetic energy}} + \underbrace{E_H[\rho]}_{\text{Hartree energy}} + \underbrace{V_{\text{ext}}[\rho]}_{\text{external potential}} + \underbrace{E_{\text{xc}}[\rho].}_{\text{exchange-correlation energy}} \tag{1.5}$$

There exist several methods that try to approach this functional with varying degrees of success. Orbital-free DFT for example tries to approximate the DFT energy functional and in particular the kinetic energy directly from the electron density using, e.g., the properties of a homogeneous electron gas (Thomas-Fermi approximation [31]). However even with further improvements (Thomas-Fermi-Dirac or von Weizsäcker approximation) the results are still too inaccurate for most applications. The major problems of orbital-free DFT were solved with Kohn-Sham DFT. Here an *artificial non-interacting electron system* is constructed whose ground-state density equals the one of the real interacting system. The density of this new system can simply be expressed by

$$\rho(\mathbf{r}) = \sum_i^N \Phi_i^*(\mathbf{r})\Phi_i(\mathbf{r}), \tag{1.6}$$

where Φ_i represent the eigenstates. Due to the simplicity of a non-interacting system we can evaluate the three largest contributions (kinetic energy, electro-static energy (Hartree energy) and energy of electrons in the external potential) explicitly. The rest, i.e. the energy from exchange and correlation effects, however must still be approximated. The most commonly used exchange-correlation potentials include the local density approximation (LDA)

$$E_{\mathrm{xc}}^{\mathrm{LDA}} = \int d^3r\, \rho(\mathbf{r}) \varepsilon_{\mathrm{xc}}^{\mathrm{LDA}}(\rho(\mathbf{r}))\,, \tag{1.7}$$

and the general gradient approximation (GGA)

$$E_{\mathrm{xc}}^{\mathrm{GGA}} = \int d^3r\, \rho(\mathbf{r}) \varepsilon_{\mathrm{xc}}^{\mathrm{GGA}}(\rho(\mathbf{r}), \nabla\rho(\mathbf{r}))\,, \tag{1.8}$$

in various parametrizations, such as PW91 [32] or PBE [33]. Other approximations which include, e.g., hybrid functionals such as B3LYP [34, 35], nonetheless also gained increasing popularity over the past. By minimizing the total energy functional with the constraint of orthogonal wave functions one arrives at the Kohn Sham equations [5] which have to be solved self-consistently:

$$\left[-\frac{\hbar^2}{2m}\Delta_i + v_{\mathrm{ext}} + e^2 \int \frac{\rho(\mathbf{r}')}{|\mathbf{r}_i - \mathbf{r}'|} d^3r' + \frac{\delta\varepsilon_{xc}}{\delta\rho(\mathbf{r})}\right] \Phi_i(\mathbf{r}) = \varepsilon_i \Phi_i(\mathbf{r}) \tag{1.9}$$

The solution of such an approach [36, 37, 38] provides the total energy of the system in the ground state. The individual eigenstate energies on the other hand are often interpreted as the electronic band-structure of our initial problem. However one has to keep in mind that these energies are, in fact, only auxiliary solutions of the converged eigenvalue equations and must therefore be treated with caution.

1.3 Wannierization

DFT, despite its many successes, still remains 'just' a more elaborate mean-field approach, at least, with the exchange-correlation potentials available. Due to the nature of such approaches they are not equipped to deal with effects of strong correlations, found in most of the more interesting materials. One of the biggest unsolved problems within DFT remained the Mott metal-to-insulator transition (MIT) [39, 40]. The effects responsible for such a behavior are beyond a static mean-field description and must therefore be dealt with through other techniques, more specifically many-body model Hamiltonians [41]. The typical Hubbard model used to describe these strong correlation effects reads

$$\hat{H}_{\mathrm{Hubbard}} = -t \sum_{\langle i,j\rangle\sigma} \hat{c}_{j\sigma}^{\dagger} \hat{c}_{i\sigma} + U \sum_i n_{i\uparrow} n_{i\downarrow} - \mu \sum_{i\sigma} n_{i\sigma}. \tag{1.10}$$

The first term describes electrons moving on a lattice (with the hopping parameter t) while the second term describes the on-site Coulomb interaction between two electrons, necessarily of opposite spins because of the Pauli principle. The last term originates from the grand canonical ensemble and allows the variation of the number of particles in the system via the chemical potential μ. The competition between delocalization (hopping) and localization (on-site interaction) allows this model to have deeply fascinating physics. To apply Hubbard type of models in the context of real materials one has to start off by rewriting Eq. (1.1) into its second quantization form. This reads

$$\hat{H} = \sum_{\sigma} \int d^3 r \hat{\psi}^{\dagger}_{\sigma}(\mathbf{r}) \left[-\frac{\hbar^2}{2m}\Delta + V(\mathbf{r}) \right] \hat{\psi}_{\sigma}(\mathbf{r}) + \frac{1}{2} \sum_{\sigma,\sigma'} \int d^3 r d^3 r' \hat{\psi}^{\dagger}_{\sigma}(\mathbf{r}) \hat{\psi}^{\dagger}_{\sigma'}(\mathbf{r}') \frac{e^2}{|\mathbf{r}-\mathbf{r}'|} \hat{\psi}_{\sigma'}(\mathbf{r}') \hat{\psi}_{\sigma}(\mathbf{r}), \tag{1.11}$$

where $\hat{\psi}^{(\dagger)}_{\sigma}(\mathbf{r})$ annihilates (creates) an electron at position $\mathbf{r}$ with spin σ. These field operator are built from the corresponding Bloch wave functions

$$\psi_{\mathbf{k},n}(\mathbf{r}) = e^{i\mathbf{k}\mathbf{r}} u_{\mathbf{k},n}(\mathbf{r}) \tag{1.12}$$

via

$$\hat{\psi}^{(\dagger)}_{\sigma}(\mathbf{r}) = \frac{V}{(2\pi)^3} \int_{\mathrm{BZ}} d^3 k \sum_{n} \psi^{(*)}_{\mathbf{k},n}(\mathbf{r})\, \hat{c}^{(\dagger)}_{\mathbf{k},n,\sigma}. \tag{1.13}$$

Here $\hat{c}^{(\dagger)}$ annihilates (creates) an electron with crystal momentum $\mathbf{k}$, spin σ and orbital n. The integration is done over the whole Brillouin zone (BZ) and the summation is done over all bands n. In order to get a description that is feasible in DMFT one has to introduce the so-called Wannier basis, as one has to define locality. The main idea is to do a basis transformation of an energetically localized basis (Bloch basis) obtained from DFT to a spatially localized Wannier basis. The transformation is done via

$$|\mathbf{R}n\rangle = \frac{V}{(2\pi)^3} \int_{BZ} d^3 k e^{-i\mathbf{k}\cdot\mathbf{R}} \sum_{m=1}^{J} U^{(\mathbf{k})}_{mn} |\psi_{m\mathbf{k}}\rangle \tag{1.14a}$$

$$w_{n\mathbf{R}}(\mathbf{r}) = \langle \mathbf{r}|\mathbf{R}n\rangle \tag{1.14b}$$

and the momentum-dependent unitary transformation matrices $U^{\mathbf{k}}_{mn}$ are, e.g., adjusted in order to minimize the functional [42]

$$\Omega = \sum_{n} \left[\langle \mathbf{0}n| \, r^2 \, |\mathbf{0}n\rangle - \langle \mathbf{0}n| \, \mathbf{r} \, |\mathbf{0}n\rangle \right], \tag{1.15}$$

which estimates the spatial spread of the Wannier functions. This new basis allows us then to rewrite Eq. (1.11) into

$$\hat{H} = -\sum_{\substack{\mathbf{R}_1,\mathbf{R}_2 \\ lm \\ \sigma}} t_{lm}(\mathbf{R}_1,\mathbf{R}_2)\hat{c}^\dagger_{\mathbf{R}_1 l\sigma}\hat{c}_{\mathbf{R}_2 m\sigma} + \frac{1}{2}\sum_{\substack{\mathbf{R}_1\mathbf{R}_2\mathbf{R}_3\mathbf{R}_4 \\ ll'mm' \\ \sigma_1\sigma_2\sigma_3\sigma_4}} U^{\text{full}}_{lm'ml'}(\mathbf{R}_1,\mathbf{R}_2,\mathbf{R}_3,\mathbf{R}_4)\,\hat{c}^\dagger_{\mathbf{R}_3 m'\sigma_3}\hat{c}^\dagger_{\mathbf{R}_1 l\sigma_1}\hat{c}_{\mathbf{R}_2 m\sigma_2}\hat{c}_{\mathbf{R}_4 l'\sigma_4} \tag{1.16}$$

with

$$t_{lm}(\mathbf{R}_1,\mathbf{R}_2) = -\int d^3r w^*_{l\mathbf{R}_1}(\mathbf{r})\left[-\frac{\hbar^2}{2m}\Delta + V(\mathbf{r})\right] w_{m\mathbf{R}_2}(\mathbf{r}) \tag{1.17a}$$

$$U^{\text{full}}_{lm'ml'}(\mathbf{R}_1,\mathbf{R}_2,\mathbf{R}_3,\mathbf{R}_4) = \int d^3r d^3r' w^*_{m'\mathbf{R}_3}(\mathbf{r}) w^*_{l\mathbf{R}_1}(\mathbf{r}')\frac{e^2}{|\mathbf{r}-\mathbf{r}'|} w_{m\mathbf{R}_2}(\mathbf{r}') w_{l'\mathbf{R}_4}(\mathbf{r}). \tag{1.17b}$$

The matrix t_{lm} (describing both hopping processes ($l \neq m$) and energy levels ($l = m$)) can now be simply obtained by using the previous Wannier transformation matrices and applying them onto the correlated energy states. Doing the same procedure directly for the Coulomb interaction $U^{\text{full}}_{lm'ml'}$ however leads to too large interaction values. Because we only concentrate on a subspace of the, for our purposes, interesting bands we implicitly neglect screening effects from other bands. Therefore other techniques are first required to get a properly screened interaction, e.g. the constrained random phase approximation (cRPA) [43, 44, 45] or the constrained local density approximation (cLDA) [46]. Instead of the bare interaction $\frac{e^2}{|\mathbf{r}-\mathbf{r}'|}$ we obtain a partially screened interaction

$$U^{\text{full}}_{lm'ml'}(\mathbf{R},\mathbf{R},\mathbf{0},\mathbf{0},\omega) = \int d^3r d^3r' w^*_{m'\mathbf{0}}(\mathbf{r}) w^*_{l\mathbf{R}}(\mathbf{r}') W_r(\mathbf{r},\mathbf{r}',\omega) w_{m\mathbf{R}}(\mathbf{r}') w_{l'\mathbf{0}}(\mathbf{r}), \tag{1.18}$$

where we additionally assumed the interaction to be dependent only on one spatial coordinate $\mathbf{R}$. On the other hand this new interaction now depends on the frequency ω.[5]

1.4 Dynamical mean-field theory

For Hamiltonians such as the one in Eq. (1.10) exact solutions only exist for special cases, e.g. for one dimension [47], for infinite dimensions [48], for the atomic limit ($t \to 0$) or for the non-interacting case ($U \to 0$). In order to obtain a solution for our general problem, further approximations are therefore required. This is where dynamical mean-field theory (DMFT) comes into play (the full details of the necessary Green's function description will be discussed in chapter 2). DMFT uses the notion that a single site in a solid can be locally interpreted as an effective atom that can exchange particles with a bath/reservoir mimicking all the other

[5] Screening processes are inherently frequency-dependent. In many post-DFT methods, however, this frequency dependence is neglected and only the value at $\omega = 0$ is used.

electrons via a hybridization function Δ. In this context DMFT maps the Hubbard model onto a more accessible auxiliary problem, namely the Anderson impurity model (AIM). For a *finite* number of bath sites N and a single orbital, the AIM Hamiltonian reads, e.g.

$$\hat{H}_{\mathrm{AIM}} = \sum_{\sigma} \varepsilon_0 d_\sigma^\dagger d_\sigma + U d_\uparrow^\dagger d_\uparrow d_\downarrow^\dagger d_\downarrow + \sum_{\substack{\sigma \\ k=1}}^{N} V_k c_{k\sigma}^\dagger d_\sigma + V_k^* d_\sigma^\dagger c_{k\sigma} + \sum_{\substack{\sigma \\ k=1}}^{N} \varepsilon_k c_{k\sigma}^\dagger c_{k\sigma}. \tag{1.19}$$

Here the local site is described by operators d_σ which interact via the hybridization term V_k with the bath described by operators $c_{\mathbf{k}\sigma}$. The hybridization function Δ and the hybridization term V_k are connected via

$$\Delta(\nu) = \sum_k \frac{|V_k|^2}{\nu + \mu - \varepsilon_k + i0^+}. \tag{1.20}$$

In the case of such a discretized bath this problem can then be solved with different methods including exact diagonalization (ED). A more general method are continuous time quantum monte carlo (CTQMC) simulations [7, 49, 50]. The prescription is identical for all methods: The *local* projection of the lattice Green's function G is identified with the impurity Green's function. The DMFT approximation is performed when computing the lattice Green's function using the impurity self-energy, i.e.

$$\Sigma_{\mathrm{lattice}}(\mathbf{k}, \nu) \approx \Sigma_{\mathrm{impurity}}(\nu). \tag{1.21}$$

Hence, because of the local impurity problem, the self-energy is assumed to be momentum ($\mathbf{k}$) independent. This relation becomes exact in infinite dimensions and appears to be a very good approximation for typical three materials. Solving $G_{\mathrm{imp}} = G_{\mathrm{loc}}$ iteratively thus yields a self-consistent hybridization function $\Delta(\nu)$ (self-energy $\Sigma(\nu)$). The DMFT mapping and the role of the self-energy Σ is sketched in Fig. 1.1.

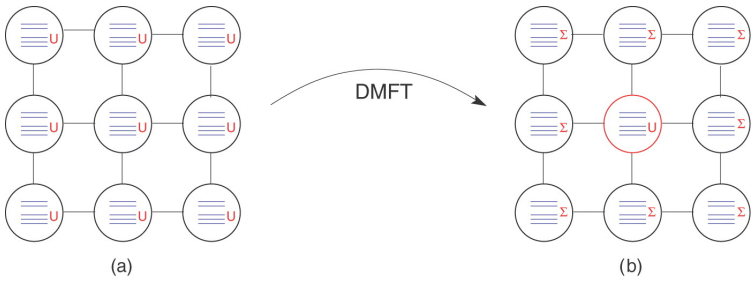

Figure 1.1: DMFT maps the lattice problem to a local impurity problem. The local interactions U (a) are 'replaced' by the self-energy Σ everywhere except the local site under consideration (b). Reproduced from [51].

2 Correlations beyond DFT

2.1 One-particle diagrams

In order to provide a more technical description of DMFT and all other post-DMFT methods we have to introduce the usual quantum-field theoretical description. This is done via so-called Feynman diagrams [52, 53, 54] where we start off by defining the n-particle Green's function in imaginary time τ

$$G_{i_1,i_2,\ldots,i_{2n-1},i_{2n}}(\tau_1,\tau_2,\ldots,\tau_{2n-1},\tau_{2n}) = (-1)^n \left\langle \mathcal{T}\left[c_{i_1}(\tau_1)c^\dagger_{i_2}(\tau_2)\cdots c_{i_{2n-1}}(\tau_{2n-1})c^\dagger_{i_{2n}}(\tau_{2n})\right]\right\rangle . \quad (2.1)$$

This represents a correlation function for adding and removing particles. The time ordering operator $\mathcal{T}$ orders the fermionic operators $\hat{c}^{(\dagger)}$ from left to right according to their time arguments τ_i so that after its application the outer left operator holds the largest and the outer right operator the smallest time argument. This reordering is accompanied with factors of (-1) for each swap of two operators. The notation used here and throughout the rest of this thesis is identical to the one used in `AbinitioDΓA` as well as all its associated publications. For a more detailed description please refer to Appendix B. Please note the difference in notation found in, e.g. [55] or [56]. There, in the particle-hole notation, a different frequency (momentum) transformation is employed while simultaneously using a Green's function arrow convention which is reversed compared to `AbinitioDΓA`. Contrary, the particle-particle frequency notation is identical.

The (proper) self-energy Σ is described via the Dyson equation and connects the interacting Green's function G with its non-interacting counter-part G_0.

$$\begin{aligned} G &= G_0 + G_0\Sigma G_0 + G_0\Sigma G_0\Sigma G_0 + \cdots \\ &= G_0 + G_0\Sigma G \end{aligned} \quad (2.2)$$

Here G is described by the usual infinite series of interaction processes of arbitrary complexity connecting non-interacting propagators. In order to include all possible diagrams and to avoid double-counting, the self-energy Σ must be defined as the summation over all one-particle *irreducible* diagrams. Reducibility in this context means that by cutting one connecting line the diagram falls apart into two valid diagrams. The basic building blocks for these diagrams are shown in Fig. 2.1 while the one-particle reducibility and the definition of the self-energy Σ is displayed in Fig. 2.2.

Figure 2.1: The bare propagator G_0 (left) and the local interaction U (right) represent the diagrammatic building blocks of perturbation theories for all models with local U. In our case they are mainly used for the description of the Anderson impurity model (and therefore DMFT). Reproduced from [55].

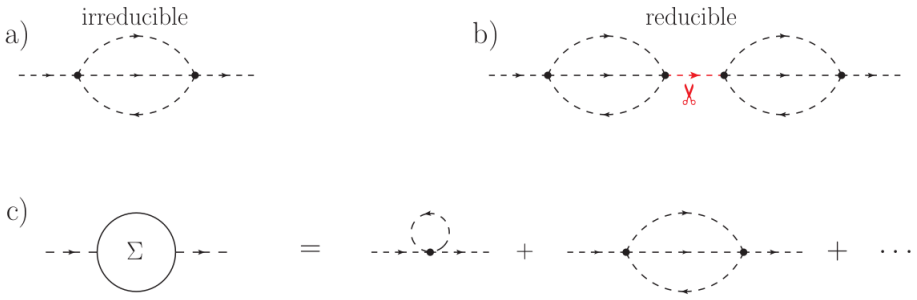

Figure 2.2: Examples for irreducible (a) and reducible (b) self-energy diagrams. Diagram (b) can be cut at the red dashed line and falls apart into two irreducible diagrams of type (a). The proper DMFT self-energy Σ is defined by the summation of all local irreducible diagrams (c). Reproduced from [55].

In the same vein we can diagrammatically represent the Dyson equation (2.2) which is displayed in Fig. 2.3.

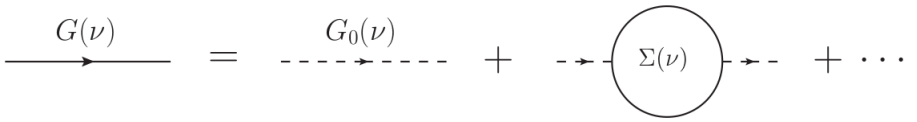

Figure 2.3: Diagrammatic representation of the Dyson equation (2.2). The interacting Green's functions G are represented as continuous lines instead of the dashed non-interacting Green's functions G_0. Reproduced from [55].

The analytical expressions for the Green's function can be obtained by exploiting the Heisenberg equation of motion (see Eq. (A.7)) and a Fourier transform to Matsubara frequencies [57].

In conjunction with the Dyson equation we get (see Appendix G for the multi-orbital lattice derivation and Ref. [55] for a non-interacting AIM derivation)

$$G_{\text{lattice}}\left(i\nu, \mathbf{k}\right) = \left[\left(i\nu + \mu\right)\delta_{mm'} - H^{\mathbf{k}}_{mm'} - \Sigma^{\mathbf{k}}_{mm'}\left(i\nu\right)\right]^{-1} \tag{2.3}$$

$$G_{\text{AIM}}\left(i\nu\right) = \left[\left(i\nu + \mu\right)\delta_{mm'} - \Delta_{mm'}\left(i\nu\right) - \Sigma_{mm'}\left(i\nu\right)\right]^{-1}, \tag{2.4}$$

where m, m' represent the involved orbitals, $i\nu$ the fermionic Matsubara frequencies, μ the chemical potential, $H^{\mathbf{k}}_{mm'}$ the Wannier Hamiltonian and $\Delta_{mm'}\left(i\nu\right)$ the hybridization function defined by

$$\Delta_{mm'}(i\nu) = \sum_{l} \frac{V^{*}_{ml} V_{lm'}}{i\nu + \mu - \varepsilon_{l}}. \tag{2.5}$$

2.2 Local correlations: dynamical mean-field theory

The mapping between the two different models – the original Hubbard model and the effective AIM – is now done via a self-consistent cycle. We start off with an arbitrary initial non-interacting local Green's function G_0 (e.g. the local projection of the non-interacting solution $\sum_{\mathbf{k}} G_0(i\nu, \mathbf{k})$). The next steps are then iterated until convergence is reached.

1. Compute the hybridization function:
   $\Delta(i\nu) = G_0^{-1}(i\nu) - i\nu - \mu$.

2. Compute the impurity Green's function $G_{\text{imp}}(i\nu)$ of the AIM, defined by $\Delta(i\nu)$, via an impurity solver.

3. Extract the self-energy of the impurity problem:
   $\Sigma_{\text{imp}}(i\nu) = G_0^{-1}(i\nu) - G_{\text{imp}}^{-1}(i\nu)$.

4. Identify the DMFT lattice self-energy with the impurity self-energy:
   $\Sigma_{\text{lattice}}(\mathbf{k}, i\nu) = \Sigma_{\text{imp}}(i\nu)$.

5. Compute the local projection of the lattice Green's function:
   $G_{\text{lattice,loc}}\left(i\nu\right) = \sum_{\mathbf{k}} \left[i\nu + \mu - H^{\mathbf{k}} - \Sigma_{\text{lattice}}\left(i\nu\right)\right]^{-1}$,
   and adjust μ to find the requested particle number.

6. Apply the DMFT self-consistency condition $G_{\text{imp}} = G_{\text{lattice,loc}}$ and use this relation to calculate a new non-interacting impurity Green's function:
   $G^{-1}_{0,\text{new}}(i\nu) = G^{-1}_{\text{imp,loc}}(i\nu) + \Sigma_{\text{imp}}(i\nu)$.

Due to the simplicity of the Dyson equation (2.2), the computationally most expensive part is calculating the impurity Green's function. In our case this is done by means of a CTQMC solver which works in imaginary times (`w2dynamics` [50]). Once converged, the impurity will thus 'feel' as if it were a site on our initial lattice. The resulting solution is mean-field like in spatial coordinates and dynamical in time and can therefore describe genuine correlation effects (see e.g. [58]).

Since all formulations described so far are on the imaginary time axis or in Matsubara frequencies we can extract only a limited amount of information, and need to do a continuation to real frequencies for physically analyzing the dynamics of our system. By following a Fermi-liquid low-energy expansion of the self-energy and taking into account that the real part of the self-energy is even while the imaginary part is odd we get in Matsubara frequencies

$$\Sigma(i\nu) \approx \Re\Sigma(i\nu \to 0^+) + \underbrace{i\,\Im\Sigma(i\nu \to 0^+)}_{-\gamma} + \underbrace{\left.\frac{\partial \Im\Sigma(i\nu)}{\partial i\nu}\right|_{i\nu\to 0^+}}_{1-Z^{-1}} i\nu + O(\nu^2). \tag{2.6}$$

From this we can extract the scattering rate γ and the quasi-particle weight $Z = \frac{m_e}{m_{eff}}$. From imaginary time, directly calculated by `w2dynmamics` [50], we can approximate the spectral function

$$A(\nu) \equiv -\frac{1}{\pi}\Im G(\nu) \tag{2.7}$$

around the Fermi level (see e.g. [59]):

$$G(\tau) = \int_{-\infty}^{\infty} d\omega A(\omega) \frac{e^{-\tau\omega}}{1+e^{-\beta\omega}} \tag{2.8a}$$

$$G\left(\frac{\beta}{2}\right) = \int_{-\infty}^{\infty} d\omega A(\omega) \frac{1}{2\cosh(\beta\omega/2)} \tag{2.8b}$$

$$A(\omega=0) \approx G\left(\frac{\beta}{2}\right)\cdot\frac{\beta}{\pi} \tag{2.8c}$$

This is a good approximation for $A(\omega = 0)$ for large enough inverse temperatures β.[6] If these quantities (Eqs. (2.6) and (2.8c)) are not sufficient we ultimately have to transform the full spectral function to the real frequency space. This is done via a technique called analytical continuation where one can employ different techniques such as the maximum entropy algorithm (MaxEnt) [60] or routines relying on Padé approximants [61].

[6] The limit $\beta \to \infty$ leads to the exact relation

$$\lim_{\beta\to\infty} \int_{-\infty}^{\infty} d\omega A(\omega) \frac{1}{2\cosh(\beta\omega/2)} \frac{\beta}{\pi} = \int_{-\infty}^{\infty} d\omega A(\omega)\cdot\delta(\omega) = A(0). \tag{2.9}$$

2.3 Two-particle diagrams

DMFT works well for a wide range of materials but due to the mapping onto a local impurity it is inherently unable to capture non-local correlations. These non-local effects are especially prominent in low dimensional systems, where the DMFT approximation begins to crumble, or near phase transitions where correlation lengths even diverge. First attempts to treat these problems were done by extending DMFT to a cluster formulation (e.g. cellular DMFT [9] or dynamical cluster approximation [8, 62]). While short-ranged correlation effects can be described by these theories, long-ranged effects are still only considered on a mean-field level. For that reason a wide range of theories were developed over the last years which try to include non-local correlations on all length scales. The one we will focus on over the course of this thesis is the so-called dynamical vertex approximation DΓA [10]. The main idea behind DΓA is to push the assumption of locality from the one-particle level to the two-particle level. However before diving straight into its details we have to start off by classifying the two-particle diagrams involved. While all possible two-particle diagrams are irreducible on the one-particle level[7], on the two-particle level they can be categorized into two groups

– Two-particle irreducible.

– Two-particle reducible in one specific channel r.

Similarly to the one-particle reducibility, two-particle reducibility means that by cutting a diagram along a given channel (i.e. cutting 2 lines) we get two new valid two-particle diagrams. This cutting procedure can be performed in three different ways, resulting in three channels $r \in ph, \overline{ph}, pp$ (particle-hole (longitudinal), particle-hole transversal, particle-particle). We can then express this classification in form of the equation

$$\underbrace{F}_{\text{1PI}} = \underbrace{\Lambda}_{\text{2PI}} + \underbrace{\Phi_{\text{pp}} + \Phi_{\text{ph}} + \Phi_{\overline{\text{ph}}}}_{\text{2PR}} . \tag{2.10}$$

The one-particle irreducible full vertex F (describing all possible two-particle interactions) thus consists of all two-particle irreducible diagrams, coined Λ, and all other diagrams which can be reducible –at most– in one out of the three previously mentioned channels. This classification along with exemplary diagrams is illustrated in Fig. 2.4.

Another way to express this equation is with the help of the two-particle irreducibility in a given channel r. In this vein a diagram can exclusively be either reducible (Φ_r) or irreducible (Γ_r) in

[7] A one-particle reducible two-particle diagram would violate the conservation of particles and thus cannot exist.

one specific channel. As a consequence all reducible diagrams can then be constructed via a so-called ladder, i.e. we build an infinite series of irreducible diagrams connected with each other by their appropriate propagators (akin to how the interacting Green's function was constructed). These so-called Bethe-Salpeter equations (BSE) read

$$\begin{aligned} F &= \Gamma_r + \Phi_r \\ &= \Gamma_r + \int \Gamma_r (GG)_r \Gamma_r + \int \Gamma_r (GG)_r \Gamma_r (GG)_r \Gamma_r + \cdots \\ &= \Gamma_r + \int \Gamma_r (GG)_r F. \end{aligned} \tag{2.11}$$

With this knowledge we can combine all four equations (three BSEs and the classification) into the so-called parquet equations

$$\begin{aligned} \Phi_{\text{ph}} &= \int \Gamma_{\text{ph}} (GG)_{\text{ph}} F = \int \left(F - \Phi_{\text{ph}}\right) (GG)_{\text{ph}} F \\ &= \int \left(\Lambda + \Phi_{\overline{\text{ph}}} + \Phi_{\text{pp}}\right) (GG)_{\text{ph}} F \end{aligned} \tag{2.12a}$$

$$\begin{aligned} \Phi_{\overline{\text{ph}}} &= \int \Gamma_{\overline{\text{ph}}} (GG)_{\overline{\text{ph}}} F = \int \left(F - \Phi_{\overline{\text{ph}}}\right) (GG)_{\overline{\text{ph}}} F \\ &= \int \left(\Lambda + \Phi_{\text{ph}} + \Phi_{\text{pp}}\right) (GG)_{\text{ph}} F \end{aligned} \tag{2.12b}$$

$$\begin{aligned} \Phi_{\text{pp}} &= \int \Gamma_{\text{pp}} (GG)_{\text{pp}} F = \int \left(F - \Phi_{\text{pp}}\right) (GG)_{\text{pp}} F \\ &= \int \left(\Lambda + \Phi_{\text{ph}} + \Phi_{\overline{\text{ph}}}\right) (GG)_{\text{pp}} F \end{aligned} \tag{2.12c}$$

$$F = \Lambda + \Phi_{\text{pp}} + \Phi_{\text{ph}} + \Phi_{\overline{\text{ph}}}. \tag{2.12d}$$

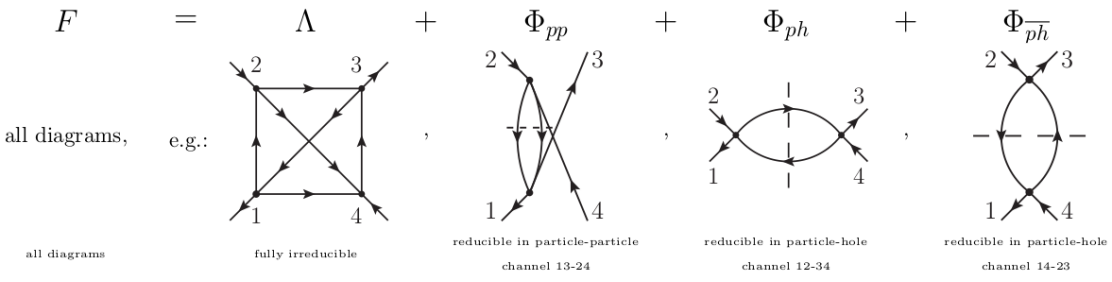

Figure 2.4: Classification of the full vertex in its separate parts according to Eq. (2.10). The indicated diagrams also show the two-particle reducibility in the three different channels. Reproduced from [63].

In order to actually obtain the numerical data for these kind of diagrams one once again makes use of an impurity solver. The local two-particle Green's function $G^{(2)}$ can be calculated (sampled in the case of a QMC solver) in a similar fashion as the one-particle Green's function G. E.g. in the particle-hole channel the local full vertex F is connected to the two-particle Green's function and the generalized susceptibility χ with the help of the bare susceptibility

$$\chi_0^{\nu\nu'\omega} = -\beta G^{\nu} G^{\nu'-\omega} \delta_{\nu,\nu'} \tag{2.13}$$

via

$$G^{(2)\,\nu\nu'\omega} = \beta G^{\nu} G^{\nu'} \delta_{\omega,0} + \underbrace{\chi_0^{\nu\nu'\omega} + \overbrace{\chi_0^{\nu\nu\omega} F^{\nu\nu'\omega} \chi_0^{\nu'\nu'\omega}}^{G^{\mathrm{con}\,\nu,\nu',\omega}}}_{\chi^{\nu\nu'\omega}}. \tag{2.14}$$

Diagrammatically this connection is illustrated in Fig. 2.5 where the so-called disconnected terms are represented by two Green's function which are not connected to each other (the full details are discussed in Appendices C and E).

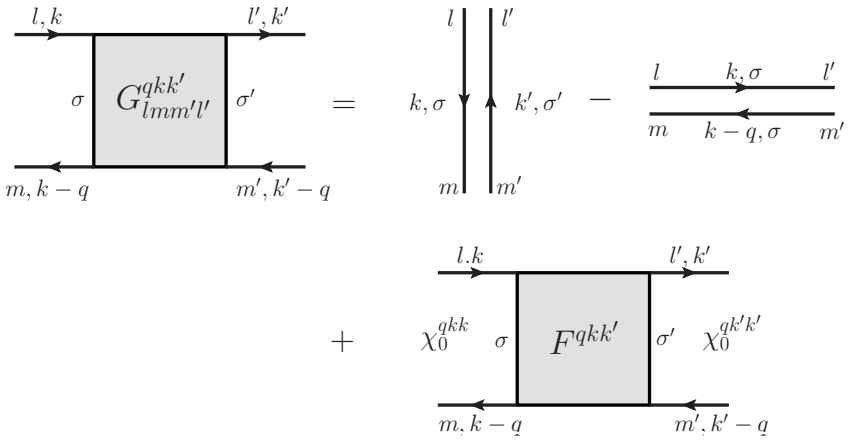

Figure 2.5: Diagrammatic representation of the separation of the two-particle Green's function $G^{qkk'}_{\sigma\sigma',lmm'l'}$ into its disconnected and connected terms. The connected Green's function contains the full vertex F while the disconnected parts are represented by 2 separate Green's functions.

Subsequently we have to subtract the disconnected terms from $G^{(2)}$ and then divide (amputate) the remaining four Green's function of the so-called connected part G^{con} in order to obtain the full vertex F.

2.4 Non-local correlations: parquet dynamical vertex approximation

Up until now the two-particle description was exact, i.e. we just rearranged diagrams into their respective groups and formed coupled expressions. In order to solve Equations (2.12) one needs to know the fully irreducible vertex Λ_0. Here, the dynamical vertex approximation (DΓA) comes into play. DΓA makes the assumption that the two-particle irreducible vertex Λ is local.[8] In that sense it represents the most natural extension of DMFT: The locality is pushed from the one-particle level (self-energy Σ) to the two-particle level

$$\Lambda^{qkk'} \rightarrow \Lambda^{\omega\nu\nu'} = \Lambda^{\mathrm{loc}}. \tag{2.15}$$

The DΓA flow usually starts with the previously described DMFT solution, i.e. we get a self-consistently solved local bath propagator G_0 / hybridization function Δ from DMFT. After that the following steps have to be carried out:

1. Compute the impurity Green's function $G_{\mathrm{imp}}(i\nu)$ and the impurity two-particle Green's function $G^{(2)}_{\mathrm{imp}}(i\nu, i\nu', i\omega)$ (or the generalized susceptibility χ) via an impurity solver.

2. Calculate the local full vertex F^{loc} by removing the disconnected terms and amputating the four legs.

3. Calculate the *local* irreducible vertices Γ_r via an inversion of the local BSE:
   $\Gamma^{\mathrm{loc}}_r = F^{\mathrm{loc}} \left[1 + (GG)^{\mathrm{loc}}_r F^{\mathrm{loc}}\right]^{-1}$

4. Calculate the local two-particle irreducible vertex Λ^{loc}:
   $\Lambda^{\mathrm{loc}} = F^{\mathrm{loc}} - \sum_r \left(F^{\mathrm{loc}} - \Gamma^{\mathrm{loc}}_r\right)$

5. Calculate the *non-local* full vertex F via the non-local BSE[9]:
   $F = [1 - \Gamma_r (GG)_r]^{-1} \Gamma_r$

6. Recalculate the two-particle irreducible vertices Γ_r via the parquet equations:
   $F, G, \Lambda^{\mathrm{loc}} \rightarrow \Phi_r \rightarrow \Gamma_r$

7. Iterate step 5 and 6 until convergence.

8. After convergence is reached, calculate the non-local self-energy $\Sigma_{D\Gamma A}(\mathbf{k}, i\nu)$ via the equation of motion (see Appendix G for a typical derivation).

[8] In the parquet approximation one, e.g., uses the bare interaction U as Λ.

[9] In the first iteration the non-locality from the full vertex F is created only from the non-local propagators. All following iterations will use non-local irreducible vertices Γ_r.

9. Calculate a new Green's function via the Dyson equation:
   $G = \left[G^{-1}_{0,\text{lattice}} - \Sigma_{D\Gamma A}\right]^{-1}$

10. Return to step 5 and iterate steps 5 to 9 until convergence.

11. Calculate a new non-interacting impurity Green's function G_0^{new}. This can, e.g., be determined by solving the impurity problem until the unknown G_0^{new} reproduces the local projection of the DΓA Green's function from step 9:
    $G_0^{\text{new}} \overset{\text{imp}}{\longleftrightarrow} \sum_{\mathbf{k}} G(\mathbf{k}, i\nu)$

12. Iterate steps 1 to 11 until convergence.[10]

The apparent complexity of this procedure makes it clear that it is only really feasible for small problems (i.e. one band calculation). In addition to that it was shown that the full parquet algorithm only converges in the weak-coupling regime [64]. For these reasons a more simplified approach is needed if one wants to do calculations for larger problems (i.e. real materials).

2.5 Non-local correlations: ladder dynamical vertex approximation

LadderDΓA represents this simplified version of parquetDΓA. The main motivation behind this approach is that one usually does not need all possible channels to describe the physics involved. The obvious disadvantage is therefore the required knowledge of channels in which instabilities are expected. LadderDΓA can be formulated in two different ways: Either the locality of the *particle-particle* reducible diagrams

$$\begin{aligned} \Lambda^{qkk'} &\to \Lambda^{\omega\nu\nu'} = \Lambda^{\text{loc}} \\ \Phi_{\text{pp}}^{qkk'} &\to \Phi_{\text{pp}}^{\omega\nu\nu'} = \Phi_{\text{pp}}^{\text{loc}}, \end{aligned} \tag{2.16}$$

or the locality of the *particle-hole-transversal* reducible diagrams is assumed

$$\begin{aligned} \Lambda^{qkk'} &\to \Lambda^{\omega\nu\nu'} = \Lambda^{\text{loc}} \\ \Phi_{\overline{\text{ph}}}^{qkk'} &\to \Phi_{\overline{\text{ph}}}^{\omega\nu\nu'} = \Phi_{\overline{\text{ph}}}^{\text{loc}}. \end{aligned} \tag{2.17}$$

Since most problems we are interested in are reasonably well described by local particle-particle diagrams (superconducting fluctuations are expected to be small) we will stick from now on to the former description. In this case the ladderDΓA flow starts identical to parquetDΓA with a converged DMFT solution, i.e. a hybridization function Δ. The major difference is that we do not use the parquet equations to recalculate new irreducible vertices and handle the whole procedure without any self-consistent cycles. This reads

[10] The full iteration of the whole process is usually not done.

1. Compute the impurity Green's function $G_{\text{imp}}(i\nu)$ and the impurity two-particle Green's function $G^{(2)}_{\text{imp}}(i\nu, i\nu', i\omega)$ (or the generalized susceptibility χ) via an impurity solver.
2. Calculate the local full vertex F^{loc} by removing the disconnected terms and amputating the four legs.
3. Calculate the *local* irreducible vertices Γ_r in the specific channels under consideration via an inversion of the local BSE:
   $\Gamma^{\text{loc}}_r = F^{\text{loc}} \left[1 + (GG)^{\text{loc}}_r F^{\text{loc}}\right]^{-1}$
4. Calculate the *non-local* full vertex F via the non-local BSE:
   $F = \left[1 - \Gamma^{\text{loc}}_r (GG)_r\right]^{-1} \Gamma^{\text{loc}}_r$
5. Calculate the non-local self-energy $\Sigma_{D\Gamma A}(\mathbf{k}, i\nu)$ via the equation of motion.
6. Calculate a new Green's function via the Dyson equation:
   $G_{D\Gamma A} = \left[G^{-1}_{0,\text{lattice}} - \Sigma_{D\Gamma A}\right]^{-1}$

This easier approach allows us to do calculations for more complex materials (i.e. multi-orbital problems). For a complete derivation and implementation details of the ladderDΓA approach used in `AbinitioDΓA` [20, 24], which is used for all following calculations, please refer to Appendices D–I. There the ladder, as suggested in point 4, is not only built with the purely local irreducible vertex, but one is able to supplement this vertex with 'ab initio' non-local interactions (hence the name). This is done with the so-called interaction vertex $\mathbf{V}^{\mathbf{qkk'}}_{\substack{lmm'l' \\ \sigma\sigma'}}$ and reads

$$\Gamma^{qkk'}_{\substack{lmm'l' \\ \sigma\sigma'}} \equiv \Gamma^{\omega\nu\nu'}_{\substack{lmm'l' \\ \sigma\sigma'}} + \mathbf{V}^{\mathbf{qkk'}}_{\substack{lmm'l' \\ \sigma\sigma'}} \tag{2.18}$$

$$\mathbf{V}^{\mathbf{qkk'}}_{\substack{lmm'l' \\ \sigma\sigma'}} \equiv \beta^{-2} \left[V^{\mathbf{q}}_{lm'ml'} - \delta_{\sigma\sigma'} V^{\mathbf{k'-k}}_{m'lml'}\right]. \tag{2.19}$$

The connection between local and non-local irreducible vertex is illustrated in Fig. 2.6.

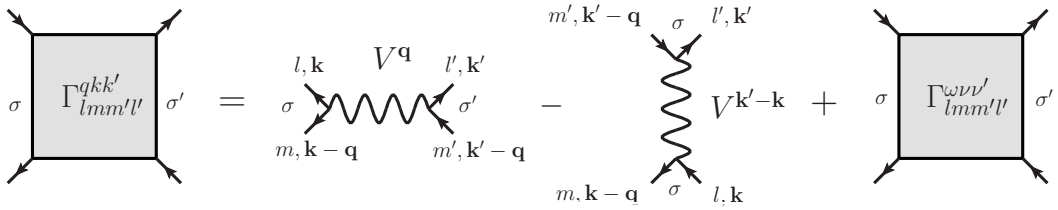

Figure 2.6: Diagrammatic representation of the supplementation of the local irreducible vertex $\Gamma^{\omega\nu\nu'}_{lm'ml'}$ with non-local interactions $V(\mathbf{q})$.

3 AbinitioDΓA for bulk $SrVO_3$

As a first step we will start by revisiting the results in the initial publications of the `AbinitioDΓA` project [20, 22, 23, 24]. Strontium vanadate $SrVO_3$, a common strongly correlated testbed material, crystallizes into a perovskite structure (see Fig. 2) with a lattice constant of $a = 3.8$Å. This crystallization is achieved by means of electron transfer, namely

$$\mathrm{Sr} + \mathrm{V}(3d^3 4s^2) + \mathrm{O}_3 \longrightarrow \mathrm{Sr}^{2+} + \mathrm{V}(3d^1) + \mathrm{O}_3^{2-}, \tag{3.1}$$

resulting in an ionic compound with (in an ideal picture) fully filled oxygen $2p$ bands, empty Strontium 5s bands and one d-electron in the vanadium t_{2g}-space.

According to photoemission spectra [65], as well as specific heat measurements [66], the t_{2g} orbitals display a mass enhancement of $Z^{-1} \approx 2$. This property can numerically be recovered by using the state-of-the-art DFT+DMFT approach. Starting from DFT in the GGA approximation (within `Wien2K` [36]) we realize the transformation to the Wannier basis for the energetically well separated $3d$ t_{2g} orbitals via `Wien2Wannier` [67]. The resulting band-structure is illustrated in Fig. 3.1.

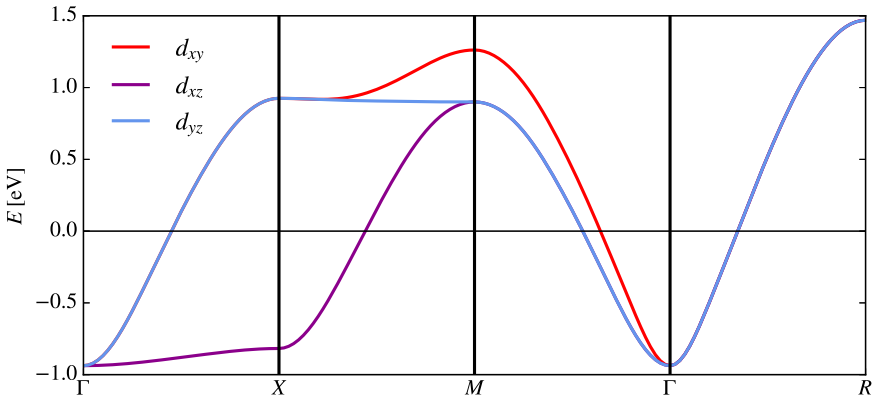

Figure 3.1: DFT band-structure of $SrVO_3$ calculated within GGA. The three vanadium t_{2g} bands around the Fermi level are well separated from the lower lying oxygen and higher lying vanadium $3d$ e_g bands (outside of the energy window displayed). The splitting of the t_{2g} and e_g bands is caused by the cubic crystal field originating from the characteristics of the involved orbitals (see e.g. [68]).

The interaction parameters U (intra-orbital), U' (inter-orbital) and J (Hund's exchange) can be calculated via cLDA and result in $U = 5$eV, $U' = 3.5$eV and $J = 0.75$eV which recover the

mass enhancement from experiments in DFT+DMFT [65], which also displays a kink [69]. We employ a SU(2) symmetric interaction parametrization, namely the Kanamori interaction [70]

$$\begin{aligned}\hat{U}^{\text{full}}_{\text{Kanamori}} = & \underbrace{U \sum_{m} n_{m\uparrow} n_{m\downarrow}}_{\text{intra-orbital density-density}} + \underbrace{\frac{1}{2} \sum_{\substack{m \neq m' \\ \sigma\sigma'}} \left[U' - \delta_{\sigma\sigma'} J\right] n_{m\sigma} n_{m'\sigma'}}_{\text{inter-orbital density-density}} \\ & + J \sum_{m \neq m'} \Big[\underbrace{\hat{c}^{\dagger}_{m\uparrow} \hat{c}^{\dagger}_{m'\downarrow} \hat{c}_{m\downarrow} \hat{c}_{m'\uparrow}}_{\text{spin-flip}} + \underbrace{\hat{c}^{\dagger}_{m\uparrow} \hat{c}^{\dagger}_{m\downarrow} \hat{c}_{m'\downarrow} \hat{c}_{m'\uparrow}}_{\text{pair-hopping}} \Big].\end{aligned} \tag{3.2}$$

It can be easily shown that these terms can be recovered by a generalized sum (employed in `AbinitioDΓA`) of the form

$$\hat{U}^{\text{full}} = \frac{1}{2} \sum_{\substack{ll'mm' \\ \sigma\sigma'}} U_{lm'ml'} \hat{c}^{\dagger}_{m'\sigma} \hat{c}^{\dagger}_{l\sigma'} \hat{c}_{m\sigma'} \hat{c}_{l'\sigma} \tag{3.3}$$

and the mapping

$$\begin{aligned} U_{mmmm} &= U \\ U_{mm'mm'} &= U' \\ U_{mm'm'm} &= J \\ U_{mmm'm'} &= J, \end{aligned} \tag{3.4}$$

where we can distinctly identify the last term as the pair-hopping contribution while the second to last term recovers both the spin-flip contribution (non-density-density part) as well as the Hund's exchange term in the inter-orbital density-density contribution (density-density part). Due to this inseparability the density-density interaction breaks SU(2) $\forall J > 0$. We stress that our ladderDΓA implementation requires a SU(2) symmetric interaction.[11]

Furthermore in cubic crystals, such as $SrVO_3$, one usually applies the relation $U = U' + 2J$ between the local intra- (U) and inter-orbital (U') parameter. This relation however only holds exactly for spherical symmetry [71] whereas in a cubic crystal structure the total symmetries are reduced to the cubic point symmetries. Nonetheless it was shown that using this spherical relation for screened interactions in the case of $3d$ orbitals provides a good approximation [72]. Consequently we will employ this relation in all the following calculations.

[11] A more generalized, i.e. momentum-dependent, interaction with an identical notation is used in the AbinitioDΓA derivation found in Appendix D.

3.1 Effects of temperature

The results [20] we want to expand on were done for an inverse temperature $\beta = 10\text{eV}^{-1}$. There the local two-particle vertex ($\chi^{\omega\nu\nu'}$) was sampled within `w2dynamics` [50] where ±60 frequencies for all three frequency dependencies were extracted. With the definition of the asymptotic region [73]

$$\nu_1\nu_2\nu_3\nu_4\frac{\beta^4}{\pi^4} > l^4\left|\delta_{\nu_1\nu_2} + \delta_{\nu_1\nu_4} - \delta_{\nu_1\nu_2}\delta_{\nu_1\nu_4}\right|^4 \tag{3.5}$$

and a replacement parameter of $l = 15$ one is subsequently able to show that the vertex region is smaller than the calculated size. This therefore allows the substitution of the QMC noise outside the vertex area with the much less noisy, purely asymptotic part (sampled separately). Additionally one can exploit this asymptotic vertex further and extend the original vertex to higher frequencies (for an introduction to multi-orbital vertex asymptotics please refer to [73]). This is helpful because our CTQMC solver works in imaginary times and must therefore apply a Fourier transform after sampling. This three-dimensional transform is rather memory-demanding and one is therefore limited in the number of frequencies one can calculate.

In order to minimize box size effects the vertex is thus extended from ±60 to ±200 through its asymptotics. The results for the purely local Kanamori interaction with the values given at the beginning of this chapter are then analyzed via the k-dependent version of Eq. (2.6)

$$\begin{aligned}\Sigma(\mathbf{k}, i\nu) &\approx \Re\Sigma(\mathbf{k}, i\nu \to 0^+) + i\Im\Sigma(\mathbf{k}, i\nu \to 0^+) + \left.\frac{\partial\Im\Sigma(\mathbf{k}, i\nu)}{\partial i\nu}\right|_{i\nu\to 0^+} i\nu + O(\nu^2) \\ &= \Re\Sigma(\mathbf{k}, i\nu \to 0^+) - i\gamma_{\mathbf{k}} + \left(1 - \frac{1}{Z_{\mathbf{k}}}\right) i\nu + O(\nu^2).\end{aligned} \tag{3.6}$$

The imaginary part of the DΓA self-energy (illustrated in Fig. 3.2) is only marginally affected where the quasi-particle weight $Z_{\mathbf{k}}$ varies less than 2% in the Brillouin zone. In the same vein the momentum-resolved scattering rate $\gamma_{\mathbf{k}}$ shows only slight adjustments towards larger values of the order of $5 - 15\%$ (one must be careful about the absolute values since they are strongly dependent on the fit). In contrast, the real part displays the largest non-local effects within DΓA (see lower panel of Fig. 3.2). The first fermionic frequency $i\nu_0$ varies more than 200meV and shows a similar pattern compared to the scattering rate. The direction in which this adjustment takes place can be best seen in Fig. 3.2, where the occupied states (lower lying energy levels) are shifted downwards while the unoccupied states (higher lying energy levels) are shifted upwards. This occupation-dependent splitting can be concluded from the band-structure in Fig. 3.1 and further confirms this point as, e.g., at the X-point the energies are split up more than 100meV.

The effects of high temperature ($T \approx 1000$K) can be seen as the Fermi surface can only be roughly surmised in the plots of Fig. 3.3.

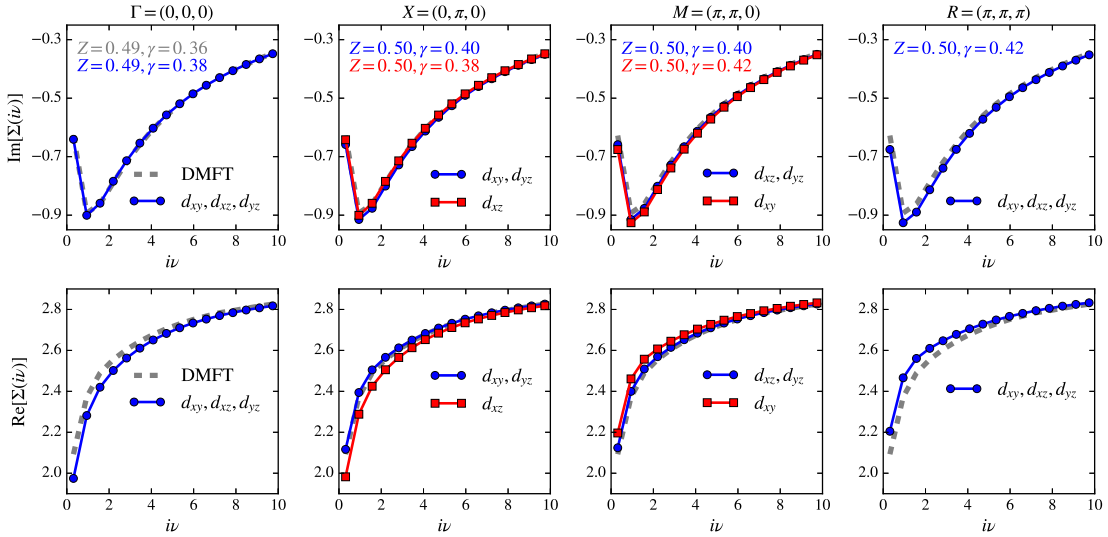

Figure 3.2: Real and imaginary parts of the DΓA self-energy for bulk $SrVO_3$ at the high symmetry points Γ, X, M and R calculated at $\beta = 10\text{eV}^{-1}$. The, locally, orbital symmetric DMFT self-energy is shown as dashed grey line while the DΓA self-energies are shown in color and split up depending on the **k**-dependent symmetry.

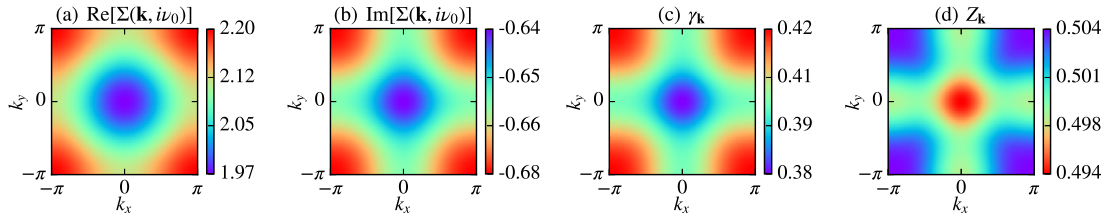

Figure 3.3: (a) Real and (b) imaginary parts of the DΓA self-energy at the first fermionic frequency $i\nu_0$. (c) Scattering rate $\gamma_{\mathbf{k}}$ and (d) quasi-particle weight $Z_{\mathbf{k}}$ according to Eq (3.6). The values were extracted in the $k_z = 0$ plane for only the xy-orbital, from which the symmetry originates, and interpolated from 20×20 to 100×100 k-points.[12]

[12] The polynomial was determined according to a least-squares fit (numpy.polynomial.polynomial.polyfit) while the interpolation was done with cubic splines (scipy.interpolate.interp2d). The fit was done via a third order polynomial at the first five frequencies.

To investigate the temperature dependence, similar calculations are performed at room temperature $\beta = 38\text{eV}^{-1}$ ($T \approx 300\text{K}$). We expected to find a more pronounced Fermi surface as well as larger non-local signatures. The reasoning being, that the DMFT approximation works best at high temperatures as here the thermal fluctuations dominate and suppress non-local correlations. Since the starting point changes, a new converged DMFT self-energy as well as a new vertex have to be calculated. Due to the lower temperature the CTQMC solver requires more computational time in order to obtain the same accuracy (the one- and two-particle Green's function have to be sampled in the interval $\tau \in [0, \beta)$) which fortunately remained feasible. The largest computational penalty is retained by the calculation of the new local two-particle vertex. Due to current implementation and memory limitations we are still restricted to ±60 frequencies for all three dependencies. This however is not a crucial factor since the non-asymptotic vertex domain, with the help of Eq. (3.5), can be shown to be already fully contained in it. We observe that, compared to the $\beta = 10\text{eV}^{-1}$ vertex, this domain scales with approximately β which suggests that only the absolute frequency values tend to matter in this respect. For all the following results the vertex is extended from ±60 to ±240 frequencies for all three dependencies. An exemplary replacement technique, following Eq. (3.5), is illustrated in Fig. 3.4. There, the areas with clearly visible QMC noise (corners of the left panels) are replaced by their corresponding asymptotic areas (middle panels). The resulting vertices (right panels) are then used for the calculations.

The imaginary parts of the DΓA self-energy (shown in Fig. 3.5) show again qualitatively little momentum dependence. The quasi-particle weight variation doubled to around 4% in the $k_z = 0$ plane compared to $\beta = 10\text{eV}^{-1}$ calculations. The scattering rate $\gamma_{\mathbf{k}}$ implies a rather large difference between the occupied and unoccupied states where the largest values can be found in the vicinity of the Fermi surface (see Figures 3.6 and 3.7). Also the real part shows again a similar behaviour as for the higher temperature, but now the Fermi surface is much more pronounced. One however has to be careful when comparing the absolute values at the lowest Matsubara frequency. The first frequency for $\beta = 38\text{eV}^{-1}$ is effectively four times closer to the zero point than for $\beta = 10\text{eV}^{-1}$ and we are always bound to introduce systematic errors when performing a polynomial fit. Nonetheless we see a trend towards non-locality with a well pronounced Fermi surface which in fact confirms our expectations.

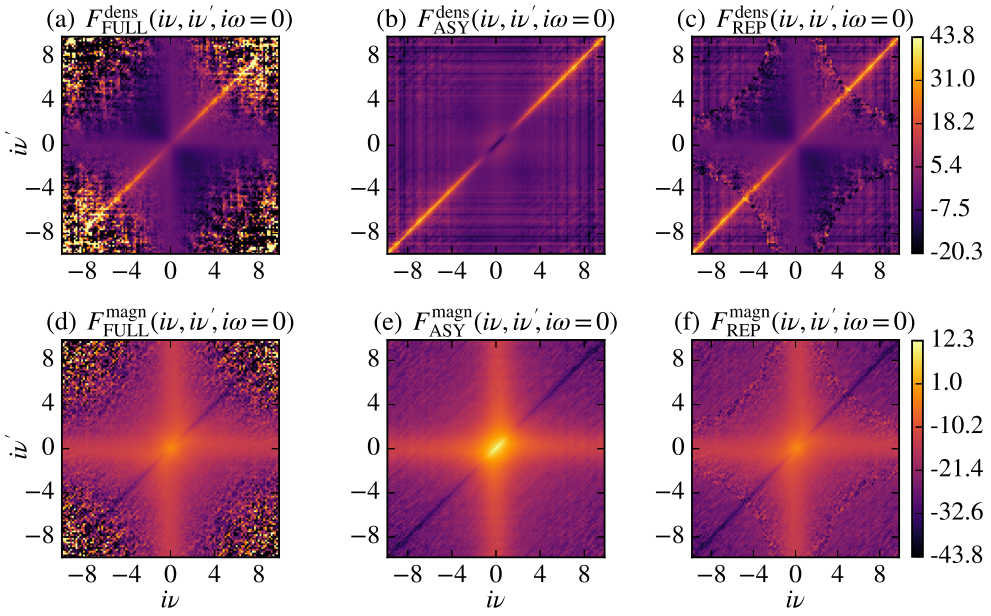

Figure 3.4: Two-particle vertex F_{1111} in the density channel at $i\omega = 0$ and $\beta = 38\mathrm{eV}^{-1}$ for the (a) full QMC data, (b) purely asymptotic data and (c) with the vertex used in the calculations (i.e. the inner non-asymptotic vertex domain from the full QMC data and the asymptotic domain from the asymptotic data). (d)-(f) same as (a) - (c) but for the magnetic channel. We show here all ±60 fermionic frequencies ν and ν' as sampled by CTQMC. The characteristic diagonal lines (from bottom left to top right) appear because here the interacting particles possess the same energy and thus they can interact without energy transfer.

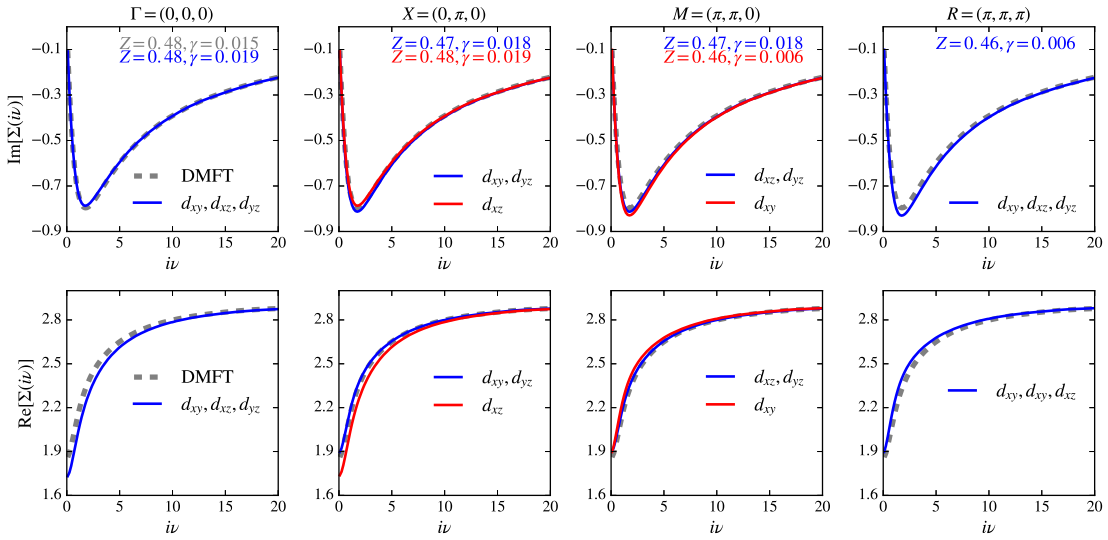

Figure 3.5: Real and imaginary parts of the DΓA self-energy for bulk $SrVO_3$ at the same high symmetry points as in Fig. 3.2 for $\beta = 38\text{eV}^{-1}$.

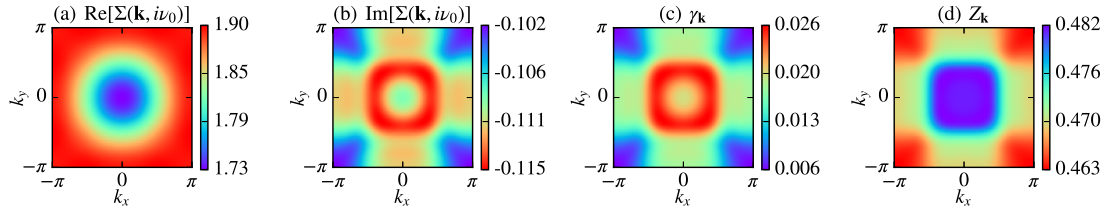

Figure 3.6: (a) Real and (b) imaginary parts of the $SrVO_3$ DΓA self-energy at the first fermionic frequency $i\nu_0$ as a function of momentum k_x and k_y. (c) Scattering rate $\gamma_{\mathbf{k}}$ and (d) quasi-particle weight $Z_{\mathbf{k}}$ according to Eq (3.6). The data here is shown in the $k_z = 0$ plane with the calculation performed for $\beta = 38\text{eV}^{-1}$.

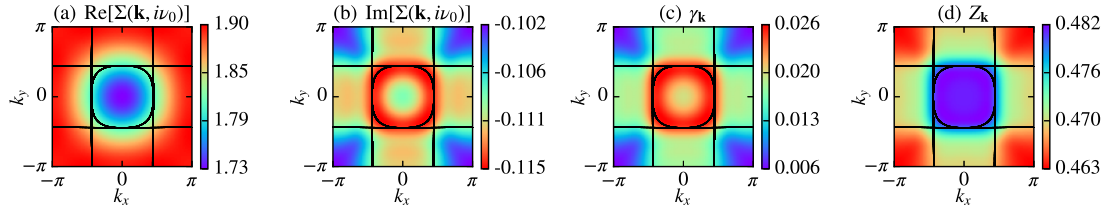

Figure 3.7: Same data as shown in Fig. 3.6 but with the LDA Fermi surface drawn on top of it (the black lines are drawn where the expression $H_{ll}(\mathbf{k}) - \mu_{\text{LDA}} = 0$ is fulfilled).

For completion, we also show here the (real part of the) momentum-dependent DMFT susceptibilities which one basically gets for free when solving the Schwinger-Dyson equation in `AbinitioDΓA` (see Appendix H). These, still orbital-dependent, density and magnetic susceptibilities (Figures 3.9 and 3.10) are displayed in form of a matrix. That is, e.g., the plot in the top right corner represents the entry 13 and thus is the data for χ_{1133}. In order to obtain experimentally measurable susceptibilities we have to sum over all orbital combinations

$$\chi_D \equiv \sum_{lm} \chi^{llmm}_{D} \tag{3.7a}$$

$$\chi_M \equiv 2 \sum_{lm} \chi^{llmm}_{M}. \tag{3.7b}$$

Here the factor 2 has to be introduced because of the missing gyromagnetic ratio g_e. By taking the off-diagonal elements into consideration (which are negative in the density susceptibilities) one can clearly see that the magnetic susceptibilities dominate the density susceptibilities in terms of size. The diagonal elements contribute the most while also having the largest momentum dependence. This is summarized in Fig. 3.8.

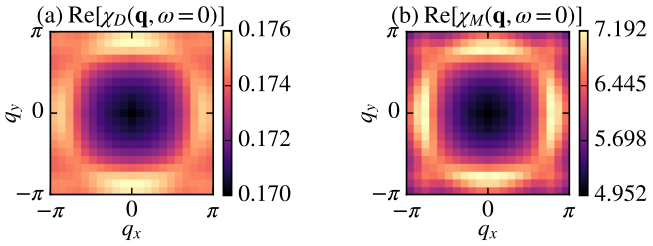

Figure 3.8: Physical density (a) and magnetic (b) susceptibility for bulk $SrVO_3$ at $\beta = 38\text{eV}^{-1}$ in the $q_z = 0$ plane. The data is obtained by applying Equations (3.7) onto the orbital-resolved susceptibilities from Figures 3.9 and 3.10. The magnetic susceptibility shows a strong momentum-dependence while also being orders of magnitude larger than its density counterpart.

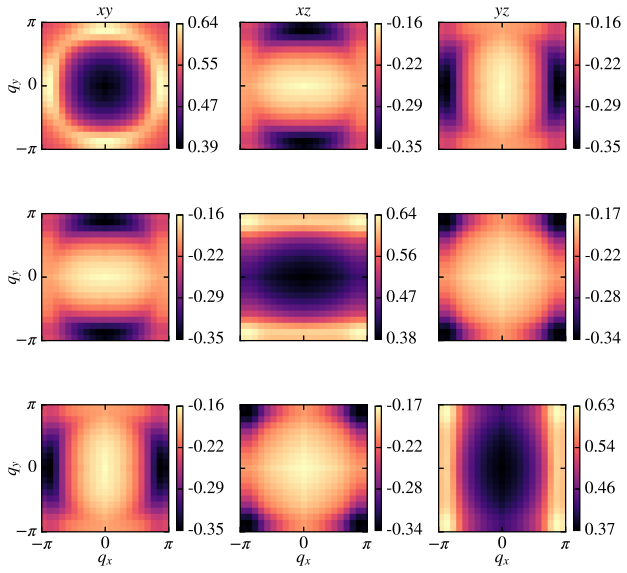

Figure 3.9: Real part of the orbital-resolved density susceptibilities $\chi_{D\ llmm}$ for bulk $SrVO_3$ at $\beta = 38\text{eV}^{-1}$ in the $q_z = 0$ plane at $\omega = 0$. The matrix position implicitly determines the involved orbitals, i.e. the diagram in the top right represents χ_{1133}. Due to time-reversal and inversion symmetry this 'matrix' must be symmetric, i.e. $\chi_{1133} \equiv \chi_{3311}$.

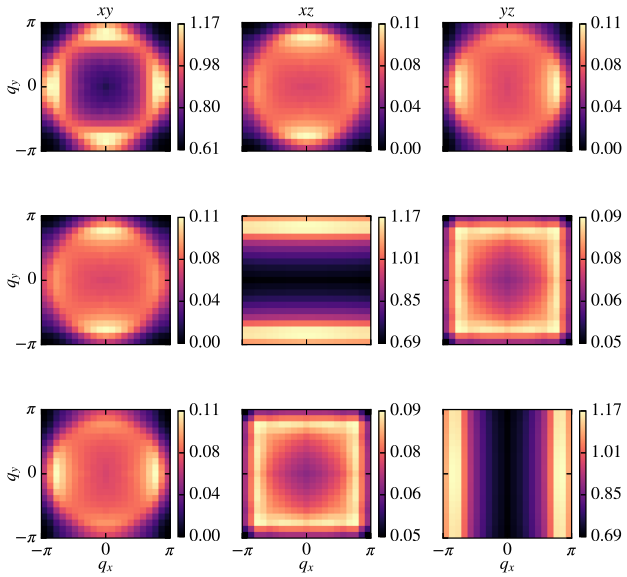

Figure 3.10: Same as Fig. 3.9 but now for the magnetic susceptibilities $\chi_{M\ llmm}$.

3.2 Effects of non-local interactions

Up to this point our description consisted of purely local interactions and therefore all non-local signatures we obtained originated from the (non-local) lattice propagators in the construction of the non-local Bethe-Salpeter equations. `AbinitioDΓA` however is derived in a way that allows the inclusion of non-local interactions on the level of the two-particle irreducible vertex Γ (see chapter 2.5 and Appendix F). Without these interactions the equation for the DΓA self-energy (Eq. (G.35)) simplifies and does not explicitly require the local boson-fermion vertex $\gamma_r^{\omega\nu}$ obtained via a frequency summation of $\chi_0 F$:[13]

$$\underset{r}{\gamma^{\omega\nu}_{lmm'l'}} \equiv \sum_{\substack{\nu' \\ n'h'}} \chi^{\omega\nu'\nu'}_{0,lmn'h'} \underset{r}{F^{\omega\nu'\nu}_{h'n'm'l'}} \tag{3.8}$$

By avoiding this object (it is still implicitly contained in the other two boson-fermion vertices $\gamma_r^{q\nu}$ and $\eta_r^{q\nu}$) we were also able to avoid most of the box size problems stemming from it.[14] Calculations with prominent non-local interactions make it essential to have data which ultimately has little to no box-size effects. The simplest and most obvious way to achieve this is by including as many frequencies as possible and hoping that the summation is converged. It turns out that this not optimal since a massive amount of frequencies is required for convergence and one would be furthermore restricted to high temperatures (only the absolute frequency size matters in the vertex domain thus requiring more frequencies at lower temperatures). A way out of this dilemma can be achieved by measuring this local boson-fermion vertex (coined $P^{(3)}$) [73] directly within CTQMC to replace $\chi_0 F$. The measurement is similar to the two-particle vertex measurement, yet one has to set two operators to an equal imaginary time. The required $\gamma_r^{\omega\nu}$ is then tightly connected to the result of this measurement (which is also required for the calculation of the kernel-2 function $K^{(2)\mathrm{ph}\ \nu\omega}$, necessary in the construction of the asymptotic vertex [73]) and one theoretically obtains an object with no box-size effects at all. Unfortunately this solution is not as perfect as it sounds since one ultimately exchanges box-size effects with QMC noise. Improvements in this regard could be further achieved by including asymptotic data of these $K^{(2)}$ objects and thus allowing us to go to higher frequencies. This is however currently not yet implemented and we have to be content with the data without further asymptotic, thus being restricted to a relatively small box $N = 60$.

[13] Due to this summation and the nature of the involved object it inherently displays the largest box size effects.

[14] The previous results for box sizes of ±60, ±120 and ±240 lie basically on top of each other. Only the first few frequencies are slightly affected by it leading to a slight deviation of $Z_{\mathbf{k}}$ and $\gamma_{\mathbf{k}}$.

In the following we show first calculations with this measured three-leg vertex $\gamma_r^{\omega\nu}$ at $\beta = 10\text{eV}^{-1}$ and the non-local interactions $V(\mathbf{q})$ shown in Fig. 3.11. The effects of the non-local interactions are clearly visible in the imaginary part of the DΓA self-energy in Fig. 3.12, where we see a trend towards less correlation (increasing Z; illustrated in Fig. 3.13). The quasi-particle weight now varies around 10% in the BZ with a maximum at the Γ point. The scattering rate is generally increased compared to the purely local results in chapter 3.1. A similar behaviour akin to the room temperature calculation can be observed: The Fermi surface of, in this case, just the *xy*-orbital looks to be well pronounced. Furthermore, we see a qualitatively different imaginary self-energy in all k-points where the values in Fig. 3.12, starting from $i\nu = 2\text{eV}$, are pushed upwards. Before commenting on the real part of the self-energy we have to mention that, compared to the previous calculation, it has to be evaluated in a slightly different manner. Due to the, now existing, non-local Hartree-Fock terms (see last line in Eq. (G.35)) we get massive shifts (up to 50eV mainly caused by the large value at $V(\mathbf{q} = \mathbf{0})$) purely in the real part. We circumvent this problem by adding these terms and subtracting the Brillouin zone mean

$$\Sigma(\mathbf{k}, i\nu) = \Sigma^{\text{no HF}}(\mathbf{k}, i\nu) + \Sigma^{\text{non-local HF}}(\mathbf{k}) - \sum_{\mathbf{k}\in\text{BZ}} \Sigma^{\text{non-local HF}}(\mathbf{k}). \tag{3.9}$$

By doing this we get real parts that are approximately centered where they were before adding these terms (ultimately absorbing them into the chemical potential to obtain a consistent occupation). The values at the first fermionic frequencies are consequently much wider spread with a maximum difference of more than 450meV. The trend is equivalent to the previous findings in that the occupied states are again pushed downwards and the unoccupied states are pushed upwards. In contrast to the imaginary part, the Fermi surface in Fig. 3.13 is much less pronounced leaving us with qualitatively the same pattern as in chapter 3.1.

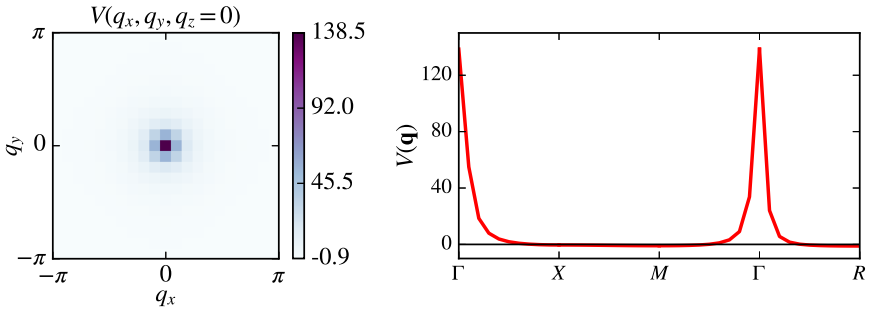

Figure 3.11: Exemplary purely non-local interaction $V(\mathbf{q})$ ($\sum_{\mathbf{q}} V(\mathbf{q}) = 0$) for the band-combination 1111 (only the *xy*-orbital is involved) in $SrVO_3$. The $V(\mathbf{q})$ data is obtained by performing a Fourier transform onto $U(\mathbf{r})$ data, calculated within cRPA.

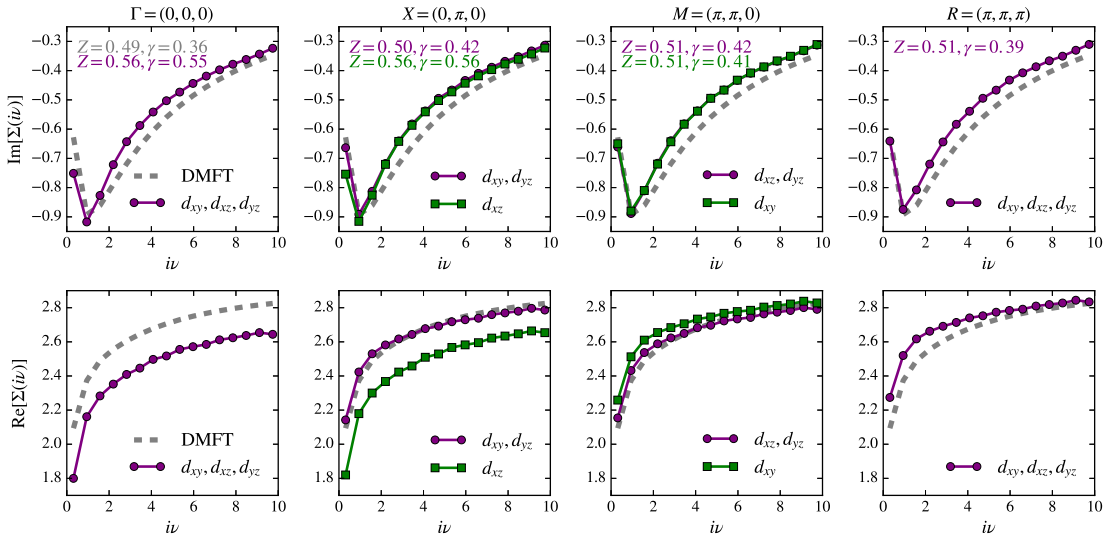

Figure 3.12: Real and imaginary parts of the DΓA self-energy of bulk $SrVO_3$ with included non-local interaction $V(\mathbf{q})$ at $\beta = 10\text{eV}^{-1}$.

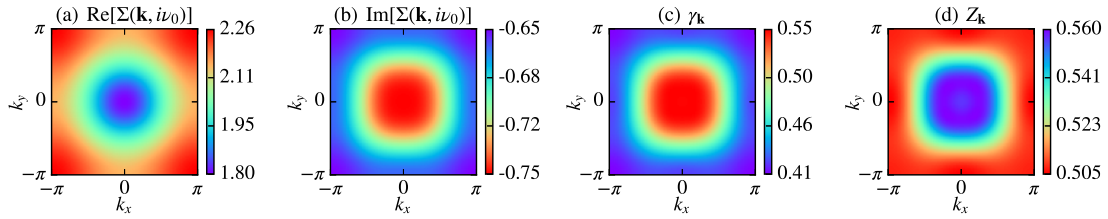

Figure 3.13: (a) Real and (b) imaginary parts of the DΓA self-energy at the first fermionic frequency $i\nu_0$. (c) Scattering rate $\gamma_{\mathbf{k}}$ and (d) quasi-particle weight $Z_{\mathbf{k}}$ according to Eq. (3.6). The calculation was performed at $\beta = 10\text{eV}^{-1}$ with the inclusion of non-local interactions.

As a final point in this chapter we will take a closer look at the box-size effects discussed at the beginning of this chapter. For comparison, calculations are shown for the box-sizes ±60, ±100, ±200 as well as the previously shown results using $\gamma^{\omega\nu}$. For clarification: In Figures 3.14 and 3.15 the panels in the bottom rows simply illustrate the data of the top rows at lower frequencies. The high-frequency box-size effects are best visible in the imaginary part of the self-energy in Fig. 3.14 where for all high-symmetry points the smaller boxes display unphysical behaviour.[15]

[15] The data for the $N = 200$ box extends much further which is why it looks almost unaffected.

In the top panels we can see that the external $\gamma^{\omega\ni}$ does not improve the internal summation in the high frequency range much. It is additionally being affected by the previously mentioned QMC noise suggesting that this phenomena originates from the bosonic box-size (see Eq. (G.35)). This ultimately makes larger boxes for this boson-fermion vertex a necessity. Unfortunately these box sizes are at this moment not yet available due to the missing implementation of the asymptotic behaviour of these vertices themselves. Nonetheless the calculation with external $\gamma^{\omega\nu}$ shows qualitatively better low-frequency behaviour (see bottom panels of Fig. 3.14) without any kinks as seen in the other calculations. Here we we see that, for all four high symmetry points, especially the value of the second frequency (around $i\nu = 0.94$) differs the most between the calculation with γ^{ω} and the rest. The most glaring discrepancy can be seen at the Γ-point ($\mathbf{q} = (0, 0, 0)$). This behaviour can be explained by the already mentioned large $V(\mathbf{q} = 0)$ value (see Fig. 3.11). Due to the relatively coarse k-mesh we might have implicitly given this point too much weight. This problem could be either solved by sampling the Brillouin zone in a more refined mesh or by keeping the old k-mesh and only replacing this one problematic value by an average of the Γ-vicinity. Due to the already quite fine mesh ($20 \times 20 \times 20$) the second variation is preferable.

The real part on the other hand looks to be much less affected by these summation effects. Here in the top panels of Fig. 3.15 the different calculations are only differing slightly. The QMC noise in the calculation with $\gamma^{\omega\nu}$ is similar to the imaginary part while being largest at the problematic Γ-point. In the low-frequency range increasing box-sizes show a trend which we have already seen before. That is, at the occupied states (X, M, R) the curves trend upwards while at the unoccupied state (Γ) the curves trend downwards (we are only referring to the xy-orbital here).

All in all, the low frequency convergence discrepancy (calculations with increasing box size do not converge towards the result with $\gamma^{\omega\nu}$) remains a problem which has to be investigated in greater detail in the future in order to achieve the best possible description with the current `AbinitioDΓA` implementation. We suggest that implementing proper $\gamma^{\omega\nu}$ asymptotics will bring the best results where we especially would target large bosonic frequency boxes and optimize k-meshes for the $V(\mathbf{q})$ calculation.

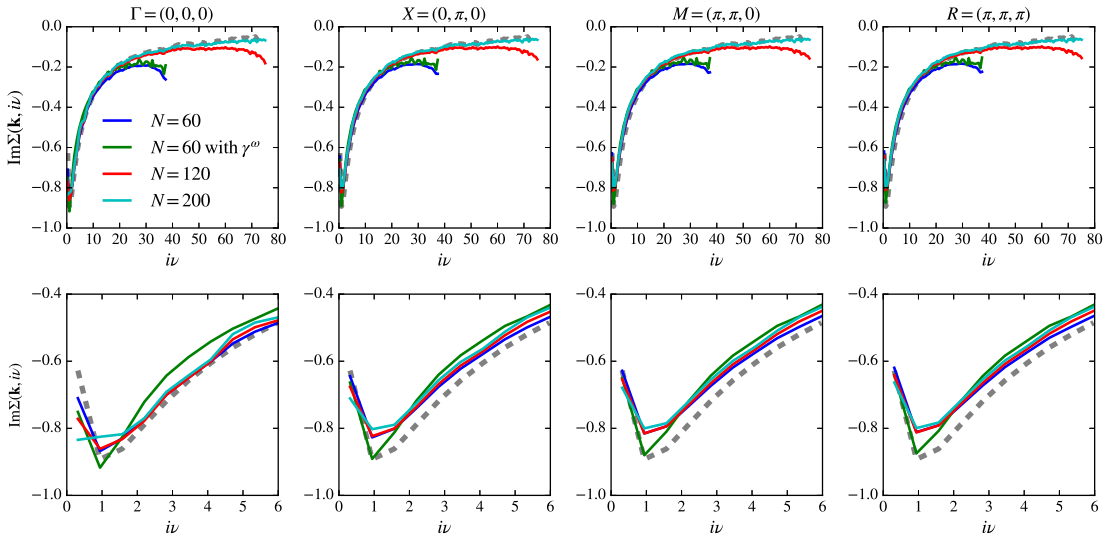

Figure 3.14: Influence of box size on the imaginary part of the DΓA self-energy at the high symmetry points. For improved visibility, we only show the results for the d_{xy} orbital. '$N = 60$ with γ^{ω}' illustrates the calculation with externally measured three-leg vertex while the other 3 calculations use a vertex which is summed up internally. This summation is consequently restricted to the stated box-size thus showing different degrees of box-size effects.

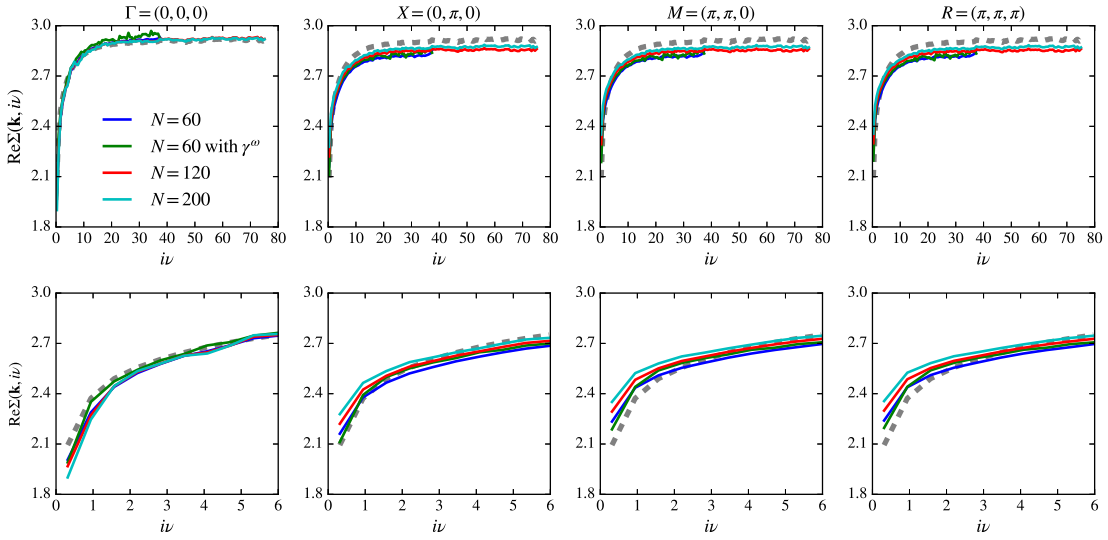

Figure 3.15: Same as Fig. 3.14 but now for the real part of the DΓA self-energy.

4 AbinitioDΓA for ultra-thin $SrVO_3$

As a starting point for the investigation of dimensionality effects in $SrVO_3$ we will resort to a previously published paper by Zhong et al. [74], which among others, is based on recent experimental findings which investigated the behaviour of ultra-thin $SrVO_3$ films [75]. In their experiments two-layered $SrVO_3$ has been found to be insulating which was further confirmed by Masaki et al. [76]. In [74] realistic DFT+DMFT calculations were performed which pinpointed the origin of this behaviour, namely the energy splitting caused by the broken local orbital symmetry. It was further concluded that by a manipulation of the interaction parameters, or by applying a potential, a Mott metal-to-insulator transition can be triggered which is unique for the bilayer case. While for three or more layers the system becomes more and more metallic and moves towards the bulk state, for one layer the system is purely insulating [74, 76].

4.1 DFT results

We reproduce their findings by doing similar DFT+DMFT calculations for a heterostructure consisting out of two $SrVO_3$ layers on top of a $SrTiO_3$ substrate. The insulating substrate is constructed out of five unit cells of $SrTiO_3$ together with a sufficiently large vacuum layer (around 8Å thick). The lattice equilibrium can be found by minimizing the DFT ground-state energy via a variation of the lattice constants involved in the Hamiltonian. This is expressed by the Hellmann-Feynman theorem and states

$$\frac{dE_\lambda}{d\lambda} = \left\langle \psi_\lambda \middle| \frac{d\hat{H}_\lambda}{d\lambda} \middle| \psi_\lambda \right\rangle, \tag{4.1}$$

where λ is an arbitrary parameter. This minimization determines a vertical lattice constant (perpendicular to the layer) between the two vanadium atoms of $a_{SrVO_3} = 3.83$Å and a gradually increase of the titanium spacing in the $SrTiO_3$ substrate starting from $a_{SrTiO_3} = 3.94$Å right below the vanadium layer up to $a_{SrTiO_3} = 4.00$Å above the vacuum. Compared to the $SrVO_3$ bulk lattice constant of $a = 3.8$Å we already see the mutual influence of the two respective crystals. The DFT calculation is analogously done with `Wien2K` [36] using linear augmented plane waves and the general gradient approximation (GGA). The maximally localized Wannier functions are prepared via `Wien2Wannier` [67] and the resulting Hamiltonian is created by projecting onto the three t_{2g} orbitals of both layers (see Fig. 4.1). With the `AbinitioDΓA` post-processing in mind a much finer k-mesh is chosen consisting out of $80 \times 80 \times 1$ k-points. The confinement in the z-direction by the vacuum at one end and the insulating $SrTiO_3$ at the other leads to a cut-off of neighbor hopping for both the xz- and yz-orbitals while having almost no

effect on the *xy*-orbital. This in turn means that the two affected *xz*- and *yz*-orbitals become more 1-dimensional leading to a crystal-field splitting Δ between the *xy*- and both the *xz*/*yz*-orbitals. In the top $SrVO_3$ layer this results in $\Delta = 0.22$eV while in the bottom $SrVO_3$ layer it is reduced to around $\Delta = 0.07$eV where in both layers the *xz*/*yz* orbitals are energetically pushed higher. This can be seen, e.g., at the Γ-point when comparing both the bulk and two-layer band-structure in Figs. 3.1 and 4.1. To summarize the DFT result we illustrate the resulting k-resolved Hamiltonian in form of a band-structure striding through all high symmetry points.[16]

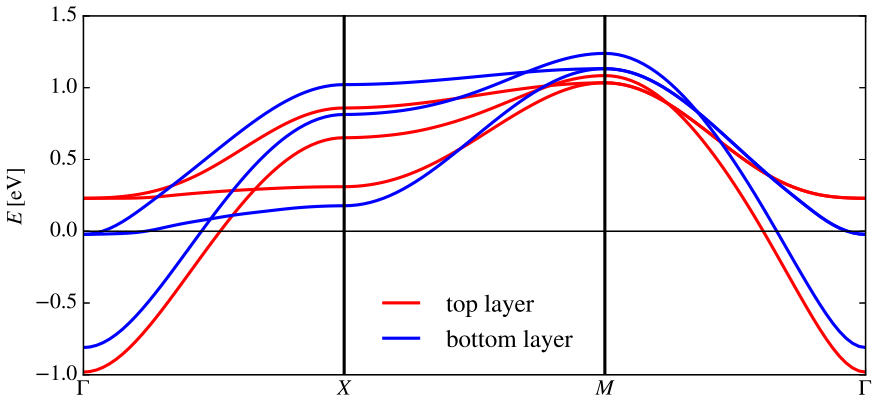

Figure 4.1: DFT band-structure of the $SrVO_3$ bilayer Hamiltonian calculated within GGA. The lowest bands at the Γ-point represent the *xy* orbitals while the highest bands at the *X*-point represent the *yz* orbitals.

4.2 DMFT results

Continuing from the DFT result we perform DMFT calculations with `w2dynamics` in the continuous-time hybridization expansion (CT-HYB) [50]. Supplementing the Hamiltonian with a Kanamori interaction and, identical to bulk $SrVO_3$, using a Hund's exchange of $J = 0.75$eV we perform all following calculations at room temperature ($\beta = 38\text{eV}^{-1}$). Instead of working with a fixed intra- and inter-band interaction parameter we vary them while still fulfilling the quasi-symmetry condition $U = U' + 2J$. In this context we start our initial calculations with $U' = 2.8$eV ($U' = 3.8$eV). Subsequent calculations are done with the previously converged endpoint used as starting point while simultaneously increasing (decreasing) the interaction by $\Delta U' = 0.1$eV. This is repeated 10 times so that we arrive at each others initial starting points $U' = 3.8$eV ($U' = 2.8$eV). All in all we have to properly converge 22 DMFT calculations from

[16] The two-dimensional cubic crystal structure shares the same symmetry points with the three-dimensional cubic crystal with the exception of $R = (\pi, \pi, \pi)$.

which we then can extract the required information.

Figure 4.2 illustrates the Mott metal-to-insulator transition where we extract the spectral function at the Fermi level via $G(\tau = \frac{\beta}{2})$, the orbital occupation $n_{i\uparrow} = \left\langle \hat{c}^{\dagger}_{i\uparrow} \hat{c}_{i\uparrow} \right\rangle$[17] as well as the (not normalized) double occupation $D_i = \left\langle \hat{c}^{\dagger}_{i\uparrow} \hat{c}_{i\uparrow} \hat{c}^{\dagger}_{i\downarrow} \hat{c}_{i\downarrow} \right\rangle$. In Fig. 4.3 we additionally show the impurity occupations defined by

$$n_{\text{imp}} = \sum_{i,\sigma} n_{i\sigma}. \tag{4.2}$$

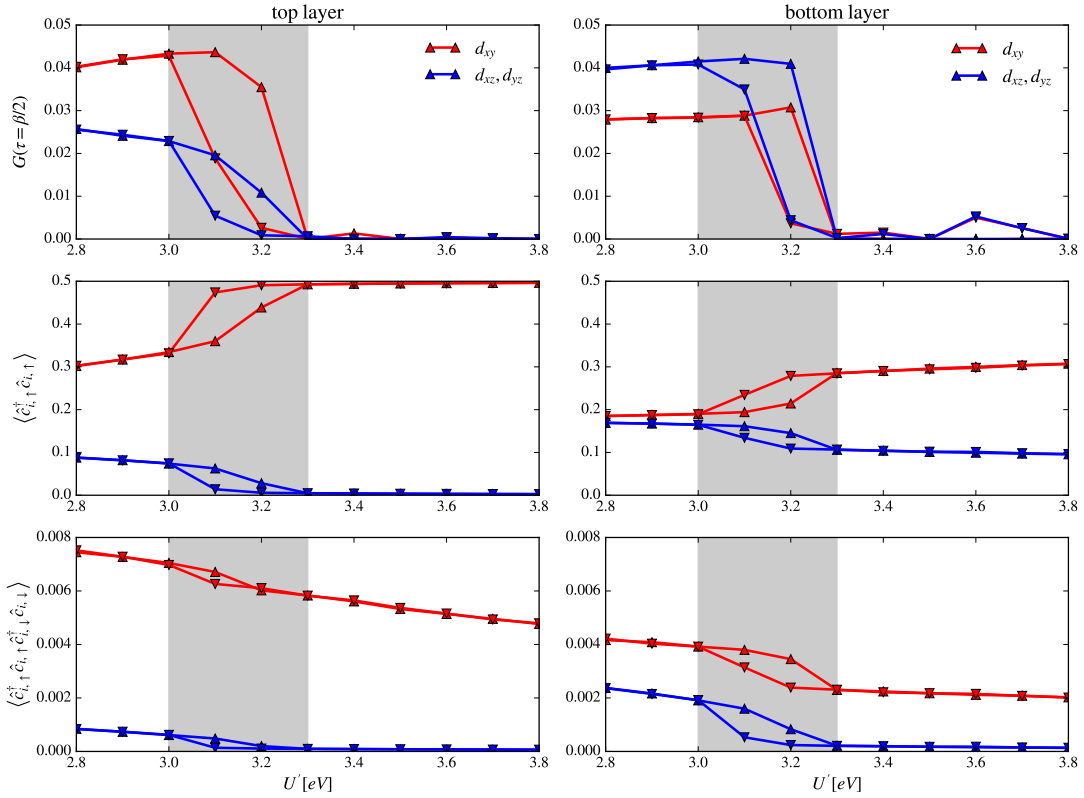

Figure 4.2: Spectral function at the Fermi edge[18](top panels), orbital occupation (middle panels) and double occupation (bottom panels) for the top layer (left panels) and the bottom layer (right panels) of $(SrVO_3)_2/(SrTiO_3)_4$ as obtained by DFT+DMFT. The graph with increasing (decreasing) U' is marked with triangles pointing upwards (downwards). The first order MIT transition (marked with a gray background) is accompanied by a depopulation of the xz/yz-orbitals in the top $SrVO_3$ layer (middle left panel) which creates a half-filled xy-orbital.

[17] The calculations are done in the paramagnetic phase, thus the orbital occupations here do not depend on the involved spin: $n_{i\uparrow} \equiv n_{i\downarrow}$.

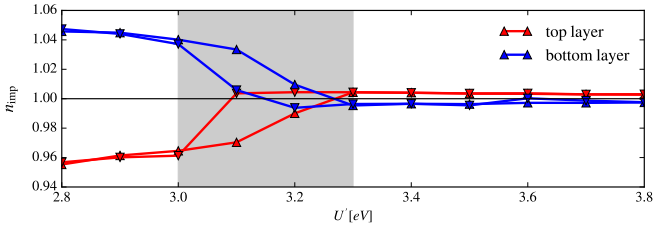

Figure 4.3: Impurity occupation of the top and bottom impurity with increasing and decreasing U'. The marker convention is identical to Fig. 4.2. In the metallic domain the impurity in the bottom layer holds 10% more population, whereas both layers host one electron per V-atom in the insulating state.

The top panels of Fig. 4.2 display the transition between metal (finite $\overline{A(0)} \approx G(\tau = \beta/2)$) and insulator ($\overline{A(0)} = G(\tau = \beta/2) = 0$). This transition is taking place simultaneously in the top and the bottom layer where both remain insulating at inter-orbital interaction values of $U' \geq 3.3$eV.[19] Due to the DMFT feedback this is however not surprising since they both mutually influence each other, which, as we see, results in common conducting and insulating regions. The orbital occupations in the middle panels further confirm the transition where a depopulation of the energetically higher lying xz/yz orbitals in the top layer takes place which is accompanied by a decrease of double occupations (bottom panels). This transfer of population to the xy-orbital creates an effectively half-filled single orbital, In this case the interaction U is already strong enough to create a Mott insulator. Essentially the same, albeit less pronounced, features can be seen in the bottom layer as well.[20] Here just a slight shift in population occurs where in the conducting domain all orbitals are approximately equally filled while in the insulating domain the xy-orbital contains 75% of the impurity population.

One additional feature, which has not been discussed in the original publication [74], can be observed in Fig. 4.3. In the insulating domain the population is (almost) equally distributed between the two impurities while in the conducting domain a major imbalance occurs. Here the bottom layer impurity holds 10% more population which is transferred to the top layer impurity when the MIT is triggered.

[18] To be exact we would need to multiply these values by $\frac{\beta}{\pi} \approx 12$ to get the actual spectral function $\overline{A(\omega = 0)}$.

[19] The hysteresis previously found in [21] is shifted by 0.2eV to the left compared to our results. This is possibly due to a mistake made in [21] where a Hund's coupling of $J = 0.65$eV instead of $J = 0.75$eV was used. In conjunction with the employed relation $U = U' + 2J$, this would exactly explain this discrepancy.

[20] The features seen in the top panels of Fig. 4.2 at values of $U' \geq 3.4$eV do not have a physical origin and are just artifacts of DMFT problems in the insulating phase. They surprisingly only occurred when transitioning from higher to lower values of U' and remain even with worm-sampling [77].

As final points, in Fig. 4.4 we show two characteristic Green's functions, as sampled by CTQMC as well as the DMFT band-structure calculated via analytical continuations in Fig. 4.5. The former illustrates the metal-to-insulator transition from a more technical point of view. In the conducting region all orbitals have finite, positive values at all imaginary times τ. By increasing the interaction these curves are pushed towards the horizontal axis, creating an insulating system once the values around $\tau = \beta/2$ are identical to 0.

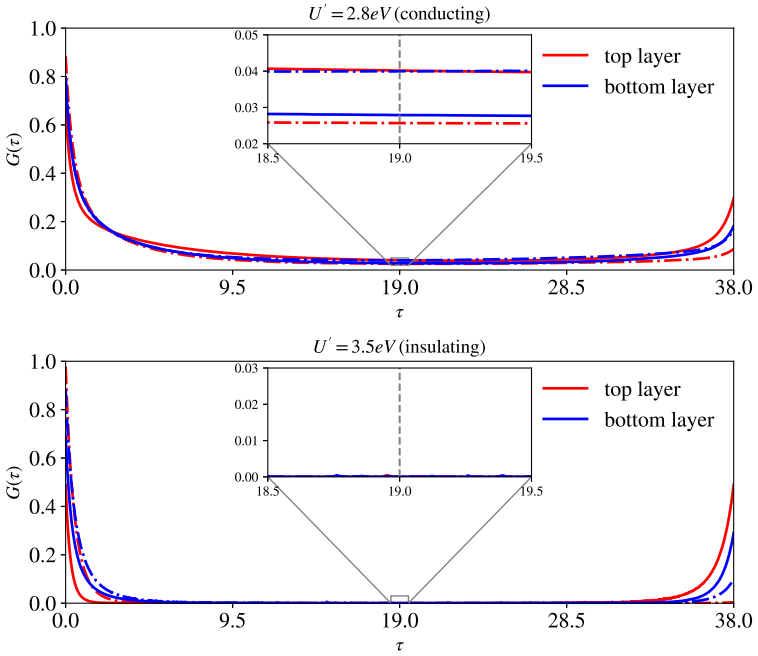

Figure 4.4: CTQMC sampled Green's function in imaginary times within the characteristic conducting and insulating phase. The *xy*-orbitals are drawn as solid lines while the *xz*(*yz*)-orbitals are drawn as dash-dotted lines. The top panel represents a characteristic conducting phase ($U' = 2.8$eV with finite values of $\overline{A(0)}$), while the bottom panel represents a characteristic insulating phase ($U' = 3.5$eV with $\overline{A(0)} = 0$).

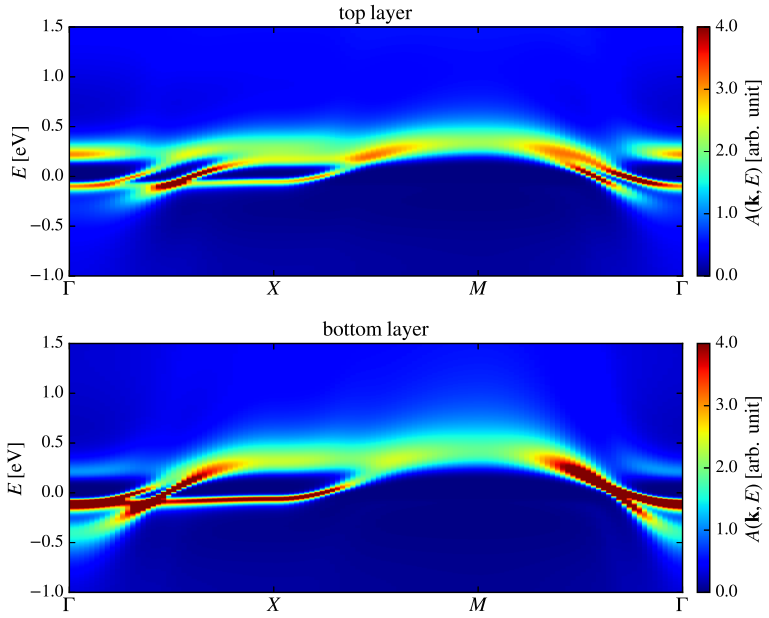

Figure 4.5: DMFT band-structure of $(SrVO_3)_2/(SrTiO_3)_4$ in the conducting phase ($U' = 2.8$eV) illustrated as heat plot constructed from analytically continued DMFT Green's functions. Each continuation is represented by a single vertical line $A(\mathbf{k}, \cdot)$ and was obtained for every k-point from their corresponding DMFT Green's functions using MaxEnt [60]. More specifically, we employ the so-called *classic* [78] variant using singular value decomposition to reduce the dimensionality of the search space. This data was provided by Josef Kaufmann.

4.3 DΓA results

The illustrated points in Fig. 4.4 were ultimately chosen to be further addressed by `AbinitioDΓA`. These exact two points are chosen because a) they represent the two characteristic domains, b) are symmetric around the hysteresis and c) include the value ($U' = 3.5$eV) found in cRPA or cLDA. Contrary to bulk $SrVO_3$ we expect much larger non-local correlation effects. This is well-founded, because the DMFT mapping to a local impurity surrounded by a bath, is an approximation for finitely many dimensions d which becomes exact in the limit $d \to \infty$. This approximation nonetheless works quite well for three dimensional materials but is much less reliable when going to two dimensions, which is the case here.

In order to apply the ladderDΓA approach implemented in `AbinitioDΓA` [20, 22, 23, 24] for the case under consideration, it first had to be extended to support inequivalent impurities. This extension was furthermore generalized so calculations with non-correlated p-orbitals are sup-

ported as well. The method at this point is however still restricted to orbital-diagonal hybridization functions (and thus impurity/local self-energies and one-particle Green's functions). Due to this non-mixing between orbitals and the two independent impurities, the computational effort, fortunately, only scales by a factor of 2 compared to bulk $SrVO_3$. We 'simply' have to calculate two separate effective 3-band models instead of the much more complex 6-band model.[21] This simplification however does not hold in `AbinitioDΓA` where, in terms of computational effort, there is no difference between these two cases. Despite the complex problem, as well as the low temperature under consideration, the `AbinitioDΓA` treatment, fortunately, remains feasible.

4.3.1 Conducting regime

In the following figures we treat the conducting point ($U = 4.3\text{eV}$) with $N \pm 60$ vertex frequencies in all directions; we did *not* extend the vertex via its asymptotic. For this specific case the vertex calculation remained the bottleneck of the treatment where for a full calculation (DFT+DMFT+`AbinitioDΓA`) a total of around $300,000$ CPU hours have to be invested (of which two thirds are solely used for the sampling of the vertex and asymptotic).[22] Extending the vertex to larger frequency boxes would shift the bottleneck back to `AbinitioDΓA` due to its more challenging frequency scaling.[23]

Figures 4.7 and 4.8 illustrate the properties of the (most important) *xy*-orbital of the impurity in the top layer while Figures 4.10 and 4.11 illustrate them for the bottom layer. Please note that due to the low hybridization between both the *xy*-orbitals and the rest (see Fig. 4.12) we are allowed to extract $Z_{\mathbf{k}}$ via $\frac{\partial \Im\Sigma(\mathbf{k},i\nu)}{\partial i\nu}\Big|_{i\nu\to 0^+} = \left(1 - Z_{\mathbf{k}}^{-1}\right)$, identical to bulk $SrVO_3$. For the *xz*- and *yz*-orbitals this is not the case anymore and an eigenvalue decomposition would be required.

In the impurity of the top layer we observe a comparably large momentum dependence in the quasi-particle weight $Z_{\mathbf{k}}$ of around 15% (bulk: 4%) The structure here, in a way, resembles the Fermi surface, which however is not quite at the point as we saw in bulk $SrVO_3$ at the same temperature ($\beta = 38\text{eV}^{-1}$) in Fig. 3.7. Nonetheless we see the same trend, i.e. $Z_{\mathbf{k}}$ is largest around the Fermi surface and smallest at the *M*-point (unoccupied states). The scattering rate looks to be similarly affected where we even find areas with $\gamma_{\mathbf{k}} \approx 0$ (around the Γ-point). We furthermore observe in Fig. 4.8 that $\gamma_{\mathbf{k}}$ also massively changes on the Fermi surface

[21] In the Kanamori parametrization the number of band-spin combinations that have to be sampled for the vertex scales with $N = \left[3n_{dim}^2 - 2n_{dim}\right] \times 6$.

[22] The calculations are done on the VSC-3 which is equipped with Intel Xeon E5-2650v2, 2.6 GHz processors.

[23] The involved matrices, which have to be inverted, are of size $n_{\text{dim}}^2 \times 2\nu_{\text{max}}$. Doubling the number of frequencies (via asymptotic) thus leads to approximately 10 times the required core-hours. [24]

(corresponding to the top layer) itself. The Fermi surface scattering rate positioned on the $\Gamma - M$ path is around 3 times larger compared to the point on the $\Gamma - X$ path which is an indication of an emerging of a so-called 'pseudogap'. The values of the self-energy at the first frequency shown in (a) and (b) of Fig. 4.7 can be best explained via Fig. 4.6. There we illustrate the real and imaginary parts of the DΓA self-energies at the high-symmetry points Γ, X and M, compared to the DFT+DMFT result (dashed lines). Due to the broken symmetry in the z-direction, the local DMFT self-energies are in turn orbital dependent and therefore show a different xy (dashed black) and yz/xz (dashed gray) contribution. The previously almost unaffected imaginary part shows, for the xy-orbital, a major momentum dependence where for all k-points the non-local corrections push all values downwards. At the M-point this effect is maximal with a difference at the peak of more than 200meV compared to DMFT. On the contrary the real-part shows a similar behaviour to bulk where we, yet again, see the same tendency regarding the (un-)occupied states. When previously the real-part split was around 200meV, we see here triple that, namely more than 600meV.

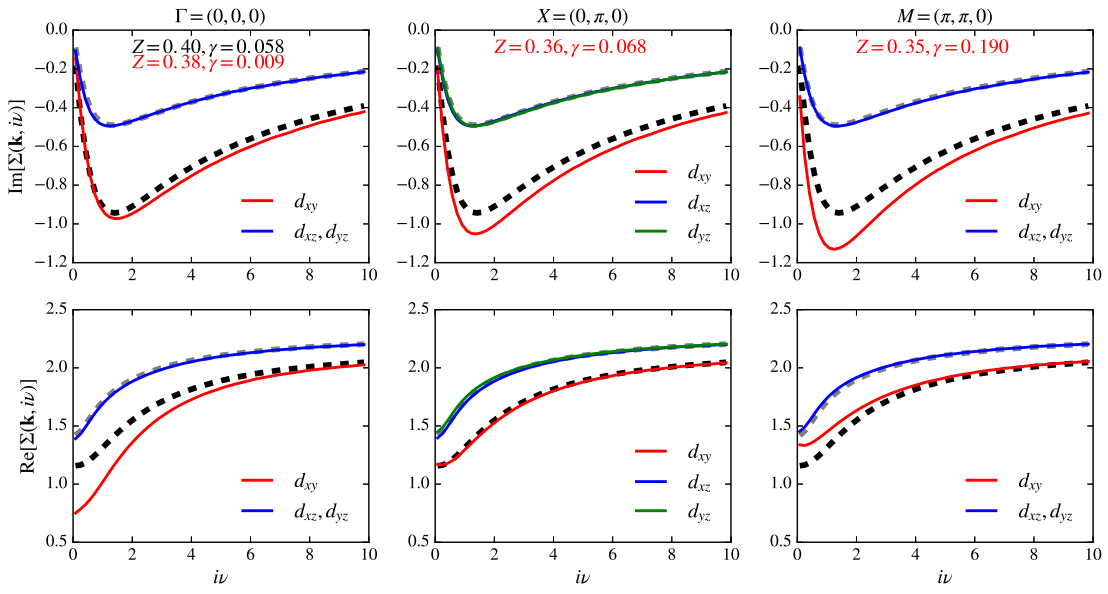

Figure 4.6: Imaginary (top panels) and real (bottom panels) part of the DΓA self-energies at the high symmetry points Γ, X and M in the top layer. The local (i.e. momentum independent) DMFT self-energies are illustrated as dashed black (xy-orbital) and dashed gray (xz/yz-orbitals) lines. The non-local DΓA self-energies split up depending on the k-point and are illustrated with different colors.

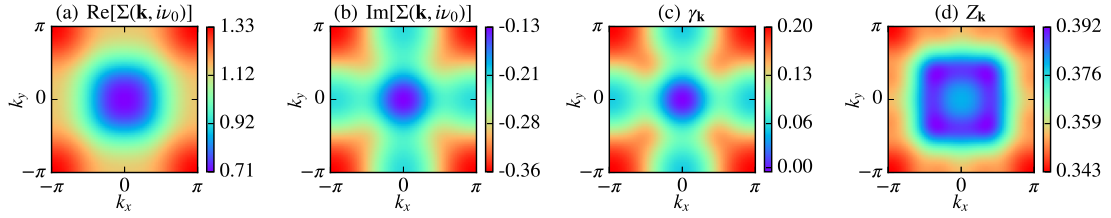

Figure 4.7: (a) Real and (b) imaginary parts of the momentum-dependent self-energy Σ at the first fermionic frequency $i\nu_0$. (c) Scattering rate $\gamma_{\mathbf{k}}$ and (d) quasi-particle weight $Z_{\mathbf{k}}$. The data shown here represents the *xy*-orbital of the impurity of the *top* layer of $(SrVO_3)_2/(SrTiO_3)_4$ calculated at room temperature by AbinitioDΓA.

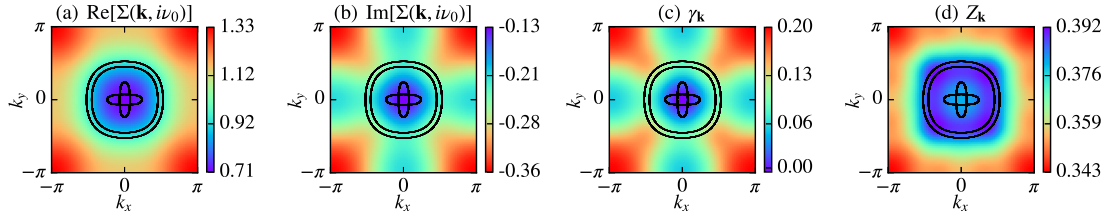

Figure 4.8: Same data as in Fig. 4.7 but with the LDA Fermi surface drawn on top of it. The outer ring represents the Fermi surface of the impurity of the top layer while the inner ring and the structure around $\mathbf{k} = (0, 0, 0)$ originate from the impurity of the bottom layer.

The impurity of the bottom layer shows overall less non-local effects where we see a trend towards bulk. This can be already seen in the DMFT results where the self-energy of the *xy*- and *xz*/*yz*-orbitals in Fig. 4.9 are almost identical (dashed black and gray lines respectively). Nonetheless the quasi-particle weight still shows a rather large momentum dependence of around 10% in the Brillouin zone. Compared to the top layer impurity the scattering rate is around three times smaller and shows quite a different structure which is however in somewhat of an agreement with the Fermi surface. The previously described pseudogap onset in the top layer can not be identified here. By again considering the full self-energies shown in Fig. 4.9 we see a surprisingly close result compared to bulk $SrVO_3$. The real part shows the same splitting of 200meV while the imaginary part also remains quite bulk-like.

Besides the already mentioned small hybridization between the two *xy* orbitals (shown in Fig. 4.12) we see a non-negligible hybridization between the other orbitals. The corresponding self-energies are considerably smaller with observed peak values of around −6meV. The comparably

large hybridization between the xz/yz orbitals of top and bottom layer can be easily explained by the characteristic of the involved Wannier functions. While the xz/yz-orbitals point towards the other layer and thus overlap, the xy-orbital lies flat inside the layer and thus the overlap is almost non-existent.

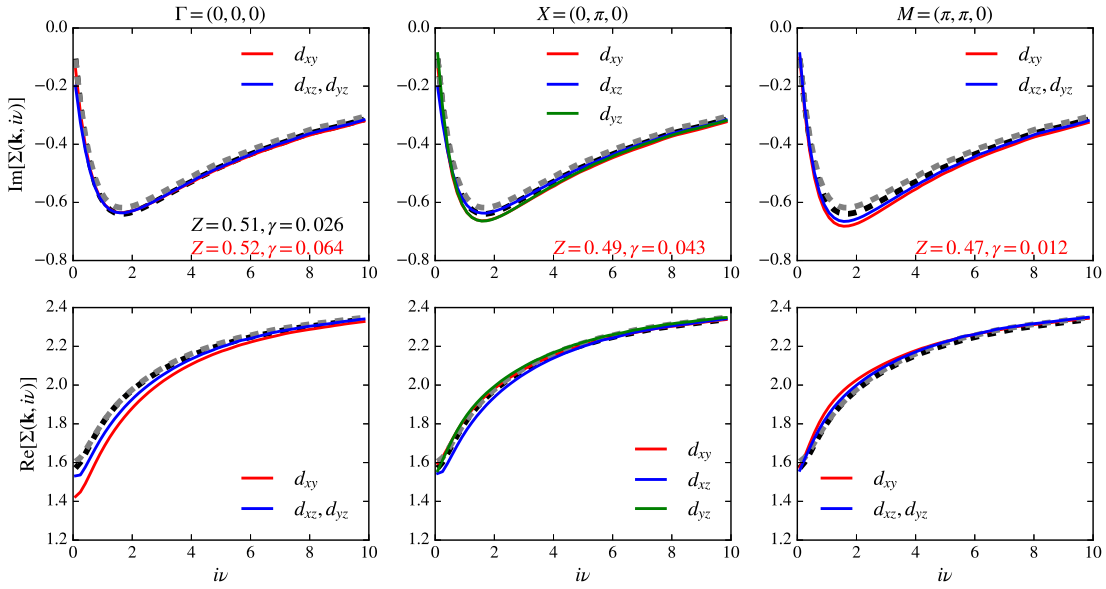

Figure 4.9: Imaginary (top panels) and real (bottom panels) of the DΓA self-energies in comparison to the DMFT self-energies. The color convention is identical to Fig. 4.6. Due to the more bulk-like behaviour of the bottom layer the two (xy - xz/yz) DMFT self-energies are almost identical. This furthermore also affects the DΓA self-energies resulting in less **k**-dependence.

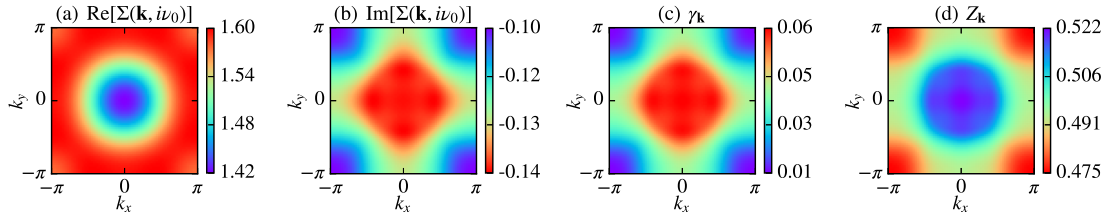

Figure 4.10: Same as Fig. 4.7 but for the xy-orbital of the impurity of the *bottom* layer.

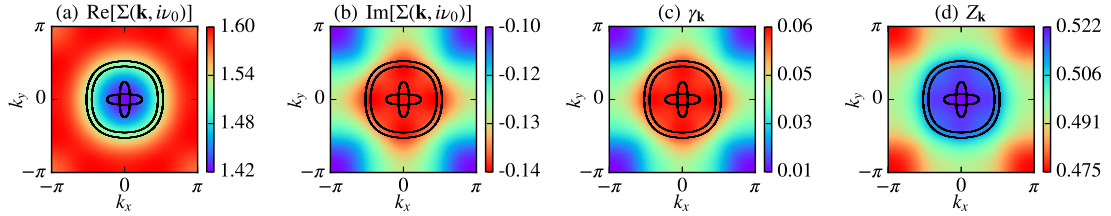

Figure 4.11: Same data as in Fig. 4.10 with the LDA Fermi surface drawn on top of it which is identical to the one illustrated in Fig. 4.8.

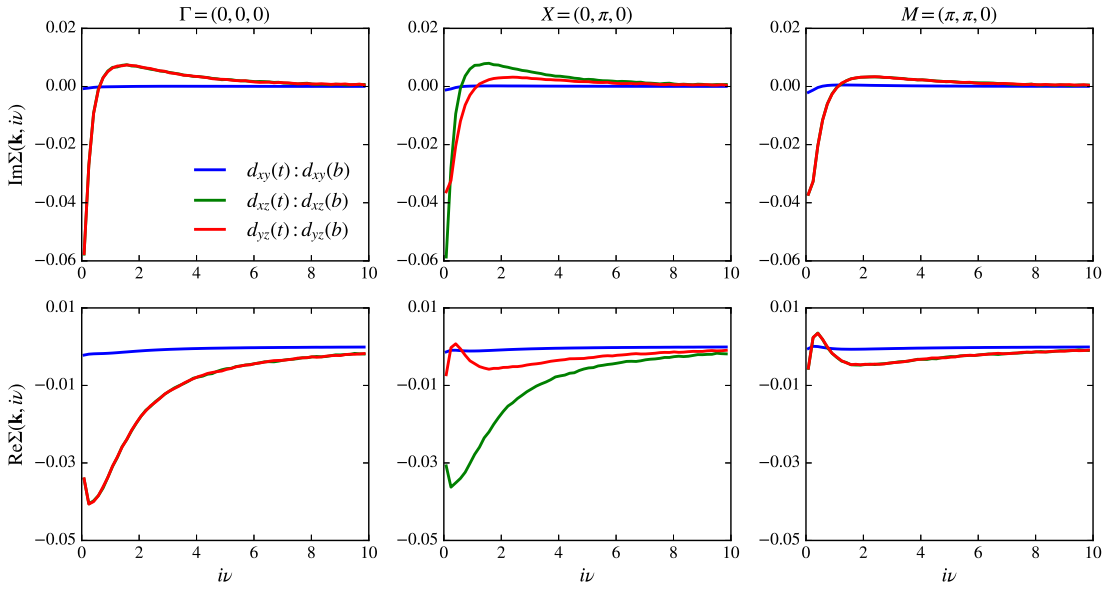

Figure 4.12: Imaginary (top panels) and real (bottom panels) part of the top-bottom layer off-diagonal self-energies. Shown here are only the non-vanishing contributions, i.e. the hybridization between equivalent orbitals between the top and bottom impurity. Similar to the previous Figures at Γ- and M-point the d_{xz}(top) : d_{xz}(bottom) contribution is identical to d_{yz}(top) : d_{yz}(bottom).

For completion we show here the orbital-resolved momentum-dependent susceptibilities. The data is extracted at the bosonic frequency $i\omega = 0$. We exploit the already described symmetry (i.e. $\chi_{1122} = \chi_{2211}$) and only show the upper triangle in Fig. 4.14 and 4.15. The orbitals are numbered $xy(t) \rightarrow xz(t) \rightarrow yz(t) \rightarrow xy(b) \rightarrow xz(b) \rightarrow yz(b)$ and thus the diagrams in the top left corner represent the top layer, the bottom right corner the bottom layer and the top right corner the off-impurity elements. Since the *local* full vertex F is sampled in CTQMC

which at the moment treats the impurities independently we only get small vertex contributions via the non-local Bethe-Salpeter equations (ladder construction with lattice propagators). For that reason they are considerably smaller compared to their diagonal counterparts. We see that the magnetic susceptibilities again dominate the density susceptibilities in terms of size which is further enhanced by the negative (positive) valued off-diagonal elements in the density (magnetic) channel. The largest contribution in the magnetic channel originates from the *xy*-orbital in the top layer where the other diagonal elements are by a factor of 3–9 smaller. In the density channel, on the contrary, the diagonal elements are much more evenly distributed. The physical susceptibilities, in comparison to bulk $SrVO_3$ are illustrated in Fig. 4.13. Each impurity, of either bulk or layered $SrVO_3$ (left three columns), shows comparably sized susceptibility values, albeit with vastly different momentum dependence. Here the bottom layer, despite its bulk-like self-energy behavior, has a mirrored structure compared to bulk. The off-impurity susceptibilities (forth column in Fig. 4.13) have non-vanishing contributions only in the magnetic channel where they even reach sizes which are comparable to bulk.

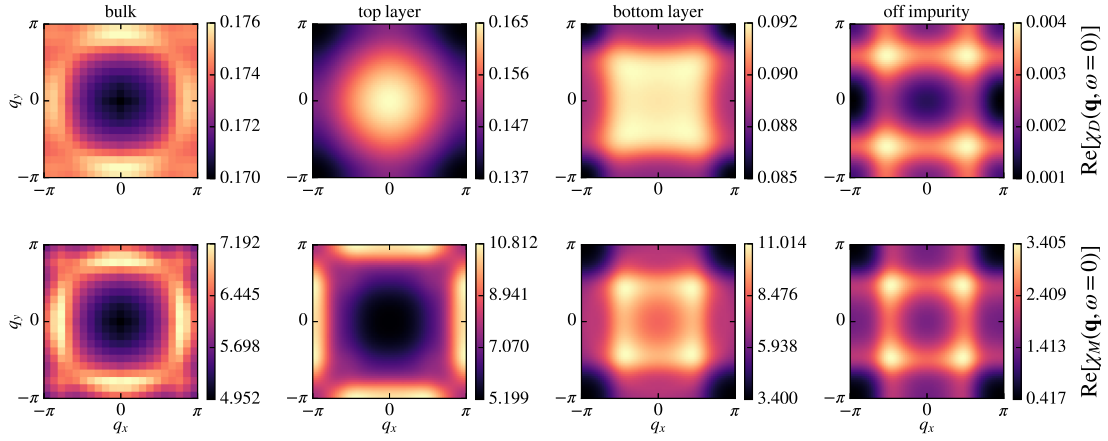

Figure 4.13: Comparison of the real parts of the *physical* density (top panels) and magnetic (bottom panels) susceptibilities between bulk $SrVO_3$ (first column) from chapter 3.1 and $(SrVO_3)_2/(SrTiO_3)_4$ (second to forth column) at $\beta = 38\mathrm{eV}^{-1}$. The bulk susceptibilities are shown in the $q_z = 0$ plane. Here the second column represents the contribution of the top $SrVO_3$ layer (summation indices $l, m \in$ top impurity according to Eqs. (3.7)), the third column the contribution of the bottom $SrVO_3$ layer and the fourth column the off-impurity contribution (summation index $l \in$ top impurity; $m \in$ bottom impurity).

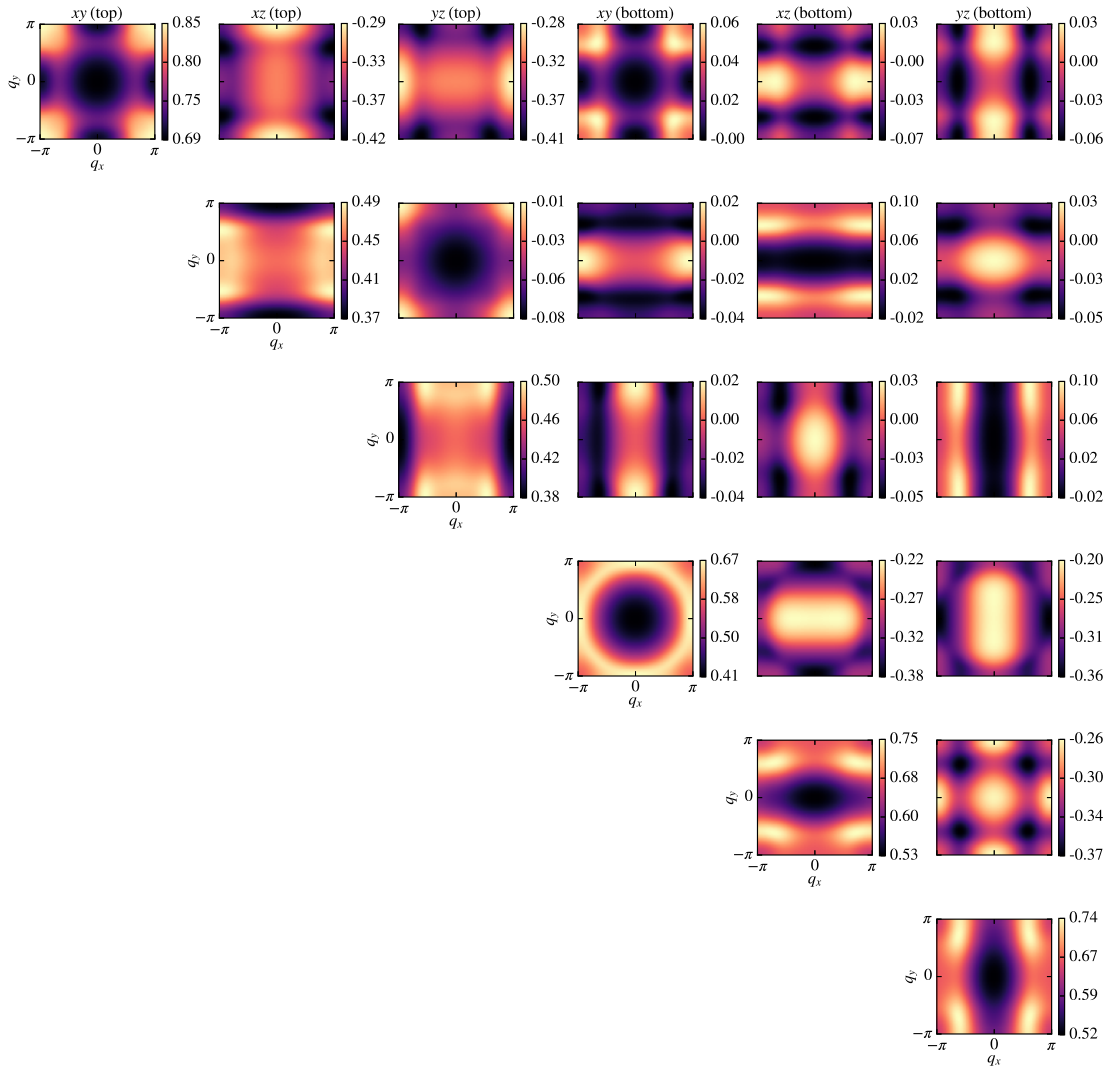

Figure 4.14: Orbital-resolved density susceptibilities $\chi_{D\ llmm}$ at $i\omega = 0$ vs q_x and q_y momentum illustrated in form of a matrix for the six orbitals and two layers. The lower triangle is not shown since it is symmetric in comparison to the upper triangle. Due to the way the orbital counting is done, the top left (cut-off) 3×3 block represents the impurity of the top layer while the bottom right (cut-off) 3×3 block represents the impurity of the bottom layer. The remaining 3×3 block in top right illustrates the off-impurity susceptibilities which on the *local* level inherently do not contain any vertex contributions (the local full vertex F is diagonal with respect to the layers). Note that the susceptibilities are plotted on different scales.

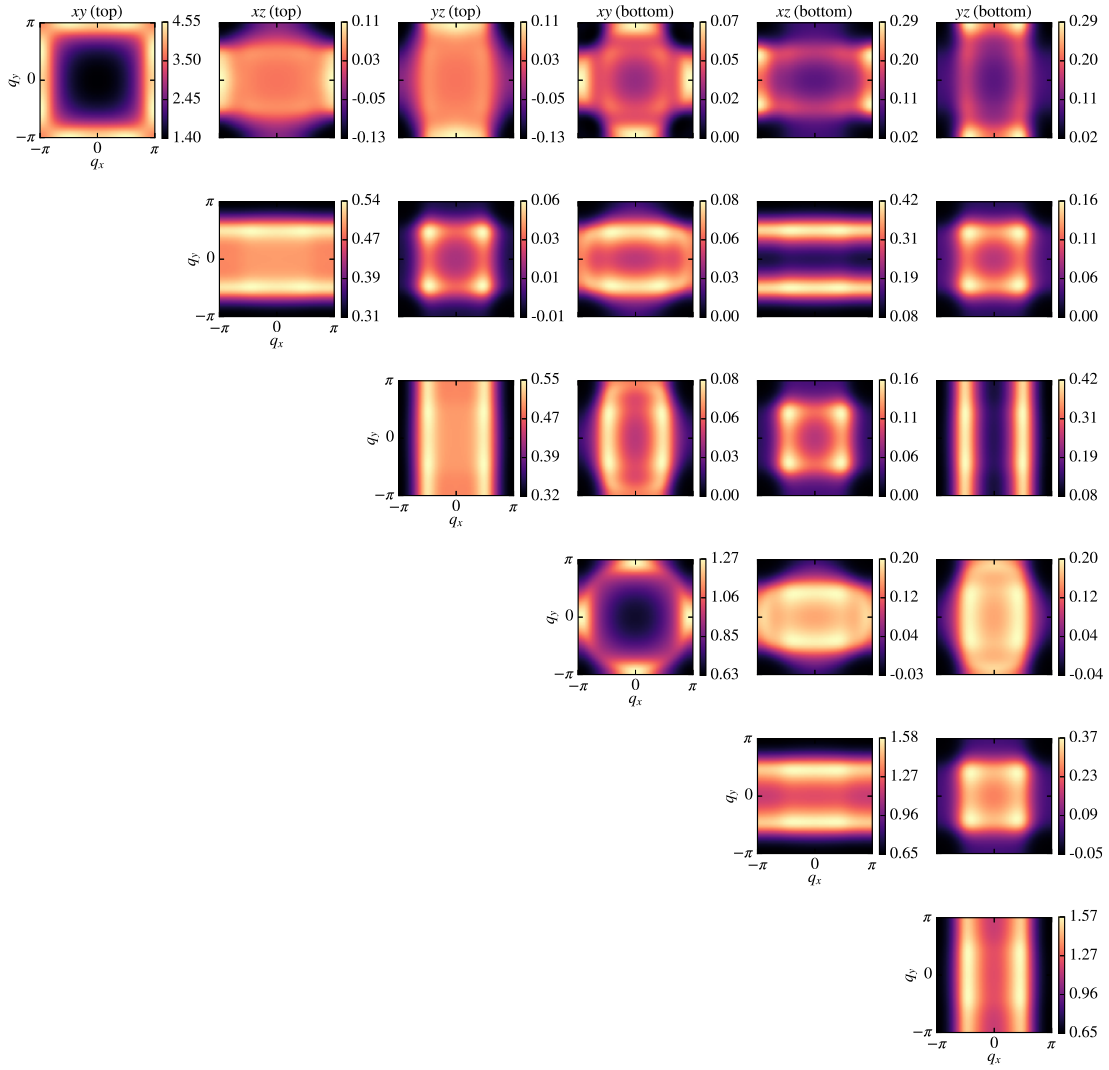

Figure 4.15: Same as Fig. 4.14 but now for the magnetic susceptibilities $\chi_{M\ llmm}$.

4.3.2 Insulating regime

In the insulating regime at $U = 5$eV the self-energy results are unfortunately found to be not utilizable. This behavior is illustrated in Figures 4.16 and 4.17. The *xy*-orbital in both the top and bottom layer are majorly affected. The top layer shows a self-energy reduction of approximately a factor of $3 - 4$ while the bottom layer shows an amplification of a factor of up to 5. Furthermore the real part of the bottom layer shows signs of a divergence at the lowest frequencies.

The diverged susceptibilities shown in Figs. 4.18, 4.19 and 4.20 suggest that we are in an ordered regime (most likely anti-ferromagnetism) in which our DΓA approach for the momentum-dependent self-energies ceases to work. These divergences are illustrated as small rings around the M-point ($\pi - \pi - 0$) which appear everywhere except for a few orbital combinations.

For a more detailed consideration we show both the density (left panels) and magnetic (right panels) at the diagonal contributions in Fig. 4.20 (for symmetry reasons we do not show the contributions 3333 and 6666). While in most panels the typical divergent characteristic is shown the initially suggested divergence-free components also display problems. In $\chi_{D\,2222}$ we observe a small kink around the typical divergence line which is more pronounced in $\chi_{M\,5555}$. The only seemingly unaffected contribution is $\chi_{M\,4444}$. However because of its size we can not be certain whether or not a similar kink appears (we would need a much finer k-mesh).

This result in turn suggests that, if we allowed for it, we would have probably already obtained antiferromagnetism in DMFT.[24]

[24] In all DMFT calculations done throughout this thesis we enforce paramagnetism.

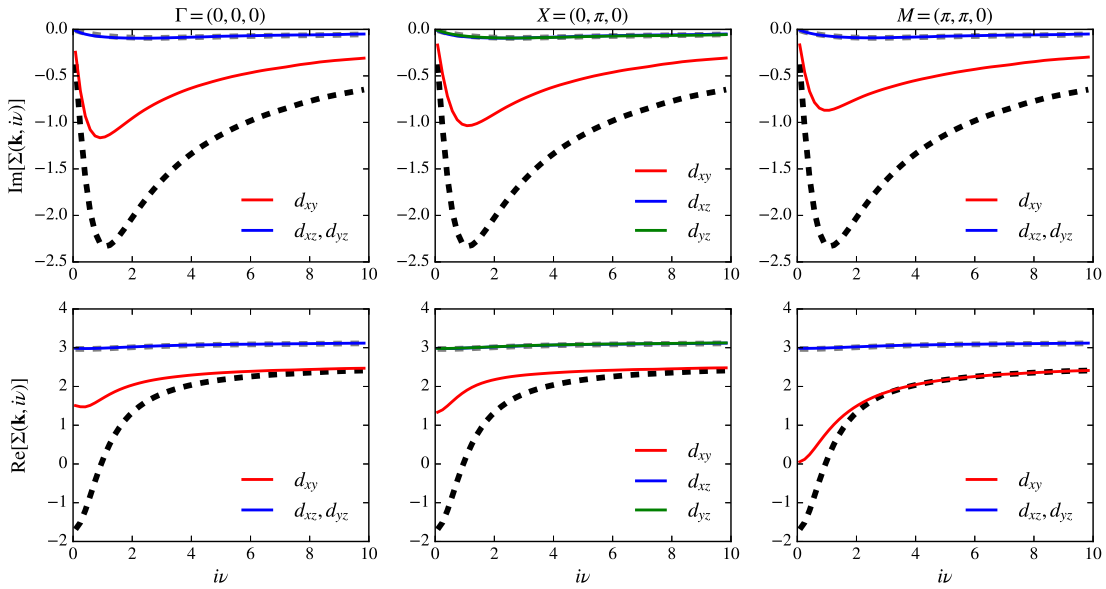

Figure 4.16: Imaginary (top panels) and real (bottom panels) part of the DΓA self-energies in the insulating phase at the top layer of $(SrVO_3)_2/(SrTiO_3)_4$. The colored graphs represent the DΓA self-energies which are compared to the DMFT solution (black (xy) and gray (xz/yz)).

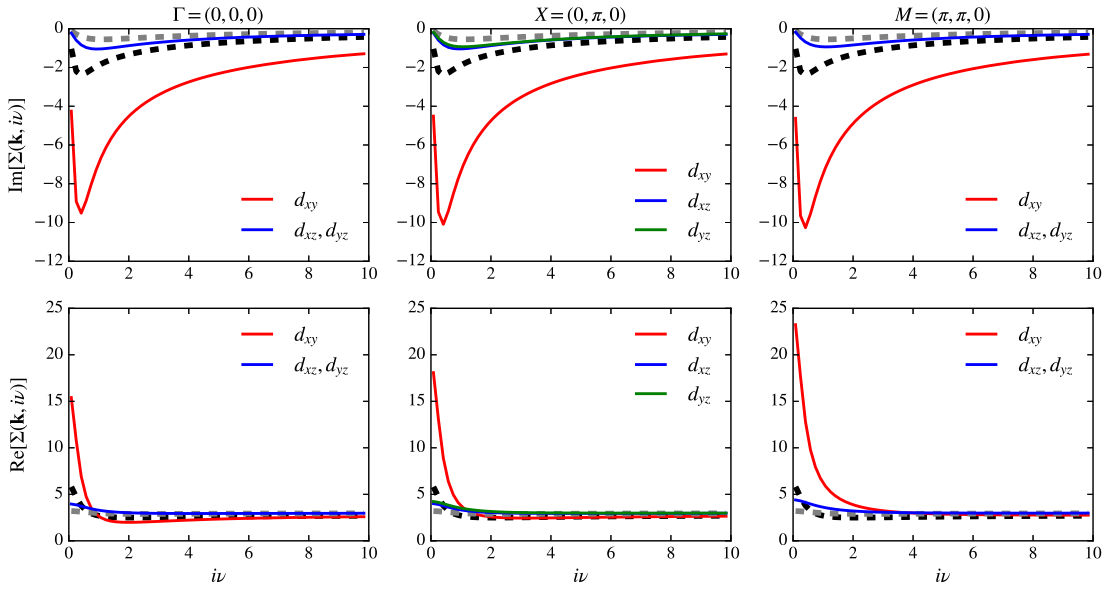

Figure 4.17: Same as 4.16 but now for the *bottom* layer.

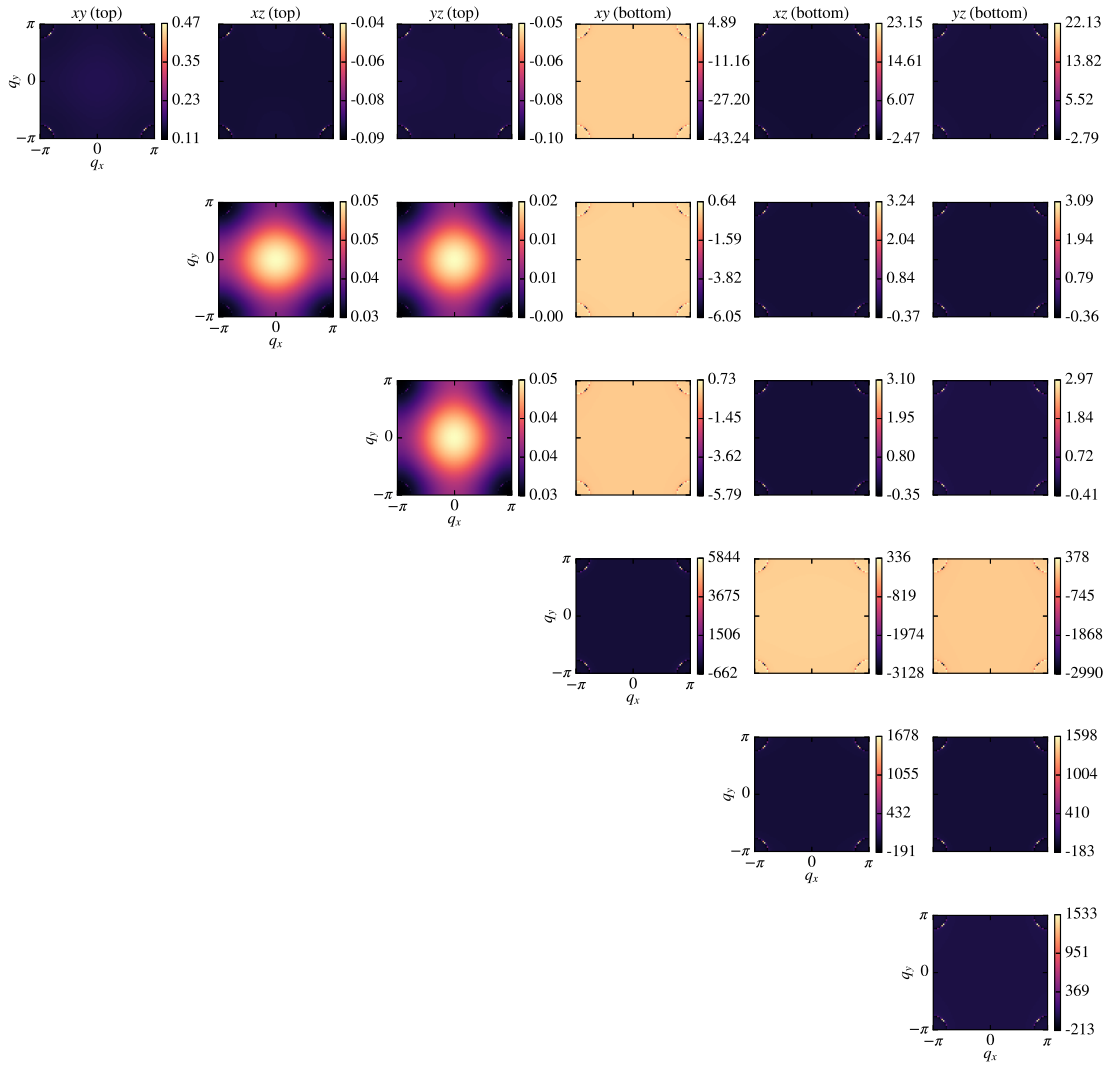

Figure 4.18: Orbital-resolved density susceptibilities $\chi_{D\,llmm}$ at $i\omega = 0$ illustrated in form of a matrix. In this insulating phase we mostly observe susceptibilities with a diverged characteristic (rings around the M-point $(\pi - \pi - 0)$). Same format as in Fig. 4.14.

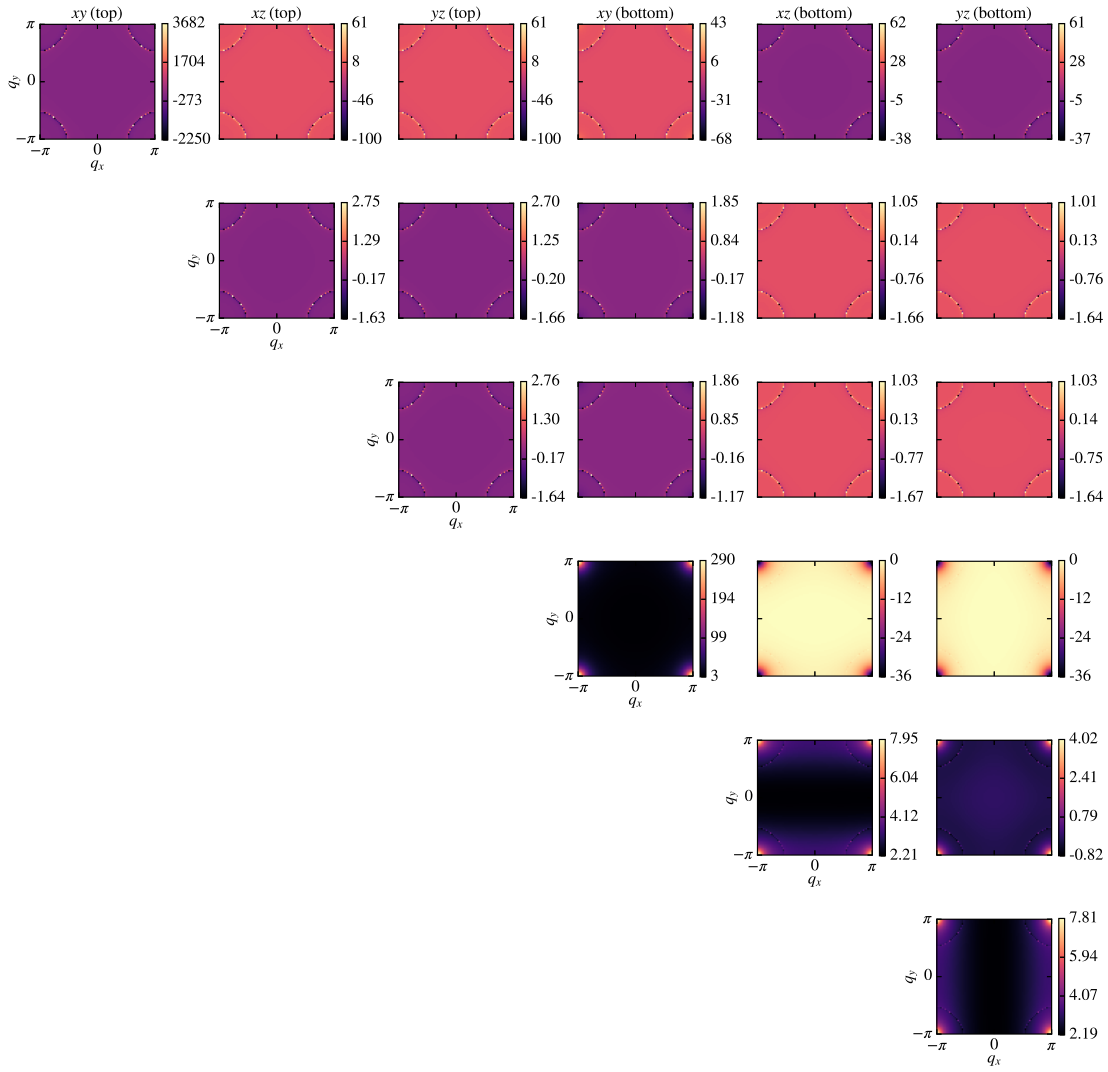

Figure 4.19: Same as Fig. 4.18 but now for the magnetic susceptibilities.

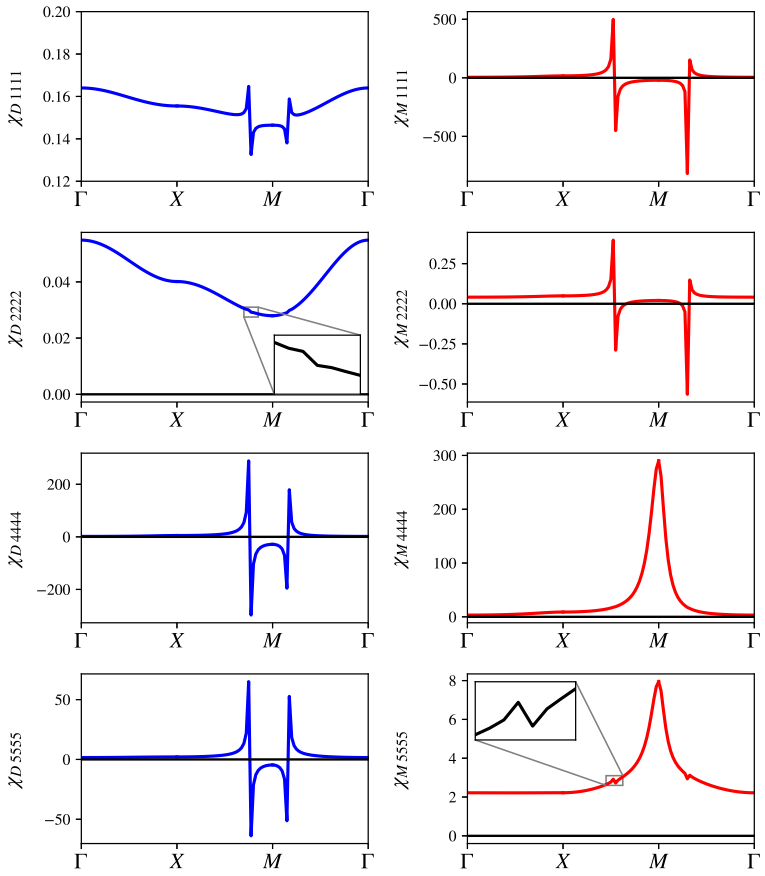

Figure 4.20: Diagonal contributions of the density and magnetic susceptibilities χ_{llll} in the insulating phase. For brevity we do not show the symmetric cases. The diverged characteristic as well as the negative susceptibilities (e.g. in the top right panel) suggest an ordered phase.

5 Summary and outlook

5.1 Summary

Starting from the many-body-problem in first quantization we bridged all the way to the state-of-the-art DFT+DMFT approach. This was mainly done by means of the introduced Green's functions formalism and Feynman diagrams. With the properties of one- and two-particle diagrams we reviewed the so-called dynamical vertex approximation (DΓA) and the, over the course of this thesis, used and furthered ladderDΓA implementation.

By extending the existing `AbinitioDΓA` project we were able to investigate bulk strontium vanadate ($SrVO_3$) with non-local interactions as well as study dimensionality effects in ultra-thin $SrVO_3$. We revisited the results from high temperature calculations for bulk $SrVO_3$ which showed a quasi-particle variation of around 2% in the Brillouin zone and a consistently larger scattering rate throughout. The main phenomena shown was the splitting of the real part of the self-energy where the occupied states were pushed energetically lower while the unoccupied states were pushed higher. At the first fermionic Matsubara frequency we saw a split of more than 200meV. This behavior looked to be unaffected by a major decrease in temperature where the size of the energy split almost remained identical. The main effect of this decrease was a sharpening of features near the Fermi-surface in all shown quantities. The quasi-particle weight, although exhibiting a larger momentum variation of 4%, remained quasi-local. This is consistent with current understanding, i.e. lower temperatures lead to less dominant local correlation effects. As a final point first calculations were performed with 'ab initio' non-local interactions $V(\mathbf{q})$. First evaluations showed that the quasi-particle weight was pushed towards less correlation (higher $Z_{\mathbf{k}}$). The real part showed a consistent trend where, again, unoccupied (occupied) states were pushed energetically higher (lower). Overall the results looked promising however there still remain problems regarding frequency box-size and k-mesh effects.

As a starting point for the study of dimensionality, we revisited (and replicated) the DFT+DMFT calculations for two-layered $SrVO_3$ on top of a $SrTiO_3$ substrate. We were able to confirm these recent findings and then chose to perform DΓA calculation for two characteristic points in the conducting and insulating regime. In the conducting regime ($U = 4.3$eV) we saw an increase of the quasi-particle weight $Z_{\mathbf{k}}$ variation w.r.t. bulk $SrVO_3$. This variation of around 15% (almost four times the size of bulk) is in particular more prominent on a relative scale due to the generally lower Z value found in the top layer. On the contrary, despite its 'bulk-like' behaviour, the bottom layer showed a similar momentum variation of 10% in Z. The largest non-local effect

remained in the real part of the DΓA self-energy. Compared to bulk $SrVO_3$ the energy split increased from 200meV to over 600meV. These observed effects in our system were only seen in the *xy*-orbitals with the *xz*/*yz*-orbitals remaining almost unaffected.

As a final point we attempted calculations for the insulating regime. However it was quickly discovered that the involved susceptibilities diverge, suggesting an ordered phase. As a consequence the resulting DΓA self-energies were not physical. The algorithm and the used channel decompositions used in the `AbinitioDΓA` formalism breaks down in such a phase.

5.2 Outlook

The ladderDΓA implementation present in `AbinitioDΓA` and the corresponding applications are at the frontier of material science. Results produced thus far look promising. However the implementation itself is still quite restricted. Due to the, already quite high computational effort (vertex sampling, asymptotic sampling, ladderDΓA) it is rather difficult to pinpoint future development directions without sacrificing applicability. Nonetheless we try to give some starting points regarding implementation generalizations and possible investigation areas.

Non-local interactions: The, in this context, for the first time used non-local interactions showed promising results (chapter 3.2). However there still remain many unanswered questions. The investigation of all involved box sizes, mesh and non-convergence effects may be a focus point in the near future to provide the best possible description. In this regard improvements of the CTQMC solver might be additionally necessary. Especially solutions for memory-bound problems such as the necessary Fourier transforms or improvements of the asymptotic vertices might come a long way.

Frequency-dependent interactions: One important piece missing from an 'ab initio' description are frequency dependent interaction, akin to GW descriptions [79, 80, 81]. So far they have been completely left out in `AbinitioDΓA` and are indeed necessary for a complete description of the involved interactions. To achieve such a description one would have to modify the interaction term used in the `AbinitioDΓA` derivation (Appendix D):

$$\hat{U}^{\text{full}}(\tau) = \frac{1}{2} \sum_{\substack{\mathbf{qkk'} \\ ll'mm' \\ \sigma\sigma'}} U^{\mathbf{qkk'}}_{lm'ml'} \hat{c}^{\dagger}_{\mathbf{k'-q},m'\sigma}(0) \hat{c}^{\dagger}_{\mathbf{k}l\sigma'}(\tau) \hat{c}_{\mathbf{k-q},m\sigma'}(\tau) \hat{c}_{\mathbf{k'}l'\sigma}(0) \times \delta_{ml}\delta_{m'l'} \tag{5.1}$$

With these (imaginary) time dependencies retarded density-density interactions would be supported giving access to even more phenomena. An even even greater generalization with re-

tarded Kanamori interactions in all three time arguments would however be preferable

$$\hat{U}^{\text{full}}(\tau_1,\tau_2,\tau_3) = \frac{1}{2}\sum_{\substack{\mathbf{qkk'}\\ ll'mm'\\ \sigma\sigma'}} U^{\mathbf{qkk'}}_{lm'ml'}\hat{c}^{\dagger}_{\mathbf{k'}-\mathbf{q},m'\sigma}(\tau_1)\hat{c}^{\dagger}_{\mathbf{k}l\sigma'}(\tau_2)\hat{c}_{\mathbf{k}-\mathbf{q},m\sigma'}(\tau_3)\hat{c}_{\mathbf{k'}l'\sigma}(0). \tag{5.2}$$

At this moment in time we however suspect that this would result in too much computational effort since hitherto only efficient CTQMC algorithms for Eq. (5.1) exist that use the segment code (see e.g. [49] for a segment algorithm description). Another route would be to include the frequency dependence only as a bare interaction vertex precisely the same way as we treat non-local correlations.

Moriyaesque λ-corrections or self-consistency: In order to conserve the occupation in the considered system and therefore retain a correct self-energy asymptotic, one would need to either implement so-called λ-corrections [55, 82] or use a self-consistency cycle (where one would need to update the chemical potential μ). Due to computational effort, the latter is only realistically possible for high temperatures and a low number of bands. The former could be applied on the same level as the non-local interaction vertex, i.e. in its most trivial case

$$\Gamma^{qkk'}_{\substack{lmm'l'\\ \sigma\sigma'}} \equiv \Gamma^{\omega\nu\nu'}_{\substack{lmm'l'\\ \sigma\sigma'}} + \mathbf{V}^{\mathbf{qkk'}}_{\substack{lmm'l'\\ \sigma\sigma'}} + \lambda. \tag{5.3}$$

However even if λ were orbital/spin/frequency/momentum-independent, finding the correct λ value would not be straight forward.

Non-diagonal hybridization functions: In the current `AbinitioDΓA` implementation all *DMFT* Green's functions and self-energies must be orbital diagonal. Recent implementations of non-diagonal hybridization functions in `w2dynamics` [50] give access to more generalized data. In bulk $SrVO_3$ (chapter 3) this would have no effect. Albeit in other systems, e.g. the ultra-thin $SrVO_3$ films used in this thesis, orbital hybridization already on the DMFT level could have major effects on the DΓA results.

Investigation of near-phase transitions: In chapter 4 we already came across a first order phase transition and our calculations showed that in its equilibrium state, ultra-thin $SrVO_3$ suggests an ordered state. From there it is principally straight-forward to investigate proximity effects of near-phase transitions in combination with dimensionality effects. One would have to either perform calculation in the area of the hysteresis (movement along the hysteresis via the interaction parameter U') or perform calculations with variable temperature. Since the insulating regime can be described by an effective one-band model we could possibly also make excellent connections to other (one-band) model calculations.

Appendix A Quantum mechanic representations

As a basic quantum mechanics introduction we revise the most commonly used representations in literature as well as in this thesis.

Schrödinger representation: The system is described with time dependent wave functions and, generally, time independent operators. The exception is, of course, the explicitly time dependent time evolution operator $\hat{U} = e^{\frac{-i\hat{H}t}{\hbar}}$. The Schrödinger equation in this representation can be written in its famous form as

$$\hat{H}\left|\psi(t)\right\rangle = E\left|\psi(t)\right\rangle = i\hbar\frac{d}{dt}\left|\psi(t)\right\rangle, \tag{A.1}$$

with a general expectation value A calculated via

$$\langle A(t)\rangle = \langle\psi_S(t)|\, A_S\, |\psi_S(t)\rangle \tag{A.2}$$

and the time dependent wave function calculated with the above mentioned unitary time evolution operator

$$\left|\psi_S(t)\right\rangle = \hat{U}\left|\psi_S(0)\right\rangle = e^{-\frac{i}{\hbar}\hat{H}t}\left|\psi_S(0)\right\rangle. \tag{A.3}$$

Heisenberg representation: Any expectation value can theoretically be measured and therefore must not depend on the representation used to calculate it:

$$\begin{aligned}\langle A(t)\rangle &= \langle\psi_S(t)|\, A_S\, |\psi_S(t)\rangle \\ &= \langle\psi_S(t)|\, \hat{U}\hat{U}^\dagger A_S\, \hat{U}\hat{U}^\dagger\, |\psi_S(t)\rangle \\ &= \langle\psi_S(0)|\, \hat{U}^\dagger A_S\, \hat{U}\, |\psi_S(0)\rangle \\ &= \langle\psi_H|\, A_H(t)\, |\psi_H\rangle\end{aligned} \tag{A.4}$$

By inserting the identity $UU^\dagger = 1$, we were able to change our representation and got the Heisenberg wave function and operator

$$\left|\psi_H\right\rangle \equiv \hat{U}^\dagger\left|\psi_S(t)\right\rangle = \left|\psi_S(0)\right\rangle \tag{A.5}$$

$$A_H(t) \equiv \hat{U}^\dagger A_S\, \hat{U}, \tag{A.6}$$

where we transferred the time dependence from the wave functions to the operators. This time

dependence is now characterized by an equation of motion

$$\begin{aligned}\frac{d}{dt}A_H(t) &= \frac{d}{dt}U^\dagger A_S(t)U \\ &= \frac{d}{dt}\left(\hat{U}^\dagger\right)A_S\hat{U} + \hat{U}^\dagger A_S\frac{d}{dt}\left(\hat{U}\right) + \hat{U}^\dagger\frac{d}{dt}\left(A_S\right)\hat{U} \\ &= \frac{i}{\hbar}\hat{H}\hat{U}^\dagger A_S\hat{U} - \hat{U}^\dagger A_S\frac{i}{\hbar}\hat{H}\hat{U} + \frac{\partial}{\partial t}A_H(t) \\ &= \frac{i}{\hbar}\hat{U}^\dagger\left[\hat{H}, A_S\right]\hat{U} + \frac{\partial}{\partial t}A_H(t) \\ &= \frac{1}{i\hbar}\hat{U}^\dagger\left[A_S, \hat{H}\right]\hat{U} + \frac{\partial}{\partial t}A_H(t),\end{aligned} \tag{A.7}$$

where the last term is only present in case of an explicitly time dependent operator $A_S(t)$. In this context one can perform a Wick rotation $t \to -i\tau$, sets $\hbar = 1$ and assumes no explicit time dependence of the Schrödinger operator $A_S(t) = A_S(0)$. This way we get a slightly different equation of motion often used throughout this thesis.

$$\begin{aligned}\frac{d}{d(-i\tau)}A_H(\tau) &= \frac{1}{i}e^{\tau\hat{H}}[A_S, \hat{H}]e^{-\tau\hat{H}} \\ \frac{d}{d\tau}A_H(\tau) &= e^{\tau\hat{H}}[\hat{H}, A_S]e^{-\tau\hat{H}}.\end{aligned} \tag{A.8}$$

Interaction representation: As a third representation we introduce the interaction representation. It is a mixture of both the Schrödinger and the Heisenberg representation, often used in time dependent perturbation theory and scattering theory. We split the Hamiltonian in a time independent and a time dependent part

$$\hat{H} = \hat{H}_0 + V(t). \tag{A.9}$$

A derivation similar to the one we did in the Heisenberg representation yields

$$\begin{aligned}\langle A\rangle &= \langle\psi_S(t)|\, A_S\, |\psi_S(t)\rangle \\ &= \langle\psi_S(t)|\, \hat{U}_0\hat{U}_0^\dagger A_S\, \hat{U}_0\hat{U}_0^\dagger\, |\psi_S(t)\rangle \\ &= \langle\psi_I(t)|\, \hat{U}_0^\dagger A_S\, \hat{U}_0\, |\psi_I(t)\rangle \\ &= \langle\psi_I(t)|\, A_I(t)\, |\psi_I(t)\rangle\,,\end{aligned} \tag{A.10}$$

with

$$|\psi_I(t)\rangle \equiv \hat{U}_0^\dagger\, |\psi_S(t)\rangle \tag{A.11}$$

$$A_I(t) \equiv \hat{U}_0^\dagger A_S(t)\hat{U}_0. \tag{A.12}$$

Here $\hat{U}_0$ is the time evolution operator of the time independent part of the Hamiltonian $\hat{H}_0$. The equation of motion is then given by

$$\frac{d}{dt}A_I(t) = \frac{1}{i\hbar}\hat{U}_0^\dagger \left[A_S, \hat{H}_0\right] \hat{U}_0 + \frac{\partial}{\partial t}A_I(t) \tag{A.13}$$

and the time evolution of the interaction wave functions can be derived by

$$\begin{aligned}
i\hbar\partial_t |\psi_S(t)\rangle &= \hat{H} |\psi_S(t)\rangle \\
i\hbar\partial_t \hat{U}_0 |\psi_I(t)\rangle &= \hat{H}\hat{U}_0 |\psi_I(t)\rangle \\
\hat{H}_0\hat{U}_0 |\psi_I(t)\rangle + i\hbar\hat{U}_0\partial_t |\psi_I(t)\rangle &= \hat{H}_0\hat{U}_0 |\psi_I(t)\rangle + V(t)\hat{U}_0 |\psi_I(t)\rangle \\
i\hbar\partial_t |\psi_I(t)\rangle &= \hat{U}_0^\dagger V_S(t)\hat{U}_0 |\psi_I(t)\rangle = V_I(t) |\psi_I(t)\rangle .
\end{aligned} \tag{A.14}$$

Appendix B Matsubara Green's functions

B.1 Definition

We define the general n-particle Green's function in imaginary time as

$$G^n_{i_1,\dots,i_{2n}}(\tau_1,\dots,\tau_{2n}) = (-1)^n \left\langle \mathcal{T}\left[\hat{c}_{i_1}(\tau_1)\hat{c}^\dagger_{i_2}(\tau_2)\dots\hat{c}_{i_{2n-1}}(\tau_{2n-1})\hat{c}^\dagger_{i_{2n}}(\tau_{2n})\right]\right\rangle, \tag{B.1}$$

with time dependent fermionic annihilation / creation (Heisenberg) operators defined in Appendix A

$$\hat{c}^{(\dagger)}(t) = \hat{U}^\dagger \hat{c}^{(\dagger)}\hat{U} = e^{i\hat{H}t}\hat{c}^{(\dagger)}e^{-i\hat{H}t} \tag{B.2}$$

$$\hat{c}^{(\dagger)}(\tau) = \hat{U}^\dagger \hat{c}^{(\dagger)}\hat{U} = e^{\hat{H}\tau}\hat{c}^{(\dagger)}e^{-\hat{H}\tau}. \tag{B.3}$$

For normal time arguments one would only need to define either the annihilation or the creation operator since

$$\hat{c}^\dagger(t) = (\hat{c}(t))^\dagger, \tag{B.4}$$

however for imaginary times this statement does not hold anymore and both definitions are required ($e^{\pm\tau\hat{H}}$ is not unitary anymore)

$$\hat{c}^\dagger(\tau) \neq (\hat{c}(\tau))^\dagger. \tag{B.5}$$

Additionally we used the grand canonical expectation value[25]

$$\langle\cdots\rangle = \mathrm{Tr}\,\langle\rho\cdots\rangle = \frac{1}{Z}\mathrm{Tr}\left(e^{-\beta\hat{H}}\cdots\right) = \frac{1}{Z}\sum_n \langle n|\, e^{-\beta\hat{H}}\cdots|n\rangle. \tag{B.6}$$

with ρ as the density matrix and Z as the partition function defined by

$$Z = \sum_n \langle n|\, e^{-\beta\hat{H}}\,|n\rangle = \mathrm{Tr}\left(e^{-\beta\hat{H}}\right). \tag{B.7}$$

Here $|n\rangle$ and E_n represent the eigenstates and eigenvalues of the operator $\hat{H} - \mu\hat{N}$ (written as $\hat{H}$) so that

$$\hat{H}\,|n\rangle = E_n\,|n\rangle. \tag{B.8}$$

Finally, the time ordering operator $\mathcal{T}$ orders the operators from left to right according to their imaginary time argument (from largest to smallest)

$$\mathcal{T}\left[c^{(\dagger)}_1(\tau_1)c^{(\dagger)}_2(\tau_2)\right] = \left[c^{(\dagger)}_1(\tau_1)c^{(\dagger)}_2(\tau_2)\right]\Theta(\tau_1-\tau_2) - \left[c^{(\dagger)}_2(\tau_2)c^{(\dagger)}_1(\tau_1)\right]\Theta(\tau_2-\tau_1). \tag{B.9}$$

This ordering is done by switching operator positions which is accompanied by an additional (-1) for each exchange.

[25] In the grand canonical ensemble the weighting factor is $e^{-\beta(\hat{H}-\mu\hat{N})}$ and not $e^{-\beta\hat{H}}$. In order to be more concise we implicitly mean $\hat{H} - \mu\hat{N}$ when writing $\hat{H}$ from now on.

B.2 Boundaries

Without loss of generality we can assume that the operators are ordered from largest to smallest imaginary time.

$$\begin{aligned} G^n_{i_1,\ldots,i_{2n}}(\tau_1,\ldots,\tau_{2n}) &= \frac{(-1)^n}{Z}\sum_m \langle m|\, e^{-\beta\hat{H}}\hat{c}_{i_1}(\tau_1)\hat{c}^\dagger_{i_2}(\tau_2)\ldots\hat{c}_{i_{2n-1}}(\tau_{2n-1})\hat{c}^\dagger_{i_{2n}}(\tau_{2n})\,|m\rangle \\ &= \frac{(-1)^n}{Z}\sum_m e^{(-\beta+\tau_1-\tau_{2n})E_m}\,\langle m|\,\hat{c}_{i_1}e^{-\hat{H}\tau_1}\hat{c}^\dagger_{i_2}(\tau_2)\ldots\hat{c}_{i_{2n-1}}(\tau_{2n-1})e^{\hat{H}\tau_{2n}}\hat{c}^\dagger_{i_{2n}}\,|m\rangle \end{aligned} \tag{B.10}$$

After evaluating the outermost operators we arrived at a prefactor of $e^{(-\beta+\tau_1-\tau_{2n})E_m}$. Since for an infinitely large system the eigenvalues E_m can also become infinitely large we have to ensure that this prefactor is of suppressing nature. This way we always get a sum that is convergent.

$$-\beta+\tau_1-\tau_{2n}<0 \tag{B.11}$$

Taking into account our first assumption of time ordered operators we can rewrite this into

$$\tau_{2n}+\beta>\tau_1>\ldots>\tau_{2n}, \tag{B.12}$$

which expresses that all time arguments have to be within an interval of the length of β. Using the cyclic property of the trace ($\mathrm{Tr}\,[ABCD] = \mathrm{Tr}\,[DABC] = \cdots$) we can impose further restrictions:

$$\begin{aligned} G^n_{i_1,\ldots,i_{2n}}(\tau_1,\ldots,\tau_{2n}) &= \frac{(-1)^n}{Z}\sum_m \langle m|\, e^{-\beta\hat{H}}\hat{c}_{i_1}(\tau_1)\hat{c}^\dagger_{i_2}(\tau_2)\ldots\hat{c}_{i_{2n-1}}(\tau_{2n-1})\hat{c}^\dagger_{i_{2n}}(\tau_{2n})\,|m\rangle \\ &= \frac{(-1)^n}{Z}\sum_m \langle m|\, e^{-\beta\hat{H}}\hat{c}^\dagger_{i_2}(\tau_2)\ldots\hat{c}^\dagger_{i_{2n}}(\tau_{2n})e^{-\beta\hat{H}}\hat{c}_{i_1}(\tau_1)e^{\beta\hat{H}}\,|m\rangle \\ &= \frac{(-1)^n}{Z}\sum_m \langle m|\, e^{-\beta\hat{H}}\hat{c}^\dagger_{i_2}(\tau_2)\ldots\hat{c}^\dagger_{i_{2n}}(\tau_{2n})\hat{c}_{i_1}(\tau_1-\beta)\,|m\rangle \\ &= -\frac{(-1)^n}{Z}\sum_m \langle m|\, e^{-\beta\hat{H}}\hat{c}_{i_1}(\tau_1-\beta)\hat{c}^\dagger_{i_2}(\tau_2)\ldots\hat{c}_{i_{2n-1}}(\tau_{2n-1})\hat{c}^\dagger_{i_{2n}}(\tau_{2n})\,|m\rangle \\ &= -G^n_{i_1,\ldots,i_{2n}}(\tau_1-\beta,\ldots,\tau_{2n}) \end{aligned} \tag{B.13}$$

$$
\begin{aligned}
G^n_{i_1,\ldots,i_{2n}}(\tau_1,\ldots,\tau_{2n}) &= \frac{(-1)^n}{Z}\sum_m \langle m|\, e^{-\beta\hat{H}}\hat{c}_{i_1}(\tau_1)\hat{c}^\dagger_{i_2}(\tau_2)\ldots\hat{c}_{i_{2n-1}}(\tau_{2n-1})\hat{c}^\dagger_{i_{2n}}(\tau_{2n})\,|m\rangle \\
&= \frac{(-1)^n}{Z}\sum_m \langle m|\, e^{-\beta\hat{H}}e^{\beta\hat{H}}\hat{c}^\dagger_{i_{2n}}(\tau_{2n})e^{-\beta\hat{H}}\hat{c}_{i_1}(\tau_1)\ldots\hat{c}_{i_{2n-1}}(\tau_{2n-1})\,|m\rangle \\
&= \frac{(-1)^n}{Z}\sum_m \langle m|\, e^{-\beta\hat{H}}\hat{c}^\dagger_{i_{2n}}(\tau_{2n}+\beta)\hat{c}_{i_1}(\tau_1)\ldots\hat{c}_{i_{2n-1}}(\tau_{2n-1})\,|m\rangle \\
&= -\frac{(-1)^n}{Z}\sum_m \langle m|\, e^{-\beta\hat{H}}\hat{c}_{i_1}(\tau_1)\hat{c}^\dagger_{i_2}(\tau_2)\ldots\hat{c}_{i_{2n-1}}(\tau_{2n-1})\hat{c}^\dagger_{i_{2n}}(\tau_{2n}+\beta)\,|m\rangle \\
&= -G^n_{i_1,\ldots,i_{2n}}(\tau_1,\ldots,\tau_{2n}+\beta)
\end{aligned}
\tag{B.14}
$$

Here we used $(2n-1)$ operator exchanges leading to an additional (-1) and arrived at the Kubo-Martin-Schwinger (KMS) boundary conditions. It is important to note here that this derivation was done with already time ordered operators (i.e. τ_1 is the largest and τ_{2n} is the smallest imaginary time) which means that the KMS conditions only apply to exactly these properties. Other starting configurations could possibly mean that we end up outside the domain of the definition of the Green's function.

B.3 Crossing and swapping symmetry

Besides the time- and space translational symmetry, which lead to energy and momentum conservation respectively, two of the most often used symmetries in this thesis are the crossing and the swapping symmetry. By exchanging a pair of annihilation or creation operators in the general n-particle Green's function

$$
G^n_{i_1,\ldots,i_{2n}}(\tau_1,\ldots,\tau_{2n}) = (-1)^n\left\langle \mathcal{T}\left[\hat{c}_{i_1}(\tau_1)\hat{c}^\dagger_{i_2}(\tau_2)\ldots\hat{c}_{i_{2n-1}}(\tau_{2n-1})\hat{c}^\dagger_{i_{2n}}(\tau_{2n})\right]\right\rangle, \tag{B.15}
$$

we have to perform $(2k-1)$ swapping operations resulting in an additional factor (-1). Subsequently we get

$$
G^n_{i_1,\ldots,i_i,\ldots,i_j,\ldots,i_{2n}}(\tau_1,\ldots,\tau_i,\ldots,\tau_j,\ldots,\tau_{2n}) \overset{\text{CR}}{=} -G^n_{i_1,\ldots,i_j,\ldots,i_i,\ldots,i_{2n}}(\tau_1,\ldots,\tau_j,\ldots,\tau_i,\ldots,\tau_{2n}). \tag{B.16}
$$

Swapping symmetry on the other hand is often used in the context of two-particle Green's function. By applying crossing symmetry on both the incoming and outgoing particles, accompanied with $(-1)^2$, we get

$$
G^2_{i_1,i_2,i_3,i_4}(\tau_1,\tau_2,\tau_3,\tau_4) \overset{\text{SW}}{=} G^2_{i_3,i_4,i_1,i_2}(\tau_3,\tau_4,\tau_1,\tau_2). \tag{B.17}
$$

Thus these symmetries are more properties of the fermionic annihilation/creation operators rather than pure symmetries themselves.

B.4 Properties of the one-particle Green's function

The one-particle Green's function presents the simplest one while also displaying some interesting features. $G^1_{i_1,i_2}(\tau)$ is defined in the time interval $(-\beta,\beta)$ while the negative arguments can be restored via the KMS condition of Eq. (B.13)

$$G^1_{i_1,i_2}(\tau-\beta) = -G^1_{i_1,i_2}(\tau) \tag{B.18}$$

with $\tau \in [0,\beta)$. The function takes, depending on the involved spin band indices, a step of 1 when τ changes from negative to positive.

$$\begin{aligned} G^1_{i_1,i_2}(0^+) &= -\left\langle \mathcal{T}\left[\hat{c}_{i_1}(0^+)\hat{c}^\dagger_{i_2}(0)\right]\right\rangle \\ &= -\left\langle \hat{c}_{i_1}(0)\hat{c}^\dagger_{i_2}(0)\right\rangle = n_{i_2,i_1} - \delta_{i_1,i_2} \\ G^1_{i_1,i_2}(0^-) &= -\left\langle \mathcal{T}\left[\hat{c}_{i_1}(0^-)\hat{c}^\dagger_{i_2}(0)\right]\right\rangle \\ &= \left\langle \hat{c}^\dagger_{i_2}(0)\hat{c}_{i_1}(0)\right\rangle = n_{i_2,i_1} \end{aligned} \tag{B.19}$$

$$G^1_{i_1,i_2}(0^-) - G^1_{i_1,i_2}(0^+) = \delta_{i_1,i_2} \tag{B.20}$$

B.5 Matsubara frequencies

In order to to get a more convenient notation we exploit the KMS boundary conditions further. Since $G(\tau)$ is restricted to an interval of the size β it can be represented in terms of a Fourier series [57]

$$G^n_{i_1,\ldots,i_{2n}}(\tau_1,\ldots,\tau_{2n}) = \frac{1}{\beta^{2n}} \sum_{\{\nu_i\}} e^{i(-\nu_1\tau_1+\nu_2\tau_2-\cdots+\nu_{2n}\tau_{2n})} G^n_{i_1,\ldots,i_{2n}}(\nu_1,\ldots,\nu_{2n}). \tag{B.21}$$

The frequency representation $G^n_{i_1,\ldots,i_{2n}}(\nu_1,\ldots,\nu_{2n})$ therefore reproduces our original time dependent Green's function and the associated properties. Consequently we get this representation by performing the Fourier transform

$$G^n_{i_1,\ldots,i_{2n}}(\nu_1,\ldots,\nu_{2n}) = \int_0^\beta d\tau_1 \cdots \int_0^\beta d\tau_{2n}\; e^{i(\nu_1\tau_1-\nu_2\tau_2+\cdots-\nu_{2n}\tau_{2n})} G^n_{i_1,\ldots,i_{2n}}(\tau_1,\ldots,\tau_{2n}). \tag{B.22}$$

Due to the antiperiodicity[26] we get the so-called (fermionic) Matsubara frequencies of the form

$$\nu_i = \frac{(2n_i+1)\pi}{\beta}. \tag{B.23}$$

Alongside this definition one usually also defines the bosonic variant obtained via a periodic function

$$\omega_i = \frac{2n_i\pi}{\beta}. \tag{B.24}$$

[26] A general antiperiodic function fulfills the condition $-f(x) = f(x+np)$ with $n = 1,3,\ldots$ and the periodicity p. This property is created by the KMS boundaries with an explicit periodicity of $p = \beta$.

Appendix C Frequency notations

As shown in Appendix B.5 we are now able to represent a general two-particle Green's function in the more convenient frequency notation by performing a Fourier transform from the (imaginary) time space into the frequency space. This transformation reads

$$G_{ijkl}^{\nu_1\nu_2\nu_3\nu_4} = \int d\tau_1 d\tau_2 d\tau_3 d\tau_4 \;\; G_{ijkl}(\tau_1,\tau_2,\tau_3,\tau_4)\, e^{i\nu_1\tau_1} e^{-i\nu_2\tau_2} e^{i\nu_3\tau_3} e^{-i\nu_4\tau_4}. \tag{C.1}$$

Due to time translational symmetry not all times are independent from each other: We can translate the Green's function by τ_4 so that the last time argument is 0. Subsequent substitutions

$$\tau_i' = \tau_i - \tau_4 \qquad i = 1,2,3$$

and an integration over τ_4 gives[27]

$$\begin{aligned} G_{ijkl}^{\nu_1\nu_2\nu_3\nu_4} &= \int d\tau_1 d\tau_2 d\tau_3 d\tau_4 \;\; G_{ijkl}(\tau_1-\tau_4,\tau_2-\tau_4,\tau_3-\tau_4,0)\, e^{i\nu_1\tau_1} e^{-i\nu_2\tau_2} e^{i\nu_3\tau_3} e^{-i\nu_4\tau_4} \\ &= \int d\tau_1' d\tau_2' d\tau_3' d\tau_4 \;\; G_{ijkl}\left(\tau_1',\tau_2',\tau_3',0\right) e^{i\nu_1\tau_1'} e^{-i\nu_2\tau_2'} e^{i\nu_3\tau_3'} e^{i(\nu_1-\nu_2+\nu_3-\nu_4)\tau_4} \\ &= \underbrace{\int d\tau_1' d\tau_2' d\tau_3' \;\; G_{ijkl}\left(\tau_1',\tau_2',\tau_3',0\right) e^{i\nu_1\tau_1'} e^{-i\nu_2\tau_2'} e^{i\nu_3\tau_3'}}_{\equiv\; G_{ijkl}^{\nu_1\nu_2\nu_3}} \underbrace{\int d\tau_4 \;\; e^{i(\nu_1-\nu_2+\nu_3-\nu_4)\tau_4}}_{\beta\delta_{(\nu_1-\nu_2+\nu_3-\nu_4),0}}, \end{aligned} \tag{C.2}$$

which is just the conservation of energy

$$\nu_1 - \nu_2 + \nu_3 - \nu_4 = 0. \tag{C.3}$$

We now have two ways to classify these three frequencies: three independent fermionic frequencies or two fermionic together with one bosonic frequency. In recent literature one usually uses the latter which leads to the following ph, $\overline{\text{ph}}$ and pp notation, illustrated in Fig. C.1.

[27] The substitution also shift the integral interval from $[0,\beta]$ to $[-\tau_4,\beta-\tau_4]$. However, for fermions, both the prefactor $e^{i\nu_j\tau_j}$ and the Green's function itself is antiperiodic with respect to τ_j. This in turn means that the combined function is periodic and consequently that any integral of the length β is equal to the integral from 0 to β.

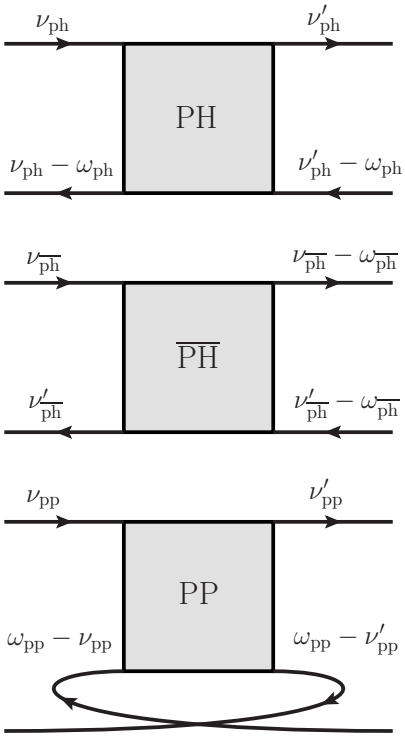

Figure C.1: The three different frequency notations: In the top panel the particle-hole (PH) notation, in the middle panel the particle-hole transversal ($\overline{\mathrm{PH}}$) notation and in the bottom panel the particle-particle (PP) notation. These notations naturally appear when considering the Bethe-Salpeter equations in the PH, $\overline{\mathrm{PH}}$ and PP channel. Of course a two-particle Green's function can be presented in all three frequency notations.

$$\nu_1 = \nu_{ph} \qquad = \nu_{\overline{ph}} \qquad = \nu_{pp} \tag{C.4}$$

$$\nu_2 = \nu_{ph} - \omega_{ph} = \nu'_{\overline{ph}} \qquad = \omega_{pp} - \nu'_{pp} \tag{C.5}$$

$$\nu_3 = \nu'_{ph} - \omega_{ph} = \nu'_{\overline{ph}} - \omega_{\overline{ph}} = \omega_{pp} - \nu_{pp} \tag{C.6}$$

$$\nu_4 = \nu'_{ph} \qquad = \nu_{\overline{ph}} - \omega_{\overline{ph}} = \nu'_{pp} \tag{C.7}$$

Appendix D Hamiltonian in AbinitioDΓA

We start by setting up a general two-particle Hamiltonian

$$\hat{H} = \hat{H}_0 + \hat{U}^{\text{full}}. \tag{D.1}$$

$\hat{H}_0$ contains all one-particle contributions and is e.g. calculated via DFT and represented in reciprocal (momentum) space. $\hat{U}^{\text{full}}$ on the other hand contains all two-particle interactions which we, at first, represent in real space.

$$\hat{H} = \sum_{\substack{\mathbf{k}\\ lm\\ \sigma}} \varepsilon_{\mathbf{k}lm} \hat{c}^\dagger_{\mathbf{k}l\sigma} \hat{c}_{\mathbf{k}m\sigma} + \frac{1}{2} \sum_{\substack{\mathbf{R}_1\mathbf{R}_2\mathbf{R}_3\mathbf{R}_4\\ ll'mm'\\ \sigma_1\sigma_2\sigma_3\sigma_4}} U^{\text{full}}_{lm'ml'}(\mathbf{R}_1, \mathbf{R}_2, \mathbf{R}_3, \mathbf{R}_4)\, \hat{c}^\dagger_{\mathbf{R}_3 m'\sigma_3} \hat{c}^\dagger_{\mathbf{R}_1 l\sigma_1} \hat{c}_{\mathbf{R}_2 m\sigma_2} \hat{c}_{\mathbf{R}_4 l'\sigma_4}. \tag{D.2}$$

For reasons which become later clear we will restrict ourselves to interactions which fulfill SU(2) symmetry. Part of this symmetry is the conservation of incoming and outgoing spins

$$\underbrace{\sigma_1 + \sigma_3}_{\text{S}_z \text{ of outgoing Particles}} = \underbrace{\sigma_2 + \sigma_4}_{\text{S}_z \text{ of incoming Particles}}. \tag{D.3}$$

This property simplifies the spin dependence of our interaction for which the relation

$$\begin{aligned} \hat{c}^\dagger_{\mathbf{R}_3 m'\sigma} \hat{c}^\dagger_{\mathbf{R}_1 l\sigma'} \hat{c}_{\mathbf{R}_2 m\sigma'} \hat{c}_{\mathbf{R}_4 l'\sigma} &= \hat{c}^\dagger_{\mathbf{R}_1 l\sigma'} \hat{c}^\dagger_{\mathbf{R}_3 m'\sigma} \hat{c}_{\mathbf{R}_4 l'\sigma} \hat{c}_{\mathbf{R}_2 m\sigma'} \\ \implies U^{\text{full}}_{lm'ml'}(\mathbf{R}_1, \mathbf{R}_2, \mathbf{R}_3, \mathbf{R}_4) &= U^{\text{full}}_{m'll'm}(\mathbf{R}_3, \mathbf{R}_4, \mathbf{R}_1, \mathbf{R}_2). \end{aligned} \tag{D.4}$$

applies, which is known as swapping symmetry (SW). By performing a general Fourier transform of the fermionic operators we can further simplify the full Hamiltonian.

$$\hat{c}^\dagger_{\mathbf{R}_3 m'\sigma} \hat{c}^\dagger_{\mathbf{R}_1 l\sigma'} \hat{c}_{\mathbf{R}_2 m\sigma'} \hat{c}_{\mathbf{R}_4 l'\sigma} = \sum_{\mathbf{k}_1,\mathbf{k}_2,\mathbf{k}_3,\mathbf{k}_4} e^{i\mathbf{k}_1\mathbf{R}_1} e^{-i\mathbf{k}_2\mathbf{R}_2} e^{i\mathbf{k}_3\mathbf{R}_3} e^{-i\mathbf{k}_4\mathbf{R}_4} \hat{c}^\dagger_{\mathbf{k}_3 m'\sigma} \hat{c}^\dagger_{\mathbf{k}_1 l\sigma'} \hat{c}_{\mathbf{k}_2 m\sigma'} \hat{c}_{\mathbf{k}_4 l'\sigma} \tag{D.5}$$

with

$$\begin{aligned} \sum_{\mathbf{R}} e^{i\mathbf{k}\mathbf{R}} \hat{c}_{\mathbf{R}l\sigma} &= \hat{c}_{\mathbf{k}l\sigma} & \sum_{\mathbf{R}} e^{-i\mathbf{k}\mathbf{R}} \hat{c}^\dagger_{\mathbf{R}l\sigma} &= \hat{c}^\dagger_{\mathbf{k}l\sigma} \\ \sum\!\!\!\!\!\!\int_{\mathbf{k}\in\text{BZ}} e^{-i\mathbf{k}\mathbf{R}} \hat{c}_{\mathbf{k}l\sigma} &= \hat{c}_{\mathbf{R}l\sigma} & \sum\!\!\!\!\!\!\int_{\mathbf{k}\in\text{BZ}} e^{i\mathbf{k}\mathbf{R}} \hat{c}^\dagger_{\mathbf{k}l\sigma} &= \hat{c}^\dagger_{\mathbf{R}l\sigma} \end{aligned} \tag{D.6}$$

Similar to Appendix C we are now able to exploit space translational invariance. By adopting the particle-hole equivalent notation for momenta

$$\begin{aligned} \mathbf{k}_1 &= \mathbf{k} \\ \mathbf{k}_2 &= \mathbf{k} - \mathbf{q} \\ \mathbf{k}_3 &= \mathbf{k}' - \mathbf{q} \\ \mathbf{k}_4 &= \mathbf{k}'. \end{aligned} \tag{D.7}$$

we can now rewrite the two-particle part of the Hamiltonian:

$$\begin{aligned}\hat{U}^{\text{full}} &= \frac{1}{2}\sum_{\substack{\mathbf{R}_1\mathbf{R}_2\mathbf{R}_3\\ ll'mm'\\ \sigma\sigma'}} U^{\text{full}}_{lm'ml'}\left(\mathbf{R}_1,\mathbf{R}_2,\mathbf{R}_3\right)\hat{c}^\dagger_{\mathbf{R}_3 m'\sigma}\hat{c}^\dagger_{\mathbf{R}_1 l\sigma'}\hat{c}_{\mathbf{R}_2 m\sigma'}\hat{c}_{\mathbf{0}l'\sigma}\\ &= \frac{1}{2}\sum_{\substack{\mathbf{qkk'}\\ ll'mm'\\ \sigma\sigma'}} U^{\mathbf{qkk'}}_{lm'ml'}\hat{c}^\dagger_{\mathbf{k'}-\mathbf{q},m'\sigma}\hat{c}^\dagger_{\mathbf{k}l\sigma'}\hat{c}_{\mathbf{k}-\mathbf{q},m\sigma'}\hat{c}_{\mathbf{k'}l'\sigma}\end{aligned} \tag{D.8}$$

with

$$U^{\mathbf{qkk'}}_{lm'ml'} = \sum_{\mathbf{R}_1,\mathbf{R}_2,\mathbf{R}_3} e^{i\mathbf{kR}_1}e^{-i(\mathbf{k}-\mathbf{q})\mathbf{R}_2}e^{i(\mathbf{k'}-\mathbf{q})\mathbf{R}_3}U^{\text{full}}_{lm'ml'}\left(\mathbf{R}_1,\mathbf{R}_2,\mathbf{R}_3\right). \tag{D.9}$$

The momentum dependencies of these objects can be further simplified if the overlap between adjacent unit cells is neglected [20]. The creation and annihilation operators can then be paired up at site $\mathbf{0}$ and $\mathbf{R}$ which motivates the definition

$$U_{lm'ml'} \equiv U^{\text{full}}_{lm'ml'}\left(\mathbf{0},\mathbf{0},\mathbf{0}\right) \tag{D.10}$$

and

$$V^{\mathbf{q}}_{lm'ml'} \equiv \sum_{\mathbf{R}\neq\mathbf{0}} e^{i\mathbf{Rq}}U^{\text{full}}_{lm'ml'}\left(\mathbf{R},\mathbf{R},\mathbf{0}\right), \tag{D.11}$$

which represent a purely local (U) and a purely non-local ($\sum_{\mathbf{q}} V^{\mathbf{q}} = 0$) interaction, respectively. Applying the previously mentioned space translational symmetry (momentum conservation) to Eq. (D.4) leaves us with

$$U^{\text{full}}_{lm'ml'}\left(\mathbf{R}_1,\mathbf{R}_2,\mathbf{R}_3\right) = U^{\text{full}}_{m'll'm}\left(\mathbf{R}_3-\mathbf{R}_2,-\mathbf{R}_2,\mathbf{R}_1-\mathbf{R}_2\right), \tag{D.12}$$

which can be used to apply crossing and swapping symmetry to these new U and $V^{\mathbf{q}}$ objects:

$$\begin{aligned}U_{lm'ml'} &= U^{\text{full}}_{lm'ml'}\left(\mathbf{0},\mathbf{0},\mathbf{0}\right)\\ &\overset{\text{CR}}{=} -U^{\text{full}}_{lm'l'm}\left(\mathbf{0},\mathbf{0},\mathbf{0}\right) = -U_{lm'l'm}\end{aligned} \tag{D.13}$$

$$\begin{aligned}U_{lm'ml'} &= U^{\text{full}}_{lm'ml'}\left(\mathbf{0},\mathbf{0},\mathbf{0}\right)\\ &\overset{\text{SW}}{=} U^{\text{full}}_{m'll'm}\left(\mathbf{0},\mathbf{0},\mathbf{0}\right) = U_{m'll'm}\end{aligned} \tag{D.14}$$

$$\begin{aligned}V^{\mathbf{q}}_{lm'ml'} &= \sum_{\mathbf{R}\neq\mathbf{0}} e^{i\mathbf{Rq}}U^{\text{full}}_{lm'ml'}\left(\mathbf{R},\mathbf{R},\mathbf{0}\right)\\ &\overset{\text{SW}}{=} \sum_{\mathbf{R}\neq\mathbf{0}} e^{i\mathbf{Rq}}U^{\text{full}}_{m'll'm}\left(-\mathbf{R},-\mathbf{R},\mathbf{0}\right)\\ &= \sum_{\mathbf{R}\neq\mathbf{0}} e^{-i\mathbf{Rq}}U^{\text{full}}_{m'll'm}\left(\mathbf{R},\mathbf{R},\mathbf{0}\right) = V^{-\mathbf{q}}_{m'll'm}\end{aligned} \tag{D.15}$$

Appendix E One- and two-particle Green's functions in AbinitioDΓA

In `AbinitioDΓA` we restrict ourselves to two kind of Green's functions, namely the one-particle and two-particle ones. The explicit application of time translational symmetry (energy conservation) allows one to write

$$G^{\mathbf{k}}_{\substack{lm \\ \sigma}}(\tau) \equiv -\left\langle \mathcal{T}\left[\hat{c}_{\mathbf{k}l\sigma}(\tau)\hat{c}^{\dagger}_{\mathbf{k}m\sigma}(0)\right]\right\rangle \tag{E.1}$$

$$G^{\mathbf{qkk'}}_{\substack{lmm'l' \\ \sigma_1\sigma_2\sigma_3\sigma_4}}(\tau_1,\tau_2,\tau_3) \equiv \left\langle \mathcal{T}\left[\hat{c}_{\mathbf{k}l\sigma_1}(\tau_1)\hat{c}^{\dagger}_{\mathbf{k}-\mathbf{q},m\sigma_2}(\tau_2)\hat{c}_{\mathbf{k'}-\mathbf{q},m'\sigma_3}(\tau_3)\hat{c}^{\dagger}_{\mathbf{k'}l'\sigma_4}(0)\right]\right\rangle. \tag{E.2}$$

The already mentioned assumed spin conservation allows us to have only six different spin combinations

$$\sigma_1\sigma_2\sigma_3\sigma_4 \;=\; \begin{cases} \uparrow\uparrow\uparrow\uparrow & \downarrow\downarrow\downarrow\downarrow \\ \uparrow\uparrow\downarrow\downarrow & \downarrow\downarrow\uparrow\uparrow \\ \uparrow\downarrow\downarrow\uparrow & \downarrow\uparrow\uparrow\downarrow \end{cases} \tag{E.3}$$

in the two-particle Green's function. This restriction in turn allows us to abbreviate the notation to

$$\begin{aligned} G_{\sigma\sigma'} &\equiv G_{\sigma\sigma\sigma'\sigma'} \\ G_{\overline{\sigma\sigma'}} &\equiv G_{\sigma\sigma'\sigma'\sigma} \end{aligned} \tag{E.4}$$

Applying a SU(2) transformation in form of a rotation about the y-axis with a rotation angle of $\varphi = \pi$ we get [55]

$$\begin{aligned} G_{\sigma\sigma'} &= G_{(-\sigma)(-\sigma')} = G_{\sigma'\sigma} \\ G_{\overline{\sigma\sigma'}} &= G_{\overline{(-\sigma)(-\sigma')}} = G_{\overline{\sigma'\sigma}}, \end{aligned} \tag{E.5}$$

while a rotation angle of $\varphi = \frac{\pi}{2}$ results in

$$G_{\sigma\sigma} = G_{\sigma(-\sigma)} + G_{\overline{\sigma(-\sigma)}}. \tag{E.6}$$

The SU(2) symmetry further allows us to decompose the Green's function into the so-called spin diagonalized representation [64]. Therewith the spin degrees of freedom in the Green's function (and later on also the vertices) can be separated into the so-called density and magnetic channels (in literature these are oftentimes referred to as charge and spin channels, respectively):

$$G_D \equiv G_{\uparrow\uparrow} + G_{\uparrow\downarrow} \tag{E.7}$$

$$G_M \equiv G_{\uparrow\uparrow} - G_{\uparrow\downarrow} \overset{\text{SU(2)}}{=} G_{\overline{\uparrow\downarrow}} \tag{E.8}$$

In our case this relation is numerically implemented as

$$G_D = \frac{1}{2}\left[G_{\uparrow\uparrow} + G_{\downarrow\downarrow} + G_{\uparrow\downarrow} + G_{\downarrow\uparrow}\right]$$

$$G_M = \frac{1}{4}\left[G_{\uparrow\uparrow} + G_{\downarrow\downarrow} - G_{\uparrow\downarrow} - G_{\downarrow\uparrow} + G_{\overline{\uparrow\downarrow}} + G_{\overline{\downarrow\uparrow}}\right].$$

The discontinuities contained in the two-particle Green's function (coming from equal time arguments of the disconnected terms shown in Appendix B.4) can be canceled if one subtracts the disconnected pairs. These pairs of one-particle Green's functions arise from the 0^{th} expansion order and can be separated by applying Wick's theorem

$$\begin{aligned}
G^0_{1234} &= \left\langle \mathcal{T}\left[\hat{c}_1(\tau_1)\hat{c}_2^\dagger(\tau_2)\hat{c}_3(\tau_3)\hat{c}_4^\dagger(\tau_4)\right]\right\rangle_0 \\
&= \left\langle \mathcal{T}\left[\hat{c}_1(\tau_1)\hat{c}_2^\dagger(\tau_2)\right]\right\rangle_0 \left\langle \mathcal{T}\left[\hat{c}_3(\tau_3)\hat{c}_4^\dagger(\tau_4)\right]\right\rangle_0 + \left\langle \mathcal{T}\left[\hat{c}_1(\tau_1)\hat{c}_4^\dagger(\tau_4)\right]\right\rangle_0 \left\langle \mathcal{T}\left[\hat{c}_2^\dagger(\tau_2)\hat{c}_3(\tau_3)\right]\right\rangle_0 \\
&= \left\langle \mathcal{T}\left[\hat{c}_1(\tau_1)\hat{c}_2^\dagger(\tau_2)\right]\right\rangle_0 \left\langle \mathcal{T}\left[\hat{c}_3(\tau_3)\hat{c}_4^\dagger(\tau_4)\right]\right\rangle_0 - \left\langle \mathcal{T}\left[\hat{c}_1(\tau_1)\hat{c}_4^\dagger(\tau_4)\right]\right\rangle_0 \left\langle \mathcal{T}\left[\hat{c}_3(\tau_3)\hat{c}_2^\dagger(\tau_2)\right]\right\rangle_0 \\
&= G^0_{12}G^0_{34} - G^0_{14}G^0_{32}.
\end{aligned} \tag{E.9}$$

By dressing these disconnected terms with self-energies and aggregating the rest into the so-called connected term we get

$$\begin{aligned}
G^{\mathbf{qkk'}}_{\substack{lmm'l' \\ \sigma\sigma'}}(\tau_1,\tau_2,\tau_3) = \delta_{\mathbf{q0}} G^{\mathbf{k}}_{\substack{lm \\ \sigma}}(\tau_1-\tau_2) G^{\mathbf{k'}}_{\substack{m'l' \\ \sigma'}}(\tau_3) \\
- \delta_{\mathbf{kk'}}\delta_{\sigma\sigma'} G^{\mathbf{k}}_{\substack{ll' \\ \sigma}}(\tau_1) G^{\mathbf{k'-q}}_{\substack{m'm \\ \sigma'}}(\tau_2-\tau_3) \\
+ G^{\mathbf{qkk'}\text{con}}_{\substack{lmm'l' \\ \sigma\sigma'}}(\tau_1,\tau_2,\tau_3).
\end{aligned} \tag{E.10}$$

We now can define the Fourier transform with respect to the imaginary time arguments τ_i by

$$G^{qkk'\text{con}}_{\substack{lmm'l' \\ \sigma\sigma'}} = \int_0^\beta \int_0^\beta \int_0^\beta d\tau_1 d\tau_2 d\tau_3 \; e^{i\nu\tau_1} e^{-i(\nu-\omega)\tau_2} e^{i(\nu'-\omega)\tau_3} G^{\mathbf{qkk'}\text{con}}_{\substack{lmm'l' \\ \sigma\sigma'}}(\tau_1,\tau_2,\tau_3), \tag{E.11}$$

where we absorbed the bosonic and fermionic frequencies ω, ν, ν' into the compound index $q = (\mathbf{q}, \omega), k = (\mathbf{k}, \nu), k' = (\mathbf{k}', \nu')$ respectively. The relation between the full vertex and the connected Green's function is shown in Figure E.1 and explicitly reads

$$G^{qkk'\text{con}}_{\substack{lmm'l' \\ \sigma\sigma'}} = \sum_{\substack{nhh'n' \\ k''k'''}} \chi^{qkk''}_{0,lmnh} F^{qk''k'''}_{\substack{hnn'h' \\ \sigma\sigma'}} \chi^{qk'''k'}_{0,h'n'm'l'} \tag{E.12}$$

where we used the bare susceptibility

$$\chi^{qkk'}_{0,lmm'l'} \equiv -\beta\delta_{kk'} G^k_{ll'} G^{k'-q}_{m'm}. \tag{E.13}$$

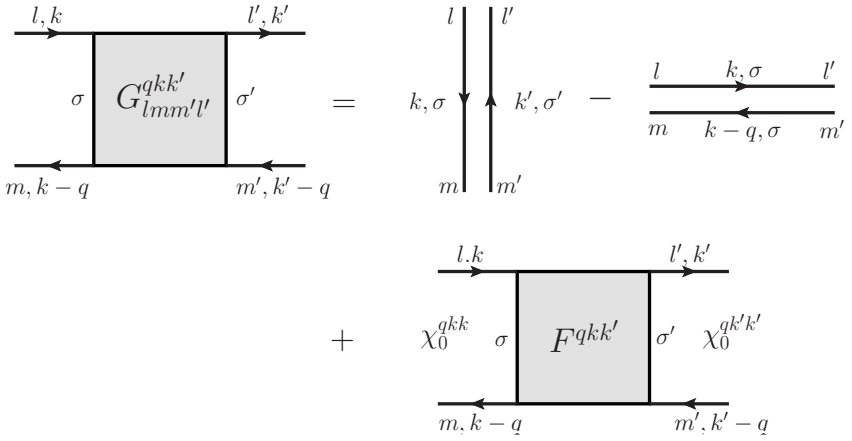

Figure E.1: Diagrammatic representation of the separation of the two-particle Green's function $G^{qkk'}_{\sigma\sigma',lmm'l'}$ into its disconnected and connected terms.

Most of the symmetries applied in the previous chapter can be similarly applied here: Time reversal symmetry leads, with the definition of $\overline{q} = (-\mathbf{q}, \omega)$ and similarly for $\overline{k}$ and $\overline{k'}$, to

$$G^{qkk'}_{\substack{lmm'l' \\ \sigma\sigma'}} \overset{\text{TR}}{=} G^{\overline{q}\overline{k'}\overline{k}}_{\substack{l'm'ml \\ \sigma'\sigma}}. \tag{E.14}$$

Crossing symmetry (CR) leads to

$$G^{qkk'}_{\substack{lmm'l' \\ \sigma\sigma'}} \overset{\text{CR}}{=} -G^{(k'-k)(k'-q)k'}_{\substack{m'mll' \\ \overline{\sigma'\sigma}}} \tag{E.15}$$

$$\overset{\text{CR}}{=} -G^{(k-k')k(k-q)}_{\substack{ll'm'm \\ \overline{\sigma\sigma'}}}, \tag{E.16}$$

while swapping symmetry (SW) leads to

$$G^{qkk'}_{\substack{lmm'l' \\ \sigma\sigma'}} \overset{\text{SW}}{=} G^{-q(k'-q)(k-q)}_{\substack{m'l'lm \\ \sigma'\sigma}}. \tag{E.17}$$

Please note here, that the same relations are also valid for the full vertex F.

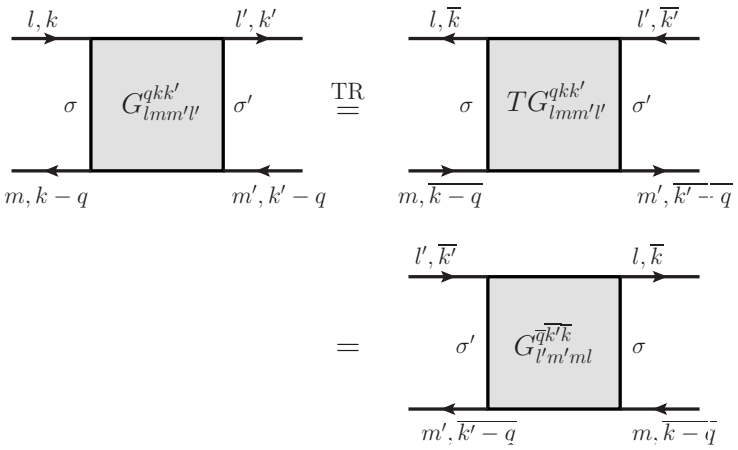

Figure E.2: Diagrammatic representation of the time-reversal symmetry applied to the two-particle Green's function $G^{qkk'}_{\sigma\sigma',lmm'l'}$. In the first step the time is reversed via the operator T and in the second step the operators are reordered to provide a valid two-particle Green's function according to (E.2).

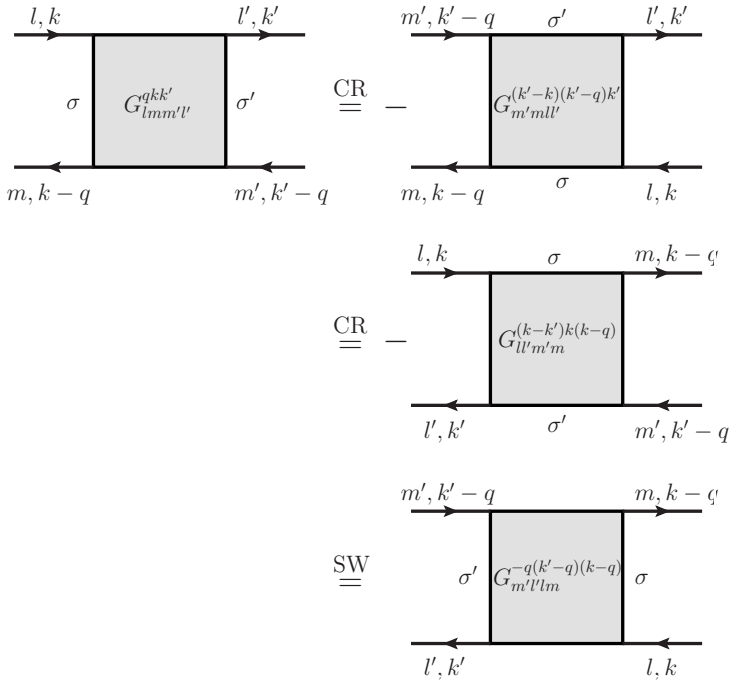

Figure E.3: Diagrammatic representation of the crossing and swapping symmetry applied to the two-particle Green's function $G^{qkk'}_{\sigma\sigma',lmm'l'}$.

Appendix F Diagrammatic extension in AbinitioDΓA

F.1 Dynamical vertex approximation

The full vertex F already mentioned in the context of connected Green's function can be classified into different subsets of diagrams. Λ represents the collection of fully two-particle irreducible diagrams, Φ_x represents diagrams which are *reducible* in channel x. Γ_x represents the counterpart to Φ_x and therefore represents diagrams which are *irreducible* in the given channel. All diagrams can either be reducible in exactly one channel or be completely irreducible.

$$\begin{aligned} F &= \Lambda + \Phi_{ph} + \Phi_{\overline{ph}} + \Phi_{pp} \\ &= \Gamma_{ph} + \Phi_{ph} \\ &= \Gamma_{\overline{ph}} + \Phi_{\overline{ph}} \\ &= \Gamma_{pp} + \Phi_{pp} \end{aligned} \tag{F.1}$$

The basic assumption of the DΓA approach is the locality of the fully irreducible vertex Λ [10], contrary to DMFT where the self-energy Σ is assumed to be local. That means that the assumption of locality is moved from the one-particle level to the two-particle level.

$$\Lambda^{qkk'} \rightarrow \Lambda^{\omega\nu\nu'} \tag{F.2}$$

One further simplification is introduced in the ladderDΓA approach employed in `AbinitioDΓA`, namely locality of the *particle-particle* reducible diagrams

$$\begin{aligned} \Lambda^{qkk'} &\rightarrow \Lambda^{\omega\nu\nu'} \\ \Phi_{\mathrm{pp}}^{qkk'} &\rightarrow \Phi_{\mathrm{pp}}^{\omega\nu\nu'} \end{aligned} \tag{F.3}$$

F.2 Local Bethe-Salpeter equation

The starting point of our derivation is the local full vertex F. F is directly contained in the full two-particle Green's function and according to the above mentioned classification we can explicitly write the local Bethe-Salpeter equations (BSE). In the spin diagonalized representation F explicitly reads

$$F^{\omega\nu\nu'}_{\substack{lmm'l'\\ r}} = \Gamma^{\omega\nu\nu'}_{\substack{lmm'l'\\ r}} + \Phi^{\omega\nu\nu'}_{\substack{lmm'l'\\ r}}. \tag{F.4}$$

The reducible diagrams can be constructed via the usual ladder

$$\Phi^{\omega\nu\nu'}_{\substack{lmm'l'\\ r}} = \sum_{\substack{nn'hh'\\ \nu''}} \Gamma^{\omega\nu\nu''}_{\substack{lmhn\\ r}} \chi^{\omega\nu''\nu''}_{0,nhh'n'} F^{\omega\nu''\nu'}_{\substack{n'h'm'l'\\ r}}. \tag{F.5}$$

The building block of ladderDΓA calculations is the irreducible vertex Γ. We can extract this vertex from a QMC measurement of χ and by using the ladder above:

$$\begin{aligned}
\chi^{\omega\nu\nu'}_{\substack{lmm'l'\\ r}} &= \chi^{\omega\nu\nu'}_{0,lmm'l'}\delta_{\nu\nu'} + \sum_{nhh'n'} \chi^{\omega\nu\nu}_{0,lmnh} F^{\omega\nu\nu'}_{\substack{hnn'h'\\ r}} \chi^{\omega\nu'\nu'}_{0,h'n'm'l'} \\
\chi^{\omega\nu\nu'}_{\substack{lmm'l'\\ r}} &= \chi^{\omega\nu\nu'}_{0,lmm'l'}\delta_{\nu\nu'} + \sum_{nhh'n'} \chi^{\omega\nu\nu}_{0,lmnh} \Gamma^{\omega\nu\nu'}_{\substack{hnn'h'\\ r}} \chi^{\omega\nu'\nu'}_{0,h'n'm'l'} \\
&\quad + \sum_{\substack{nhh'n',t's'st\\ \nu''}} \chi^{\omega\nu\nu}_{0,lmnh} \Gamma^{\omega\nu\nu''}_{\substack{hnn'h'\\ r}} \chi^{\omega\nu''\nu''}_{0,h'n's't'} \Gamma^{\omega\nu''\nu'}_{\substack{t's'st\\ r}} \chi^{\omega\nu'\nu'}_{0,tsm'l'} + \dots \\
\chi^{\omega\nu\nu'}_{\substack{lmm'l'\\ r}} &= \chi^{\omega\nu\nu'}_{0,lmm'l'}\delta_{\nu\nu'} + \sum_{nhh'n'} \chi^{\omega\nu\nu}_{0,lmnh} \Gamma^{\omega\nu\nu''}_{\substack{hnn'h'\\ r}} \chi^{\omega\nu''\nu'}_{\substack{h'n'm'l'\\ r}}
\end{aligned} \tag{F.6}$$

Due to the spin diagonalization ($r \in (D, M)$) the bare susceptibility only exists for the spin combination $\sigma\sigma\sigma\sigma$ and is therefore independent of the channel (hence we do not have any subscripts). The crossing and swapping symmetry behaves somewhat different if applied to either the irreducible or reducible parts of F. By applying crossing symmetry to a particle-hole reducible diagram one gets a particle-hole transversal reducible diagram (and the other way around). Because of this we have to be careful about our subscripts. Crossing symmetry (CR) leads to

$$\Phi^{\omega\nu\nu'}_{\substack{\overline{ph},lmm'l'\\ \sigma\sigma'}} \overset{\text{CR}}{=} -\Phi^{(\nu'-\nu)(\nu'-\omega)\nu'}_{\substack{ph,m'mll'\\ \overline{\sigma'\sigma}}} \tag{F.7a}$$

$$\overset{\text{CR}}{=} -\Phi^{(\nu-\nu')\nu(\nu-\omega)}_{\substack{ph,ll'm'm\\ \overline{\sigma\sigma'}}}, \tag{F.7b}$$

while swapping symmetry retains the diagram type

$$\Phi^{\omega\nu\nu'}_{\substack{ph,lmm'l'\\ \sigma\sigma'}} \overset{\text{SW}}{=} \Phi^{(-\omega)(\nu'-\omega)(\nu-\omega)}_{\substack{ph,m'l'lm\\ \sigma'\sigma}}. \tag{F.8}$$

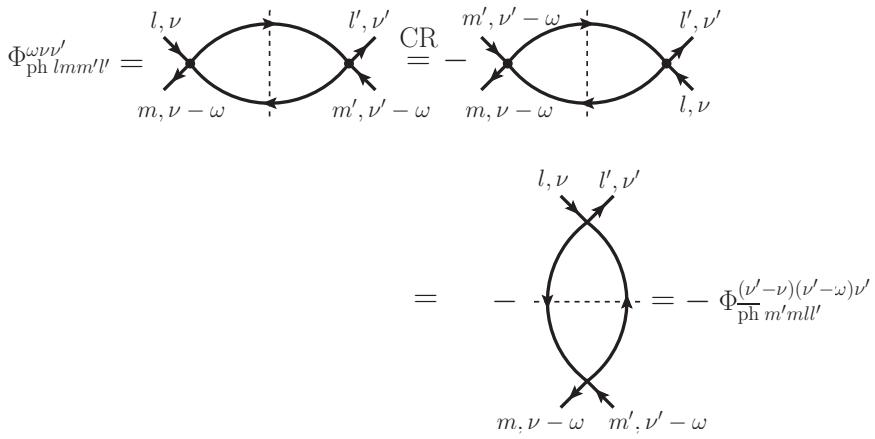

Figure F.1: Diagrammatic representation of change from a particle-hole reducible diagram to a particle-hole transversal reducible diagram. This exemplary diagram represents Equation (F.7a).

With these relations we can derive the crossing symmetry for the density and the magnetic channel (we will need these relations later on):

$$\begin{aligned}
\Phi^{\omega\nu\nu'}_{\substack{\overline{lmm'l'}\\ \overline{ph},D}} &= \Phi^{\omega\nu\nu'}_{\substack{\overline{lmm'l'}\\ \overline{ph},\uparrow\uparrow}} + \Phi^{\omega\nu\nu'}_{\substack{\overline{lmm'l'}\\ \overline{ph},\uparrow\downarrow}} \\
&\overset{\text{CR}}{=} -\Phi^{(\nu'-\nu)(\nu'-\omega)\nu'}_{\substack{m'\overline{mll'}\\ ph,\overline{\uparrow\uparrow}}} - \Phi^{(\nu'-\nu)(\nu'-\omega)\nu'}_{\substack{m'\overline{mll'}\\ ph,\overline{\downarrow\uparrow}}} \\
&\overset{\text{SU(2)}}{=} -\Phi^{(\nu'-\nu)(\nu'-\omega)\nu'}_{\substack{m'\overline{mll'}\\ ph,\uparrow\uparrow}} - \Phi^{(\nu'-\nu)(\nu'-\omega)\nu'}_{\substack{m'\overline{mll'}\\ ph,\downarrow\downarrow}} + \Phi^{(\nu'-\nu)(\nu'-\omega)\nu'}_{\substack{m'\overline{mll'}\\ ph,\downarrow\uparrow}} \\
&= \frac{1}{2}\left(-\Phi^{(\nu'-\nu)(\nu'-\omega)\nu'}_{\substack{m'\overline{mll'}\\ ph,\uparrow\uparrow}} - \Phi^{(\nu'-\nu)(\nu'-\omega)\nu'}_{\substack{m'\overline{mll'}\\ ph,\uparrow\downarrow}}\right) + \frac{3}{2}\left(-\Phi^{(\nu'-\nu)(\nu'-\omega)\nu'}_{\substack{m'\overline{mll'}\\ ph,\uparrow\uparrow}} + \Phi^{(\nu'-\nu)(\nu'-\omega)\nu'}_{\substack{m'\overline{mll'}\\ ph,\uparrow\downarrow}}\right) \\
&= -\frac{1}{2}\Phi^{(\nu'-\nu)(\nu'-\omega)\nu'}_{\substack{m'\overline{mll'}\\ D}} - \frac{3}{2}\Phi^{(\nu'-\nu)(\nu'-\omega)\nu'}_{\substack{m'\overline{mll'}\\ M}}
\end{aligned} \tag{F.9a}$$

$$\begin{aligned}
\Phi^{\omega\nu\nu'}_{\substack{\overline{lmm'l'}\\ \overline{ph},M}} &= \Phi^{\omega\nu\nu'}_{\substack{\overline{lmm'l'}\\ \overline{ph},\uparrow\uparrow}} - \Phi^{\omega\nu\nu'}_{\substack{\overline{lmm'l'}\\ \overline{ph},\uparrow\downarrow}} \\
&\overset{\text{CR}}{=} -\Phi^{(\nu'-\nu)(\nu'-\omega)\nu'}_{\substack{m'\overline{mll'}\\ ph,\overline{\uparrow\uparrow}}} + \Phi^{(\nu'-\nu)(\nu'-\omega)\nu'}_{\substack{m'\overline{mll'}\\ ph,\overline{\downarrow\uparrow}}} \\
&\overset{\text{SU(2)}}{=} -\Phi^{(\nu'-\nu)(\nu'-\omega)\nu'}_{\substack{m'\overline{mll'}\\ ph,\uparrow\uparrow}} + \Phi^{(\nu'-\nu)(\nu'-\omega)\nu'}_{\substack{m'\overline{mll'}\\ ph,\downarrow\downarrow}} - \Phi^{(\nu'-\nu)(\nu'-\omega)\nu'}_{\substack{m'\overline{mll'}\\ ph,\downarrow\uparrow}} \\
&= \frac{1}{2}\left(-\Phi^{(\nu'-\nu)(\nu'-\omega)\nu'}_{\substack{m'\overline{mll'}\\ ph,\uparrow\uparrow}} - \Phi^{(\nu'-\nu)(\nu'-\omega)\nu'}_{\substack{m'\overline{mll'}\\ ph,\uparrow\downarrow}}\right) + \frac{1}{2}\left(\Phi^{(\nu'-\nu)(\nu'-\omega)\nu'}_{\substack{m'\overline{mll'}\\ ph,\uparrow\uparrow}} - \Phi^{(\nu'-\nu)(\nu'-\omega)\nu'}_{\substack{m'\overline{mll'}\\ ph,\uparrow\downarrow}}\right) \\
&= -\frac{1}{2}\Phi^{(\nu'-\nu)(\nu'-\omega)\nu'}_{\substack{m'\overline{mll'}\\ D}} + \frac{1}{2}\Phi^{(\nu'-\nu)(\nu'-\omega)\nu'}_{\substack{m'\overline{mll'}\\ M}}
\end{aligned} \tag{F.9b}$$

F.3 Non-local Bethe-Salpeter equation

Once the irreducible vertex is extracted from the QMC data we can build the ladders with non-local propagators χ_0. However before doing that we supplement this vertex with the non-local interaction $\mathbf{V}^{\mathbf{qkk'}}$. The rationale behind this is that Γ is to lowest order equal to the local interaction U. Since we assume frequency independent interactions only we can write[28]

$$\Gamma^{qkk'}_{\substack{lmm'l' \\ \sigma\sigma'}} \equiv \Gamma^{\omega\nu\nu'}_{\substack{lmm'l' \\ \sigma\sigma'}} + \mathbf{V}^{\mathbf{qkk'}}_{\substack{lmm'l' \\ \sigma\sigma'}} \tag{F.10}$$

$$\mathbf{V}^{\mathbf{qkk'}}_{\substack{lmm'l' \\ \sigma\sigma'}} \equiv \beta^{-2}\left[V^{\mathbf{q}}_{lm'ml'} - \delta_{\sigma\sigma'} V^{\mathbf{k'-k}}_{m'lml'}\right]. \tag{F.11}$$

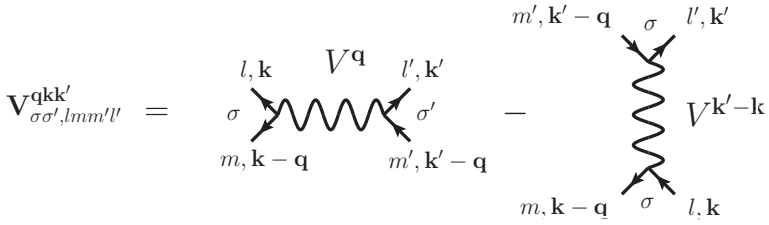

Figure F.2: Diagrammatic representation of the interaction vertex $V^{\mathbf{qkk'}}_{lm'ml'}$.

A considerable simplification can be achieved by neglecting the term depending on $\mathbf{k'} - \mathbf{k}$. By doing that we get

$$\begin{aligned}\Gamma^{qvv'}_{\substack{lmm'l' \\ r}} &= \Gamma^{\omega\nu\nu'}_{\substack{lmm'l' \\ r}} + \mathbf{V}^{\mathbf{q}}_{\substack{lmm'l' \\ r}} \\ &= \Gamma^{\omega\nu\nu'}_{\substack{lmm'l' \\ r}} + \delta_{r,d} 2\beta^{-2} V^{\mathbf{q}}_{lm'ml'},\end{aligned} \tag{F.12}$$

and the non-local BSE reads

$$F^{qkk'}_{\substack{lmm'l' \\ r}} = \Gamma^{qvv'}_{\substack{lmm'l' \\ r}} + \sum_{\substack{nn'hh' \\ k''}} \Gamma^{qvv''}_{\substack{lmhn \\ r}} \chi^{qk''k''}_{0,nhh'n'} F^{qk''k'}_{\substack{n'h'm'l' \\ r}}. \tag{F.13}$$

Since F is now built from $\mathbf{k}$ and $\mathbf{k'}$ independent objects, F is naturally also independent from

[28] Please note the difference in index subsets between the interaction vertex and the interaction itself. The vertex has to have the same index order as the irreducible vertex (i.e. $\hat{c}_{\mathbf{k}l\sigma}\hat{c}^{\dagger}_{\mathbf{k}-\mathbf{q},m\sigma}\hat{c}_{\mathbf{k'}-\mathbf{q},m'\sigma'}\hat{c}^{\dagger}_{\mathbf{k'}l'\sigma'}$), while the interaction must have a general two-particle interaction order. Additionally we have to interpret the interaction as Feynman diagram, thus the roles of the annihilation and creation operators have to be reversed. With this in mind we can swap the operators order to $\hat{c}^{\dagger}_{\mathbf{k'}-\mathbf{q},m'\sigma'}\hat{c}^{\dagger}_{\mathbf{k}l\sigma}\hat{c}_{\mathbf{k}-\mathbf{q},m\sigma}\hat{c}_{\mathbf{k'}l'\sigma'}$ which corresponds to the interaction $V^{\mathbf{q}}_{lm'ml'}$. The second interaction term on the other hand is generated from the first one via crossing symmetry.

these and we can therefore perform the $\mathbf{k}$-sum explicitly. This yields (with $F^{qvv'} = \sum_{\mathbf{kk}'} F^{qkk'}$)

$$\begin{aligned} F^{qvv'}_{\substack{lmm'l' \\ r}} &= \Gamma^{qvv'}_{\substack{lmm'l' \\ r}} + \sum_{\substack{nn'hh' \\ \nu''}} \Gamma^{qvv''}_{\substack{lmhn \\ r}} \chi^{qv''v''}_{0,nhh'n'} F^{qv''v'}_{\substack{n'h'm'l' \\ r}} \\ &= \Gamma^{qvv'}_{\substack{lmm'l' \\ r}} + \Phi^{qvv'}_{\substack{lmm'l' \\ r}} \end{aligned} \tag{F.14}$$

with

$$\chi^{qvv}_{0,lmm'l'} = \sum_{\mathbf{k}} \chi^{qkk}_{0,lmm'l'}. \tag{F.15}$$

The ladder is only built up in the particle-hole channel and as already mentioned we hence do not recover a crossing symmetric non-local vertex $F^{qvv'}$. We can however restore this symmetry by taking the corresponding diagrams in the particle-hole transversal channel into account as well. In order to do this we have to set up the parquet equation and use the crossing symmetric properties shown previously. (Here we only derive the formulas for the density channel. The formulation in the magnetic channel is not necessary since it will not appear in any future derivation.)

$$\begin{aligned} F^{qkk'}_{D} &= \Lambda^{\omega vv'}_{D} + \Phi^{\omega vv'}_{D,pp} + \Phi^{qvv'}_{D,ph} + \Phi^{qkk'}_{D,\overline{ph}} + \mathbf{V}^{\mathbf{qkk'}}_{D} \\ &= \Lambda^{\omega vv'}_{D} + \Phi^{\omega vv'}_{D,pp} + \Phi^{\omega vv'}_{D,ph} + \Phi^{\omega vv'}_{D,\overline{ph}} + \left(\Phi^{qvv'}_{D,ph} - \Phi^{\omega vv'}_{D,ph}\right) + \left(\Phi^{qkk'}_{D,\overline{ph}} - \Phi^{\omega vv'}_{D,\overline{ph}}\right) + \mathbf{V}^{\mathbf{qkk'}}_{D} \\ &= F^{\omega vv'}_{D} + \left(\Phi^{qvv'}_{D,ph} - \Phi^{\omega vv'}_{D,ph}\right) + \left(\Phi^{qkk'}_{D,\overline{ph}} - \Phi^{\omega vv'}_{D,\overline{ph}}\right) + \mathbf{V}^{\mathbf{qkk'}}_{D} \end{aligned} \tag{F.16}$$

To be concise we drop the orbital indices (which are $lmm'l'$ for each term). We use the ladderDΓA approximation and assume Λ and Φ_{pp} to be purely local. This means that in Eq. (F.16) Λ and Φ_{pp} are purely local and $\Phi^{qvv'}_{D,ph}$ and $\Phi^{qkk'}_{D,\overline{ph}}$ are calculated from local Bethe-Salpeter ladders with a local vertex Γ as discussed in the following. Since the non-local interaction $\mathbf{V}^{\mathbf{qkk'}}$ is neither part of Φ_{ph} nor $\Phi_{\overline{ph}}$ nor $F^{\omega vv'}$ it has to be added explicitly and we have to ensure that it is crossing symmetric on its own.

$$\begin{aligned} \mathbf{V}^{\mathbf{qkk'}}_{\substack{lmm'l' \\ \sigma\sigma'}} &= \beta^{-2}\left(V^{\mathbf{q}}_{lm'ml'} - \delta_{\sigma\sigma'} V^{\mathbf{k'-k}}_{m'lml'}\right) \\ &\overset{\mathrm{CR}}{=} \beta^{-2}\left(-V^{\mathbf{k'-k}}_{m'lml'}\delta_{\sigma\sigma'} + V^{\mathbf{q}}_{lm'ml'}\right) \end{aligned} \tag{F.17}$$

In the density channel we get

$$\begin{aligned} \mathbf{V}^{\mathbf{qkk'}}_{\substack{lmm'l' \\ D}} &= \mathbf{V}^{\mathbf{qkk'}}_{\substack{lmm'l' \\ \uparrow\uparrow}} + \mathbf{V}^{\mathbf{qkk'}}_{\substack{lmm'l' \\ \uparrow\downarrow}} \\ &= 2\beta^{-2} V^{\mathbf{q}}_{lm'ml'} - \beta^{-2} V^{\mathbf{k'-k}}_{m'lml'}. \end{aligned} \tag{F.18}$$

With the help of

$$F^{qvv',\mathrm{nl}}_{\substack{lmm'l' \\ r}} \equiv F^{qvv'}_{\substack{lmm'l' \\ r}} - F^{\omega vv'}_{\substack{lmm'l' \\ r}} \tag{F.19}$$

and the non-local version of the crossing symmetric relations

$$\Phi^{qkk'}_{\substack{lmm'l' \\ \overline{ph},D}} = -\frac{1}{2}\Phi^{(k'-k)(k'-q)k'}_{\substack{m'mll' \\ D}} - \frac{3}{2}\Phi^{(k'-k)(k'-q)k'}_{\substack{m'mll' \\ M}} \tag{F.20a}$$

$$\Phi^{qkk'}_{\substack{lmm'l' \\ \overline{ph},M}} = -\frac{1}{2}\Phi^{(k'-k)(k'-q)k'}_{\substack{m'mll' \\ D}} + \frac{1}{2}\Phi^{(k'-k)(k'-q)k'}_{\substack{m'mll' \\ M}}, \tag{F.20b}$$

we get

$$\begin{aligned}\Phi^{q\nu\nu'}_{\substack{lmm'l' \\ D,ph}} - \Phi^{\omega\nu\nu'}_{\substack{lmm'l' \\ D,ph}} &= \left(F^{q\nu\nu'}_{\substack{lmm'l' \\ D,ph}} - \Gamma^{q\nu\nu'}_{\substack{lmm'l' \\ D,ph}}\right) - \left(F^{\omega\nu\nu'}_{\substack{lmm'l' \\ D,ph}} - \Gamma^{\omega\nu\nu'}_{\substack{lmm'l' \\ D,ph}}\right) \\ &= F^{q\nu\nu',\mathrm{nl}}_{\substack{lmm'l' \\ D,ph}} - 2\beta^{-2}V^{\mathbf{q}}_{lm'ml'},\end{aligned} \tag{F.21}$$

and

$$\begin{aligned}\Phi^{qkk'}_{\substack{lmm'l' \\ D,\overline{ph}}} - \Phi^{\omega\nu\nu'}_{\substack{lmm'l' \\ D,\overline{ph}}} &= -\frac{1}{2}\Phi^{(k'-k)(k'-q)k'}_{\substack{m'mll' \\ D,\mathrm{ph}}} - \frac{3}{2}\Phi^{(k'-k)(k'-q)k'}_{\substack{m'mll' \\ M,\mathrm{ph}}} + \frac{1}{2}\Phi^{(\nu'-\nu)(\nu'-\omega)\nu'}_{\substack{m'mll' \\ D,\mathrm{ph}}} + \frac{3}{2}\Phi^{(\nu'-\nu)(\nu'-\omega)\nu'}_{\substack{m'mll' \\ M,\mathrm{ph}}} \\ &= -\frac{1}{2}\left(F^{(k'-k)(k'-q)k'}_{\substack{m'mll' \\ D,\mathrm{ph}}} - \Gamma^{(k'-k)(k'-q)k'}_{\substack{m'mll' \\ D,\mathrm{ph}}}\right) - \frac{3}{2}\left(F^{(k'-k)(k'-q)k'}_{\substack{m'mll' \\ M,\mathrm{ph}}} - \Gamma^{(k'-k)(k'-q)k'}_{\substack{m'mll' \\ M,\mathrm{ph}}}\right) \\ &\quad + \frac{1}{2}\left(F^{(\nu'-\nu)(\nu'-\omega)\nu'}_{\substack{m'mll' \\ D,\mathrm{ph}}} - \Gamma^{(\nu'-\nu)(\nu'-\omega)\nu'}_{\substack{m'mll' \\ D,\mathrm{ph}}}\right) + \frac{3}{2}\left(F^{(\nu'-\nu)(\nu'-\omega)\nu'}_{\substack{m'mll' \\ M,\mathrm{ph}}} - \Gamma^{(\nu'-\nu)(\nu'-\omega)\nu'}_{\substack{m'mll' \\ M,\mathrm{ph}}}\right) \\ &= -\frac{1}{2}F^{(k'-k)(\nu'-\omega)\nu',\mathrm{nl}}_{\substack{m'mll' \\ D,\mathrm{ph}}} - \frac{3}{2}F^{(k'-k)(\nu'-\omega)\nu',\mathrm{nl}}_{\substack{m'mll' \\ M,\mathrm{ph}}} + \beta^{-2}V^{\mathbf{k}'-\mathbf{k}}_{m'lml'}.\end{aligned} \tag{F.22}$$

With these two expressions we see that the non-local interaction vertex cancels out and we finally get the fully crossing symmetric non-local full vertex

$$F^{qkk'}_{\substack{lmm'l' \\ D}} = F^{\omega\nu\nu'}_{\substack{lmm'l' \\ D}} + \underbrace{F^{q\nu\nu',\mathrm{nl}}_{\substack{lmm'l' \\ D,ph}} - \frac{1}{2}F^{(k'-k)(\nu'-\omega)\nu',\mathrm{nl}}_{\substack{m'mll' \\ D,\mathrm{ph}}} - \frac{3}{2}F^{(k'-k)(\nu'-\omega)\nu',\mathrm{nl}}_{\substack{m'mll' \\ M,\mathrm{ph}}}}_{\text{built with non-local ph ladder}}, \tag{F.23}$$

taking into account both the ph and $\overline{\mathrm{ph}}$ ladder. As a final and very important step we have to make sure when inverting and building the local and non-local ladders that we avoid the local irreducible vertex Γ. This is necessary because it recently was shown that this quantity contains an infinite set of diverging components [83]. The non-local ladder is built via

$$\begin{aligned}F^q_r &= \Gamma^q_r + \Phi^q_r \\ &= \Gamma^q_r + \Gamma^q_r\chi^q_0F^q_r \\ &= \left(1 - \Gamma^q_r\chi^q_0\right)^{-1}\Gamma^q_r \\ &= \left[\left(\Gamma^q_r\right)^{-1}\left(1 - \Gamma^q_r\chi^q_0\right)\right]^{-1} \\ &= \left[\left(\Gamma^q_r\right)^{-1} - \chi^q_0\right]^{-1}.\end{aligned} \tag{F.24}$$

Instead of supplying the non-local irreducible vertex Γ_r^q directly we have to perform some algebraic tricks instead:

$$\begin{aligned}
F_M^q &= \left[\left(\Gamma_M^q\right)^{-1} - \chi_0^q\right]^{-1} \\
&= \left[\left(\Gamma_M^\omega\right)^{-1} - \chi_0^q\right]^{-1} \\
&= \left[\left(F_M^\omega\left(1 + \chi_0^\omega F_M^\omega\right)^{-1}\right)^{-1} - \chi_0^q\right]^{-1} \\
&= \left[\left(1 + \chi_0^\omega F_M^\omega\right)\left(F_M^\omega\right)^{-1} - \chi_0^q\right]^{-1} \\
&= \left[\left(F_M^\omega\right)^{-1} + \chi_0^\omega - \chi_0^q\right]^{-1} \\
&= \left[\left(F_M^\omega\right)^{-1} - \chi_0^{q,\mathrm{nl}}\right]^{-1} \\
&= \left[\left(1 - \chi_0^{q,\mathrm{nl}} F_M^\omega\right)\left(F_M^\omega\right)^{-1}\right]^{-1} \\
&= F_M^\omega\left[1 - \chi_0^{q,\mathrm{nl}} F_M^\omega\right]^{-1}
\end{aligned} \tag{F.25a}$$

$$\begin{aligned}
F_D^q &= \left[\left(\Gamma_D^q\right)^{-1} - \chi_0^q\right]^{-1} \\
&= \left[\left(\Gamma_D^\omega + 2\beta^{-2}V^{\mathbf{q}}\right)^{-1} - \chi_0^q\right]^{-1} \\
&= \left\{\left[F_D^\omega\left(1 + \chi_0^\omega F_D^\omega\right)^{-1} + 2\beta^{-2}V^{\mathbf{q}}\right]^{-1} - \chi_0^q\right\}^{-1} \\
&= \left(\left\{\left[F_D^\omega + 2\beta^{-2}V^{\mathbf{q}}\left(1 + \chi_0^\omega F_D^\omega\right)\right]\left[1 + \chi_0^\omega F_D^\omega\right]\right\}^{-1} - \chi_0^q\right)^{-1} \\
&= \left\{\left[1 + \chi_0^\omega F_D^\omega\right]\left[F_D^\omega + 2\beta^{-2}V^{\mathbf{q}}\left(1 + \chi_0^\omega F_D^\omega\right)\right]^{-1} - \chi_0^q\right\}^{-1} \\
&= \left(\left\{1 + \chi_0^\omega F_D^\omega - \chi_0^q\left[F_D^\omega + 2\beta^{-2}V^{\mathbf{q}}\left(1 + \chi_0^\omega F_D^\omega\right)\right]\right\}\left\{F_D^\omega + 2\beta^{-2}V^{\mathbf{q}}\left[1 + \chi_0^\omega F_D^\omega\right]\right\}^{-1}\right)^{-1} \\
&= \left[F_D^\omega + 2\beta^{-2}V^{\mathbf{q}}\left(1 + \chi_0^\omega F_D^\omega\right)\right]\left[1 - \chi^{q,\mathrm{nl}} F_D^\omega - 2\beta^{-2}\chi_0^q V^{\mathbf{q}}\left(1 + \chi_0^\omega F_D^\omega\right)\right]^{-1}
\end{aligned} \tag{F.25b}$$

where we used the definition

$$\chi_0^{q,\mathrm{nl}} \equiv \chi_0^q - \chi_0^\omega, \tag{F.26}$$

and again dropped all fermionic frequencies and orbital indices to be more concise. By combining the extraction of the local irreducible vertex and the construction of the non-local full vertex we were able to completely avoid the previously mentioned problems. Furthermore we were able to reformulate the final expression so only one inversion is required. This massively improves the numerical implementation since matrix inversions represent the bottleneck of this algorithm.

Appendix G Equation of motion in AbinitioDΓA

G.1 Non-interacting Green's function

The `AbinitioDΓA` self-energy is derived via the equation of motion (EOM). The result is commonly known as Schwinger-Dyson equation and is based on the derivative of the Green's function with respect to the first imaginary time argument τ. This procedure explicitly reads:

$$\begin{aligned}
\frac{d}{d\tau} G^{k}_{\substack{mm' \\ \sigma}}(\tau) &= -\frac{d}{d\tau}\left\langle \mathcal{T}\left[\hat{c}_{\mathbf{k}m\sigma}(\tau)\hat{c}^{\dagger}_{\mathbf{k}m'\sigma}(0)\right]\right\rangle \\
&= -\frac{d}{d\tau}\left[\Theta(\tau)\left\langle \hat{c}_{\mathbf{k}m\sigma}(\tau)\hat{c}^{\dagger}_{\mathbf{k}m'\sigma}(0)\right\rangle - \Theta(-\tau)\left\langle \hat{c}^{\dagger}_{\mathbf{k}m'\sigma}(0)\hat{c}_{\mathbf{k}m\sigma}(\tau)\right\rangle\right] \\
&= -\delta(\tau)\left\langle \hat{c}_{\mathbf{k}m\sigma}(\tau)\hat{c}^{\dagger}_{\mathbf{k}m'\sigma}(0)\right\rangle - \Theta(\tau)\left\langle \left[\hat{H}, \hat{c}_{\mathbf{k}m\sigma}(\tau)\right]\hat{c}^{\dagger}_{\mathbf{k}m'\sigma}(0)\right\rangle \\
&\quad - \delta(\tau)\left\langle \hat{c}^{\dagger}_{\mathbf{k}m'\sigma}(0)\hat{c}_{\mathbf{k}m\sigma}(\tau)\right\rangle + \Theta(-\tau)\left\langle \hat{c}^{\dagger}_{\mathbf{k}m'\sigma}(0)\left[\hat{H}, \hat{c}_{\mathbf{k}m\sigma}(\tau)\right]\right\rangle \\
&= -\delta(\tau)\delta_{mm'} - \left\langle \mathcal{T}\left[\left[\hat{H}, \hat{c}_{\mathbf{k}m\sigma}(\tau)\right]\hat{c}^{\dagger}_{\mathbf{k}m'\sigma}(0)\right]\right\rangle \\
&= -\delta(\tau)\delta_{mm'} - \left\langle \mathcal{T}\left[\left[\hat{H}_0, \hat{c}_{\mathbf{k}m\sigma}(\tau)\right]\hat{c}^{\dagger}_{\mathbf{k}m'\sigma}(0)\right]\right\rangle - \underbrace{\left\langle \mathcal{T}\left[\left[\hat{U}^{full}, \hat{c}_{\mathbf{k}m\sigma}(\tau)\right]\hat{c}^{\dagger}_{\mathbf{k}m'\sigma}(0)\right]\right\rangle}_{[\Sigma G]^{\mathbf{k}}_{\substack{mm' \\ \sigma}}}
\end{aligned} \tag{G.1}$$

With the general (anti-)commutator rules

$$[AB, C] = A\,[B, C] + [A, C]\,B \tag{G.2a}$$

$$= A\,\{B, C\} - \{A, C\}\,B, \tag{G.2b}$$

we obtain the two emerging commutator expressions

$$\begin{aligned}
\left[\hat{c}^{\dagger}_1\hat{c}_2, \hat{c}_3\right] &= \hat{c}^{\dagger}_1\left\{\hat{c}_2, \hat{c}_3\right\} - \left\{\hat{c}^{\dagger}_1, \hat{c}_3\right\}\hat{c}_2 \\
&= -\delta_{1,3}\hat{c}_2
\end{aligned} \tag{G.3}$$

and

$$\begin{aligned}
\left[\hat{c}^{\dagger}_1\hat{c}^{\dagger}_2\hat{c}_3\hat{c}_4, \hat{c}_5\right] &= -\left\{\hat{c}_5, \hat{c}^{\dagger}_1\right\}\hat{c}^{\dagger}_2\hat{c}_3\hat{c}_4 + \hat{c}^{\dagger}_1\left\{\hat{c}_5, \hat{c}^{\dagger}_2\right\}\hat{c}_3\hat{c}_4 - \hat{c}^{\dagger}_1\hat{c}^{\dagger}_2\left\{\hat{c}_5, \hat{c}_3\right\}\hat{c}_4 + \hat{c}^{\dagger}_1\hat{c}^{\dagger}_2\hat{c}_3\left\{\hat{c}_5, \hat{c}_4\right\} \\
&= -\delta_{5,1}\hat{c}^{\dagger}_2\hat{c}_3\hat{c}_4 + \hat{c}^{\dagger}_1\delta_{5,2}\hat{c}_3\hat{c}_4.
\end{aligned} \tag{G.4}$$

We can therefore calculate the commutator with H_0 from Eq. (G.1)

$$\begin{aligned}\left[\hat{H}_0, \hat{c}_{\mathbf{k}m\sigma}(\tau)\right] &= \sum_{\substack{\mathbf{a}\\xy\\\rho}} \varepsilon_{\mathbf{a}xy}\left[\hat{c}^\dagger_{\mathbf{a},x\rho}\hat{c}_{\mathbf{a}y\rho}, \hat{c}_{\mathbf{k}m\sigma}(\tau)\right] \\ &= -\sum_{\substack{\mathbf{a}\\xy\\\rho}} \varepsilon_{\mathbf{k}xy}\left(\delta_{\mathbf{a},\mathbf{k}}\delta_{x,m}\delta_{\rho,\sigma}\hat{c}_{\mathbf{a}y\rho}\right)(\tau) \\ &= -\sum_{y} \varepsilon_{\mathbf{k}my}\left(\hat{c}_{\mathbf{k}y\sigma}\right)(\tau)\,.\end{aligned} \tag{G.5}$$

Inserting this relation back in (G.1) we get

$$\begin{aligned}\frac{d}{d\tau}G^{\mathbf{k}}_{\substack{mm'\\\sigma}}(\tau) &= -\delta(\tau)\delta_{mm'} - \left\langle \mathcal{T}\left[\left[\hat{H}_0, \hat{c}_{\mathbf{k}m\sigma}(\tau)\right]\hat{c}^\dagger_{\mathbf{k}m'\sigma}(0)\right]\right\rangle \\ &= -\delta(\tau)\delta_{mm'} + \sum_{y}\varepsilon_{\mathbf{k}my}\left\langle \mathcal{T}\left[\hat{c}_{\mathbf{k}y\sigma}(\tau)\,\hat{c}^\dagger_{\mathbf{k}m'\sigma}(0)\right]\right\rangle \\ &= -\delta(\tau)\delta_{mm'} - \sum_{y}\varepsilon_{\mathbf{k}my}G^{\mathbf{k}}_{\substack{ym'\\\sigma}}(\tau).\end{aligned} \tag{G.6}$$

Applying the Fourier transform with respect to the imaginary time τ to both sides of the equation we can get to an explicit expression for the Green's function. The derivative is transformed elegantly by

$$\begin{aligned}\mathcal{F}\left[\frac{d}{d\tau}G^{\mathbf{k}}_{\substack{mm'\\\sigma}}(\tau)\right] &= \int_0^\beta e^{i\nu\tau}\frac{d}{d\tau}\left(G^{\mathbf{k}}_{\substack{mm'\\\sigma}}(\tau)\right)d\tau \\ &= \left[e^{i\nu\tau}G^{\mathbf{k}}_{\substack{mm'\\\sigma}}(\tau)\right]_0^\beta - \int_0^\beta \frac{d}{d\tau}\left(e^{i\nu\tau}\right)G^{\mathbf{k}}_{\substack{mm'\\\sigma}}(\tau)\,d\tau \\ &= \underbrace{-G^{\mathbf{k}}_{\substack{mm'\\\sigma}}(\beta) - G^{\mathbf{k}}_{\substack{mm'\\\sigma}}(0)}_{\equiv\,0\ (\mathrm{KMS})} - i\nu\int_0^\beta e^{i\nu\tau}G^{\mathbf{k}}_{\substack{mm'\\\sigma}}(\tau)\,d\tau \\ &= -i\nu\,\mathcal{F}\left[G^{\mathbf{k}}_{\substack{mm'\\\sigma}}(\tau)\right] = -i\nu\,G^{k}_{\substack{mm'\\\sigma}}\end{aligned} \tag{G.7}$$

and we finally arrive at

$$\begin{aligned}-i\nu\,G^{k}_{\substack{mm'\\\sigma}} &= -\delta_{mm'} - \sum_{y}\varepsilon_{\mathbf{k}my}G^{k}_{\substack{ym'\\\sigma}} \\ \implies \sum_{y}\left[(i\nu+\mu)\,\delta_{my} - \varepsilon_{\mathbf{k}my}\right]G^{k}_{\substack{ym'\\\sigma}} &= \delta_{mm'}.\end{aligned} \tag{G.8}$$

We expanded $\varepsilon_{\mathbf{k}my} \to \varepsilon_{\mathbf{k}my} - \mu\delta_{my}$ in conformance with the abbreviated grand canonical form of $\hat{H} \to \hat{H} - \mu\hat{N}$ and arrived at the non-interacting Green's function G_0 in the orbital basis. For

illustration this matrix equation reads for two orbitals

$$\left(\begin{bmatrix} i\nu+\mu & 0 \\ 0 & i\nu+\mu \end{bmatrix} - \begin{bmatrix} \varepsilon_{\mathbf{k}11} & \varepsilon_{\mathbf{k}12} \\ \varepsilon_{\mathbf{k}21} & \varepsilon_{\mathbf{k}22} \end{bmatrix}\right) \times \begin{bmatrix} G^k_{11} & G^k_{12} \\ G^k_{21} & G^k_{22} \end{bmatrix} = \begin{bmatrix} 1 & 0 \\ 0 & 1 \end{bmatrix}. \tag{G.9}$$

G.2 Interacting Green's function

From the Dyson equation

$$\begin{aligned} G &= G_0 + G_0 \Sigma G \\ \implies G^{-1} &= G_0^{-1} - \Sigma \end{aligned} \tag{G.10}$$

we can deduct that the (until now) ignored interaction term represents the indicated self-energy contribution $[\Sigma G]^{\mathbf{k}}_{\substack{mm' \\ \sigma}}$

$$\begin{aligned} -i\nu\, G^k_{\substack{mm' \\ \sigma}} &= -\delta_{mm'} - \sum_y \varepsilon_{\mathbf{k}my} G^k_{\substack{ym' \\ \sigma}} - \underbrace{[\Sigma G]^k_{\substack{mm' \\ \sigma}}}_{\text{from } \hat{U}^{\text{full}} \text{ commutator}} \\ \implies \sum_y \left[(i\nu+\mu)\,\delta_{my} - \varepsilon_{\mathbf{k}my} - \Sigma^k_{\substack{my \\ \sigma}} \right] G^k_{\substack{ym' \\ \sigma}} &= \delta_{mm'}. \end{aligned} \tag{G.11}$$

Let us now explicitly calculate this contribution:

$$\left[\hat{U}^{\text{full}}, \hat{c}_{\mathbf{k}m\sigma}(\tau)\right] = \frac{1}{2} \sum_{\substack{\mathbf{abb'} \\ xx'yy' \\ \rho\rho'}} U^{\mathbf{abb'}}_{xy'yx'} \left[\hat{c}^\dagger_{\mathbf{b'-a},y'\rho} \hat{c}^\dagger_{\mathbf{b}x\rho'} \hat{c}_{\mathbf{b-a},y\rho'} \hat{c}_{\mathbf{b'}x'\rho}, \hat{c}_{\mathbf{k}m\sigma}(\tau)\right] \tag{G.12}$$

The first term of Eq. (G.4) results in

$$\begin{aligned} &-\frac{1}{2} \sum_{\substack{\mathbf{abb'} \\ xx'yy' \\ \rho\rho'}} U^{\mathbf{abb'}}_{xy'yx'} \left(\delta_{\mathbf{b'-a},\mathbf{k}} \delta_{y',m} \delta_{\rho,\sigma} \hat{c}^\dagger_{\mathbf{b}x\rho'} \hat{c}_{\mathbf{b-a},y\rho'} \hat{c}_{\mathbf{b'}x'\rho}\right)(\tau) \\ &= -\frac{1}{2} \sum_{\substack{\mathbf{ab} \\ xx'y \\ \rho'}} U^{\mathbf{ab(k+a)}}_{xmyx'} \left(\hat{c}^\dagger_{\mathbf{b}x\rho'} \hat{c}_{\mathbf{b-a},y\rho'} \hat{c}_{\mathbf{k+a},x'\sigma}\right)(\tau) \\ &= -\frac{1}{2} \sum_{\substack{\mathbf{qk'} \\ lhn \\ \sigma'}} U^{-\mathbf{q(k'-q)(k-q)}}_{lmnh} \left(\hat{c}^\dagger_{\mathbf{k'-q},l\sigma'} \hat{c}_{\mathbf{k'}n\sigma'} \hat{c}_{\mathbf{k-q},h\sigma}\right)(\tau) \\ &\overset{\text{SW}}{=} -\frac{1}{2} \sum_{\substack{\mathbf{qk'} \\ lhn \\ \sigma'}} U^{\mathbf{qkk'}}_{mlhn} \left(\hat{c}^\dagger_{\mathbf{k'-q'},l\sigma'} \hat{c}_{\mathbf{k'}n\sigma'} \hat{c}_{\mathbf{k-q},h\sigma}\right)(\tau) \\ &= \frac{1}{2} \sum_{\substack{\mathbf{qk'} \\ lhn \\ \sigma'}} \left(U_{mlhn} + V^{\mathbf{q}}_{mlhn}\right) \left(\hat{c}^\dagger_{\mathbf{k'-q'},l\sigma'} \hat{c}_{\mathbf{k-q},h\sigma} \hat{c}_{\mathbf{k'}n\sigma'}\right)(\tau), \end{aligned} \tag{G.13}$$

where we renamed $x \to l$, $y \to n$, $x' \to h$, $\mathbf{a} \to -\mathbf{q}$, $\mathbf{b} \to \mathbf{k}' - \mathbf{q}$ and $\rho' \to \sigma'$ in the third line. Please note that summing over $-\mathbf{q}$ is identical to summing over $\mathbf{q}$ since we go through the whole Brillouin zone in both cases (the same applies for $\mathbf{k}' - \mathbf{q}$). The second term of Eq. (G.4) results in

$$\begin{aligned}
&\frac{1}{2} \sum_{\substack{\mathbf{abb'} \\ xx'yy' \\ \rho\rho'}} U^{\mathbf{abb'}}_{xy'yx'} \left(\hat{c}^\dagger_{\mathbf{b'}-\mathbf{a},y'\rho} \delta_{\mathbf{b},\mathbf{k}} \delta_{x,m} \delta_{\rho',\sigma} \hat{c}_{\mathbf{b}-\mathbf{a},y\rho'} \hat{c}_{\mathbf{b'}x'\rho} \right)(\tau) \\
&= \frac{1}{2} \sum_{\substack{\mathbf{ab'} \\ x'yy' \\ \rho}} U^{\mathbf{akb'}}_{my'yx'} \left(\hat{c}^\dagger_{\mathbf{b'}-\mathbf{a},y'\rho} \hat{c}_{\mathbf{k}-\mathbf{a},y\sigma} \hat{c}_{\mathbf{b'}x'\rho} \right)(\tau) \\
&= \frac{1}{2} \sum_{\substack{\mathbf{qk'} \\ lhn \\ \sigma'}} U^{\mathbf{qkk'}}_{mlhn} \left(\hat{c}^\dagger_{\mathbf{k'}-\mathbf{q},l\sigma'} \hat{c}_{\mathbf{k}-\mathbf{q},h\sigma} \hat{c}_{\mathbf{k'}n\sigma'} \right)(\tau) \\
&= \frac{1}{2} \sum_{\substack{\mathbf{qk'} \\ lhn \\ \sigma'}} \left(U_{mlhn} + V^{\mathbf{q}}_{mlhn} \right) \left(\hat{c}^\dagger_{\mathbf{k'}-\mathbf{q},l\sigma'} \hat{c}_{\mathbf{k}-\mathbf{q},h\sigma} \hat{c}_{\mathbf{k'}n\sigma'} \right)(\tau) ,
\end{aligned} \tag{G.14}$$

where we renamed $\mathbf{a} \to \mathbf{q}$, $\mathbf{b'} \to \mathbf{k'}$, $y' \to l$, $y \to h$, $x' \to n$ and $\rho \to \sigma'$ in the second to last line. By these renaming procedures we get two identical terms which we can directly supplement in our initial equation

$$\begin{aligned}
[\Sigma G]^{\mathbf{k}}_{\substack{mm' \\ \sigma}}(\tau) &= \sum_{\substack{\mathbf{qk'} \\ lhn \\ \sigma'}} \left(U_{mlhn} + V^{\mathbf{q}}_{mlhn} \right) \left\langle \mathcal{T} \left[\hat{c}^\dagger_{\mathbf{k'}-\mathbf{q'},l\sigma'}(\tau)\, \hat{c}_{\mathbf{k}-\mathbf{q},h\sigma}(\tau)\, \hat{c}_{\mathbf{k'}n\sigma'}(\tau)\, \hat{c}^\dagger_{\mathbf{k}m'\sigma}(0) \right] \right\rangle \\
&= \sum_{\substack{\mathbf{qk'} \\ lhn \\ \sigma'}} \left(U_{mlhn} + V^{\mathbf{q}}_{mlhn} \right) \left\langle \mathcal{T} \left[\hat{c}_{\mathbf{k'}n\sigma'}(\tau)\, \hat{c}^\dagger_{\mathbf{k'}-\mathbf{q'},l\sigma'}(\tau)\, \hat{c}_{\mathbf{k}-\mathbf{q},h\sigma}(\tau)\, \hat{c}^\dagger_{\mathbf{k}m'\sigma}(0) \right] \right\rangle \\
&= \lim_{\tau' \to \tau^+} \sum_{\substack{\mathbf{qk'} \\ lhn \\ \sigma'}} \left(U_{mlhn} + V^{\mathbf{q}}_{mlhn} \right) G^{\mathbf{qk'k}}_{\substack{nlhm' \\ \sigma'\sigma}}(\tau, \tau', \tau) .
\end{aligned} \tag{G.15}$$

The introduction of the limit is necessary if we want to separately evaluate the disconnected terms. This is done via

$$\begin{aligned}
[\Sigma G]^{\mathbf{k}}_{\substack{mm'\\ \sigma}}(\tau) &= \lim_{\tau'\to\tau^+} \sum_{\substack{\mathbf{qk}'\\ lhn\\ \sigma'}} \left(U_{mlhn} + V^{\mathbf{q}}_{mlhn}\right) \\
&\quad \times \left[G^{\mathbf{qk'k}\mathrm{con}}_{\substack{nlhm'\\ \sigma'\sigma}}(\tau,\tau',\tau) + \delta_{\mathbf{q0}} G^{\mathbf{k}'}_{\substack{nl\\ \sigma'}}(\tau-\tau') G^{\mathbf{k}}_{\substack{hm'\\ \sigma}}(\tau) - \delta_{\mathbf{kk}'}\delta_{\sigma\sigma'} G^{\mathbf{k}'}_{\substack{nm'\\ \sigma}}(\tau) G^{\mathbf{k-q}}_{\substack{hl\\ \sigma'}}(\tau-\tau') \right] \\
&= \sum_{\substack{\mathbf{qk}'\\ lhn\\ \sigma'}} \left(U_{mlhn} + V^{\mathbf{q}}_{mlhn}\right) \\
&\quad \times \left[G^{\mathbf{qk'k}\mathrm{con}}_{\substack{nlhm'\\ \sigma'\sigma}}(\tau,\tau,\tau) + \delta_{\mathbf{q0}} n^{\mathbf{k}'}_{\substack{ln\\ \sigma'}} G^{\mathbf{k}}_{\substack{hm'\\ \sigma}}(\tau) - \delta_{\mathbf{kk}'}\delta_{\sigma\sigma'} G^{\mathbf{k}'}_{\substack{nm'\\ \sigma}}(\tau) n^{\mathbf{k-q}}_{\substack{lh\\ \sigma'}} \right]
\end{aligned} \tag{G.16}$$

where we used the relation

$$\begin{aligned}
\lim_{\tau'\to\tau^+} G^{\mathbf{k}'}_{\substack{nl\\ \sigma'}}(\tau-\tau') &= -\lim_{\tau'\to\tau^+} \left\langle \mathcal{T}\left[\hat{c}_{\mathbf{k}'n\sigma'}(\tau)\hat{c}^\dagger_{\mathbf{k}'l\sigma'}(\tau')\right]\right\rangle \\
&= \lim_{\tau'\to\tau^+} \left\langle \hat{c}^\dagger_{\mathbf{k}'l\sigma'}(\tau')\hat{c}_{\mathbf{k}'n\sigma'}(\tau)\right\rangle = n^{\mathbf{k}'}_{\substack{ln\\ \sigma'}}.
\end{aligned} \tag{G.17}$$

When applying the Fourier transform to both sides of the equation we exploit the fact that transforming the equal-time object is equivalent to a summation over one fermionic and the bosonic frequency.

$$\int_0^\beta d\tau e^{i\nu\tau} G^{\mathbf{qk'k}\mathrm{con}}_{\substack{nlhm'\\ \sigma'\sigma}}(\tau,\tau,\tau) = G^{\mathbf{qk'}k\mathrm{con}}_{\substack{nlhm'\\ \sigma'\sigma}} = \frac{1}{\beta^2}\sum_{\omega\nu'} G^{qk'k\mathrm{con}}_{\substack{nlhm'\\ \sigma'\sigma}}. \tag{G.18}$$

Thus we get the expression

$$\begin{aligned}
[\Sigma G]^{k}_{\substack{mm'\\ \sigma}} &= \frac{1}{\beta^2}\sum_{\substack{qk'\\ lhn\\ \sigma'}} \left[U_{mlhn} + V^{\mathbf{q}}_{mlhn}\right] G^{qk'k\mathrm{con}}_{\substack{nlhm'\\ \sigma'\sigma}} \\
&\quad + \sum_{\substack{\mathbf{qk}'\\ lhn\\ \sigma'}} \left[U_{mlhn} + V^{\mathbf{q}}_{mlhn}\right] \left[\delta_{\mathbf{q0}} n^{\mathbf{k}'}_{\substack{ln\\ \sigma'}} G^{k}_{\substack{hm'\\ \sigma}} - \delta_{\mathbf{kk}'}\delta_{\sigma\sigma'} G^{k}_{\substack{nm'\\ \sigma}} n^{\mathbf{k-q}}_{\substack{lh\\ \sigma'}} \right],
\end{aligned} \tag{G.19}$$

from which we can extract the connected (first line) and the Hartree-Fock self-energy contribution (second line) by dividing off the right hand Green's function (the term 'connected' originates from the connected part of the two-particle Green's function which might be misleading at first glance)

$$\begin{aligned}
\Sigma^{k}_{\substack{mm'\\ \sigma}} &= \sum_{l'} [\Sigma G]^{k}_{\substack{ml'\\ \sigma}} \left[G^{-1}\right]^{k}_{\substack{l'm'\\ \sigma}} \\
&= \Sigma^{k\mathrm{con}}_{\substack{mm'\\ \sigma}} + \Sigma^{\mathbf{k}\mathrm{HF}}_{\substack{mm'\\ \sigma}}.
\end{aligned} \tag{G.20}$$

$$
\begin{aligned}
\Sigma^{\mathbf{k}\mathrm{HF}}_{\substack{mm' \\ \sigma}} &= \sum_{\substack{\mathbf{q}\mathbf{k}' \\ l'lhn \\ \sigma'}} \left[U_{mlhn} + V^{\mathbf{q}}_{mlhn}\right] \left[\delta_{\mathbf{q}\mathbf{0}} n^{\mathbf{k}'}_{\substack{ln \\ \sigma'}} G^{k}_{\substack{hl' \\ \sigma}} - \delta_{\mathbf{k}\mathbf{k}'}\delta_{\sigma\sigma'} G^{k}_{\substack{nl' \\ \sigma}} n^{\mathbf{k}-\mathbf{q}}_{\substack{lh \\ \sigma'}}\right] \left[G^{-1}\right]^{k}_{\substack{l'm' \\ \sigma}} \\
&= \sum_{\substack{\mathbf{q}\mathbf{k}' \\ l'lhn \\ \sigma'}} \left[U_{mlhn} + V^{\mathbf{q}}_{mlhn}\right] \delta_{\mathbf{q}\mathbf{0}} n^{\mathbf{k}'}_{\substack{ln \\ \sigma'}} \underbrace{G^{k}_{\substack{hl' \\ \sigma}} \left[G^{-1}\right]^{k}_{\substack{l'm' \\ \sigma}}}_{\delta_{hm'}} - \sum_{\substack{\mathbf{q}\mathbf{k}' \\ l'lhn \\ \sigma'}} \left[U_{mlhn} + V^{\mathbf{q}}_{mlhn}\right] \delta_{\mathbf{k}\mathbf{k}'}\delta_{\sigma\sigma'} \underbrace{G^{k}_{\substack{nl' \\ \sigma}} \left[G^{-1}\right]^{k}_{\substack{l'm' \\ \sigma}}}_{\delta_{nm'}} n^{\mathbf{k}-\mathbf{q}}_{\substack{lh \\ \sigma'}} \\
&= \underbrace{\sum_{\substack{\mathbf{k}' \\ ln \\ \sigma'}} \left[U_{mlm'n} + V^{\mathbf{0}}_{mlm'n}\right] n^{\mathbf{k}'}_{\substack{ln \\ \sigma'}}}_{\text{Hartree}} - \underbrace{\sum_{\substack{\mathbf{q} \\ lh}} \left[U_{mlhm'} + V^{\mathbf{q}}_{mlhm'}\right] n^{\mathbf{k}-\mathbf{q}}_{\substack{lh \\ \sigma}}}_{\text{Fock}}
\end{aligned}
\tag{G.21}
$$

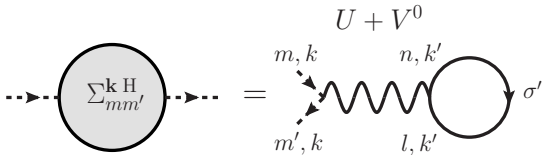

Figure G.1: Diagrammatic representation of the Hartree contribution to the self-energy. The occupation n_{ln} is represented by a fermionic loop from vertex n to l.

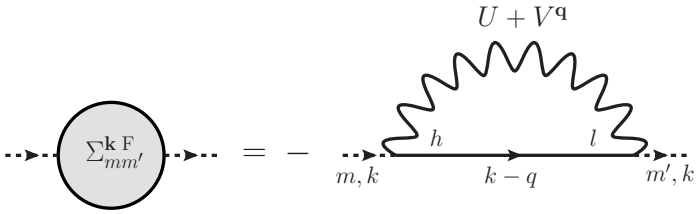

Figure G.2: Diagrammatic representation of the Fock contribution to the self-energy. Due to spin conservation the propagator $k - q$ must have the same spin as the implied incoming and outgoing propagators.

$$
\begin{aligned}
\Sigma^{k\mathrm{con}}_{\substack{mm'\\ \sigma}} &= \frac{1}{\beta^2}\sum_{\substack{qk'\\ l'lhn\\ \sigma'}}\left[U_{mlhn}+V^{\mathbf{q}}_{mlhn}\right]\left[G^{qk'k\mathrm{con}}_{\substack{nlhl'\\ \sigma'\sigma}}\right]\left[G^{-1}\right]^{k}_{\substack{l'm'\\ \sigma}}\\
&= -\frac{1}{\beta}\sum_{\substack{qk'\\ l'lhn,rstu\\ \sigma'}}\left[U_{mlhn}+V^{\mathbf{q}}_{mlhn}\right]\left[\chi^{qk'k'}_{0,nlsr}F^{qk'k}_{\substack{rstu\\ \sigma'\sigma}}G^{k}_{\substack{ul'\\ \sigma}}G^{k-q}_{\substack{ht\\ \sigma}}\right]\left[G^{-1}\right]^{k}_{\substack{l'm'\\ \sigma}}\\
&= -\frac{1}{\beta}\sum_{\substack{qk'\\ lhn,rst\\ \sigma'}}\left[U_{mlhn}+V^{\mathbf{q}}_{mlhn}\right]\left[\chi^{qk'k'}_{0,nlsr}F^{qk'k}_{\substack{rstm'\\ \sigma'\sigma}}G^{k-q}_{\substack{ht\\ \sigma}}\right]\\
&= -\frac{1}{\beta}\sum_{\substack{qk'\\ lhn,rst}}\left[U_{mlhn}+V^{\mathbf{q}}_{mlhn}\right]\left[\chi^{qk'k'}_{0,nlsr}F^{qk'k}_{\substack{rstm'\\ D}}G^{k-q}_{\substack{ht\\ \sigma}}\right]
\end{aligned}
\tag{G.22}
$$

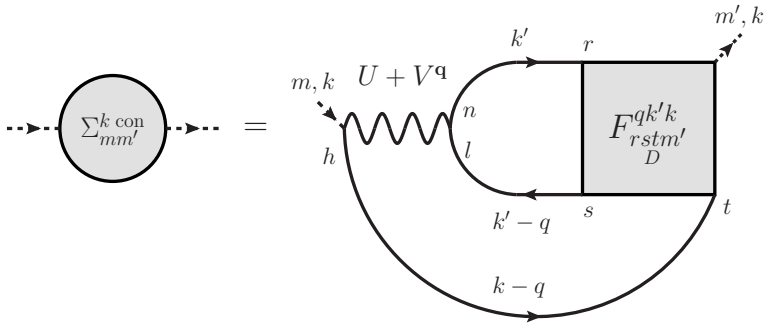

Figure G.3: Diagrammatic representation of the connected contribution to the self-energy containing the full vertex $F^{qk'k}_{D}$.

In order to get the final DΓA self-energy we have now to insert the crossing symmetric non-local full vertex derived in Appendix F

$$
F^{qkk'}_{\substack{lmm'l'\\ D}} = F^{\omega\nu\nu'}_{\substack{lmm'l'\\ D}} + F^{q\nu\nu',\mathrm{nl}}_{\substack{lmm'l'\\ D,ph}} - \frac{1}{2}F^{(k'-k)(\nu'-\omega)\nu',\mathrm{nl}}_{\substack{m'mll'\\ D,\mathrm{ph}}} - \frac{3}{2}F^{(k'-k)(\nu'-\omega)\nu',\mathrm{nl}}_{\substack{m'mll'\\ M,\mathrm{ph}}}.
$$

By dropping the ‘ph’ label for clarity we can extract the different contributions

$$\Sigma^{k\mathrm{con}} = \Sigma^{k,\mathrm{Uloc}} + \Sigma^{k,\mathrm{Vloc}} + \Sigma^{k,\mathrm{ph}} + \Sigma^{k,U\overline{\mathrm{ph}}} + \Sigma^{k,V\overline{\mathrm{ph}}}$$

$$\Sigma^{k,\mathrm{Uloc}} = -\frac{1}{\beta}\sum_{\substack{qν'\\lhn,rst}} [U_{mlhn}]\left[\chi^{qν'ν'}_{0,nlsr} F^{ων'ν}_{D,rstm'} G^{k-q}_{ht,σ}\right] \tag{G.23a}$$

$$\Sigma^{k,\mathrm{Vloc}} = -\frac{1}{\beta}\sum_{\substack{qν'\\lhn,rst}} \left[V^{\mathbf{q}}_{mlhn}\right]\left[\chi^{qν'ν'}_{0,nlsr} F^{ων'ν}_{D,rstm'} G^{k-q}_{ht,σ}\right] \tag{G.23b}$$

$$\Sigma^{k,\mathrm{ph}} = -\frac{1}{\beta}\sum_{\substack{qν'\\lhn,rst}} \left[U_{mlhn} + V^{\mathbf{q}}_{mlhn}\right]\left[\chi^{qν'ν'}_{0,nlsr} F^{qν'ν,\mathrm{nl}}_{D,rstm'} G^{k-q}_{ht,σ}\right] \tag{G.23c}$$

$$\begin{aligned}\Sigma^{k,U\overline{\mathrm{ph}}} &= -\frac{1}{\beta}\sum_{\substack{qk'\\lhn,rst}} [U_{mlhn}]\left[\chi^{qk'k'}_{0,nlsr}\left(-\frac{1}{2}F^{(k-k')(ν-ω)ν,\mathrm{nl}}_{D,tsrm'} - \frac{3}{2}F^{(k-k')(ν-ω)ν,\mathrm{nl}}_{M,tsrm'}\right) G^{k-q}_{ht,σ}\right]\\ &\overset{\text{relabelling}}{=} \frac{1}{\beta}\sum_{\substack{qk'\\lhn,rst}} [U_{mlnh}]\left[\chi^{qk'k'}_{0,nlsr}\left(\frac{1}{2}F^{qν'ν,\mathrm{nl}}_{D,rstm'} + \frac{3}{2}F^{qν'ν,\mathrm{nl}}_{M,rstm'}\right) G^{k-q}_{ht,σ}\right]\\ &= \frac{1}{\beta}\sum_{\substack{qk'\\lhn,rst}} \left[\tilde{U}_{mlhn}\right]\left[\chi^{qk'k'}_{0,nlsr}\left(\frac{1}{2}F^{qν'ν,\mathrm{nl}}_{D,rstm'} + \frac{3}{2}F^{qν'ν,\mathrm{nl}}_{M,rstm'}\right) G^{k-q}_{ht,σ}\right]\end{aligned} \tag{G.23d}$$

$$\begin{aligned}\Sigma^{k,V\overline{\mathrm{ph}}} &= -\frac{1}{\beta}\sum_{\substack{qk'\\lhn,rst}} \left[V^{\mathbf{q}}_{mlhn}\right]\left[\chi^{qk'k'}_{0,nlsr}\left(-\frac{1}{2}F^{(k-k')(ν-ω)ν,\mathrm{nl}}_{D,tsrm'} - \frac{3}{2}F^{(k-k')(ν-ω)ν,\mathrm{nl}}_{M,tsrm'}\right) G^{k-q}_{ht,σ}\right]\\ &\overset{\text{relabelling}}{=} \frac{1}{\beta}\sum_{\substack{qk'\\lhn,rst}} \left[V^{\mathbf{k}-\mathbf{k}'}_{mlnh}\right]\left[\chi^{qk'k'}_{0,nlsr}\left(\frac{1}{2}F^{qν'ν,\mathrm{nl}}_{D,rstm'} + \frac{3}{2}F^{qν'ν,\mathrm{nl}}_{M,rstm'}\right) G^{k-q}_{ht,σ}\right]\\ &= \frac{1}{\beta}\sum_{\substack{qk'\\lhn,rst}} \left[\tilde{V}^{\mathbf{k}-\mathbf{k}'}_{mlhn}\right]\left[\chi^{qk'k'}_{0,nlsr}\left(\frac{1}{2}F^{qν'ν,\mathrm{nl}}_{D,rstm'} + \frac{3}{2}F^{qν'ν,\mathrm{nl}}_{M,rstm'}\right) G^{k-q}_{ht,σ}\right]\end{aligned} \tag{G.23e}$$

where we we introduced the tilde objects for convenience in the implementation by

$$\begin{aligned}U_{mlnh} &\equiv \tilde{U}_{mlhn}\\ V^{\mathbf{k}-\mathbf{k}'}_{mlnh} &\equiv \tilde{V}^{\mathbf{k}-\mathbf{k}'}_{mlhn}.\end{aligned} \tag{G.24}$$

The transformation marked with ‘relabelling’ is diagrammatically illustrated for the full connected self-energy contribution in Fig. G.4 and allows us to transform to a, for us, much more convenient frequency and momentum notation. Please note that this has nothing to do with crossing symmetry (thus no additional (-1) factors).

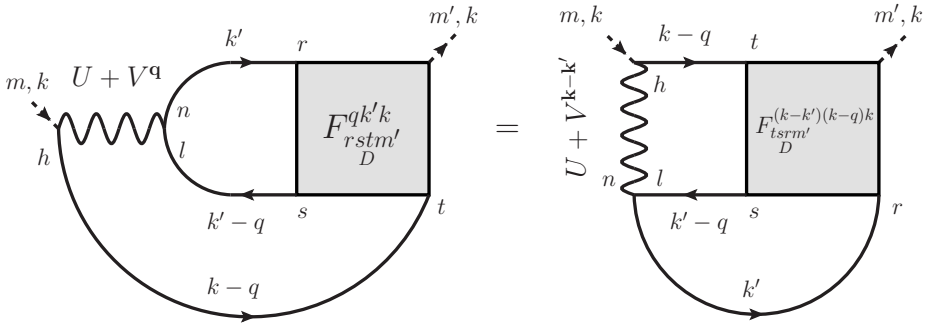

Figure G.4: Diagrammatic representation of the relabelling procedure exploited in (G.23d), (G.23e) and (G.33). By flipping both the interaction and the vertex we get the same diagram with different frequency and momentum dependencies.

By introducing so-called three-leg (boson-fermion) vertices we can simplify these equations (the fully local three-leg $\gamma_r^{\omega\nu}$ is illustrated in Fig. G.5).

$$\gamma^{\omega\nu}_{\substack{lmm'l'\\ r}} \equiv \sum_{\substack{\nu'\\ n'h'}} \chi^{\omega\nu'\nu'}_{0,lmn'h'} F^{\omega\nu'\nu}_{\substack{h'n'm'l'\\ r}} \tag{G.25}$$

$$\gamma^{q\nu}_{\substack{lmm'l'\\ r}} \equiv \sum_{\substack{\nu'\\ n'h'}} \chi^{q\nu'\nu',\mathrm{nl}}_{0,lmn'h'} F^{\omega\nu'\nu}_{\substack{h'n'm'l'\\ r}} \tag{G.26}$$

$$\begin{aligned} \eta^{q\nu}_{\substack{lmm'l'\\ r}} &\equiv \sum_{\substack{\nu'\\ n'h'}} \chi^{q\nu'\nu'}_{0,lmn'h'} F^{q\nu'\nu}_{\substack{h'n'm'l'\\ r}} - \sum_{\substack{\nu'\\ n'h'}} \chi^{\omega\nu'\nu'}_{0,lmn'h'} F^{\omega\nu'\nu}_{\substack{h'n'm'l'\\ r}} \\ &= \sum_{\substack{\nu'\\ n'h'}} \chi^{q\nu'\nu'}_{0,lmn'h'} F^{q\nu'\nu}_{\substack{h'n'm'l'\\ r}} - \gamma^{\omega\nu}_{\substack{lmm'l'\\ r}} \end{aligned} \tag{G.27}$$

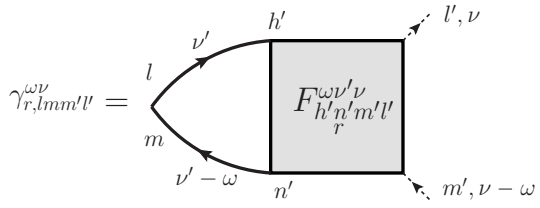

Figure G.5: Diagrammatic representation of the construction of a so-called three-leg vertex. By summing over one fermionic Matsubara frequency we 'close' the diagram. The resulting vertex thus has one less frequency dependence while retaining its full orbital dependencies.

For the first four terms this leads to

$$\begin{aligned}\Sigma^{k,\mathrm{Uloc}} &= -\frac{1}{\beta}\sum_{\substack{qν'\\lhn,rst}}[U_{mlhn}]\left[\chi^{ων'ν'}_{0,nlsr}F^{ων'ν}_{rstm',D}G^{k-q}_{ht,σ}\right]-\frac{1}{\beta}\sum_{\substack{qν'\\lhn,rst}}[U_{mlhn}]\left[\chi^{qν'ν',\mathrm{nl}}_{0,nlsr}F^{ων'ν}_{rstm',D}G^{k-q}_{ht,σ}\right]\\ &= \Sigma^{ν}_{\mathrm{DMFT}}-\Sigma^{U,\mathrm{loc}}_{\mathrm{HF}}-\frac{1}{\beta}\sum_{\substack{q\\lhn,t}}[U_{mlhn}]\left[\gamma^{qν}_{nltm',D}G^{k-q}_{ht,σ}\right]\end{aligned} \tag{G.28}$$

$$\begin{aligned}\Sigma^{k,\mathrm{Vloc}} &= -\frac{1}{\beta}\sum_{\substack{qν'\\lhn,rst}}\left[V^{\mathbf{q}}_{mlhn}\right]\left[\chi^{qν'ν'}_{0,nlsr}F^{ων'ν}_{rstm',D}G^{k-q}_{ht,σ}\right]\\ &= -\frac{1}{\beta}\sum_{\substack{qν'\\lhn,rst}}\left[V^{\mathbf{q}}_{mlhn}\right]\left[\left(\chi^{qν'ν',\mathrm{nl}}_{0,nlsr}+\chi^{ων'ν'}_{0,nlsr}\right)F^{ων'ν}_{rstm',D}G^{k-q}_{ht,σ}\right]\\ &= -\frac{1}{\beta}\sum_{\substack{q\\lhn,rst}}\left[V^{\mathbf{q}}_{mlhn}\right]\left[\left(\gamma^{qν}_{nltm',D}+\gamma^{ων}_{nltm',D}\right)G^{k-q}_{ht,σ}\right]\end{aligned} \tag{G.29}$$

$$\begin{aligned}\Sigma^{k,\mathrm{ph}} &= -\frac{1}{\beta}\sum_{\substack{qν'\\lhn,rst}}\left[U_{mlhn}+V^{\mathbf{q}}_{mlhn}\right]\left[\chi^{qν'ν'}_{0,nlsr}F^{qν'ν,\mathrm{nl}}_{rstm',D}G^{k-q}_{ht,σ}\right]\\ &= -\frac{1}{\beta}\sum_{\substack{qν'\\lhn,rst}}\left[U_{mlhn}+V^{\mathbf{q}}_{mlhn}\right]\left[\left(\chi^{qν'ν'}_{0,nlsr}F^{qν'ν}_{rstm',D}-\chi^{ων'ν'}_{0,nlsr}F^{ων'ν}_{rstm',D}-\chi^{qν'ν',\mathrm{nl}}_{0,nlsr}F^{ων'ν}_{rstm',D}\right)G^{k-q}_{ht,σ}\right]\\ &= -\frac{1}{\beta}\sum_{\substack{q\\lhn,t}}\left[U_{mlhn}+V^{\mathbf{q}}_{mlhn}\right]\left[\left(\eta^{qν}_{nltm',D}-\gamma^{qν}_{nltm',D}\right)G^{k-q}_{ht,σ}\right]\end{aligned} \tag{G.30}$$

$$\begin{aligned}\Sigma^{k,U\overline{\mathrm{ph}}} &= \frac{1}{\beta}\sum_{\substack{qk'\\lhn,rst}}\left[\tilde{U}_{mlhn}\right]\left[\chi^{qk'k'}_{0,nlsr}\left(\frac{1}{2}F^{qν'ν,\mathrm{nl}}_{rstm',D}+\frac{3}{2}F^{qν'ν,\mathrm{nl}}_{rstm',M}\right)\right]G^{k-q}_{ht,σ}\\ &= \frac{1}{\beta}\sum_{\substack{qν'\\lhn,rst}}\left[\tilde{U}_{mlhn}\right]\left[\chi^{qν'ν'}_{0,nlsr}\left(\frac{1}{2}F^{qν'ν}_{rstm',D}+\frac{3}{2}F^{qν'ν}_{rstm',M}\right)-\chi^{qν'ν'}_{0,nlsr}\left(\frac{1}{2}F^{ων'ν}_{rstm',D}+\frac{3}{2}F^{ων'ν}_{rstm',M}\right)\right]G^{k-q}_{ht,σ}\\ &= \frac{1}{\beta}\sum_{\substack{qν'\\lhn,rst}}\left[\tilde{U}_{mlhn}\right]\left[\frac{1}{2}\left(\chi^{qν'ν'}_{0,nlsr}F^{qν'ν}_{rstm',D}-\chi^{ων'ν'}_{0,nlsr}F^{ων'ν}_{rstm',D}-\chi^{qν'ν',\mathrm{nl}}_{0,nlsr}F^{ων'ν}_{rstm',D}\right)\right.\\ &\qquad\left.+\frac{3}{2}\left(\chi^{qν'ν'}_{0,nlsr}F^{qν'ν}_{rstm',D}-\chi^{ων'ν'}_{0,nlsr}F^{ων'ν}_{rstm',D}-\chi^{qν'ν',\mathrm{nl}}_{0,nlsr}F^{ων'ν}_{rstm',D}\right)\right]G^{k-q}_{ht,σ}\\ &= \frac{1}{\beta}\sum_{\substack{q\\lhn,t}}\left[\tilde{U}_{mlhn}\right]\left[\frac{1}{2}\left(\eta^{qν}_{nltm',D}-\gamma^{qν}_{nltm',D}\right)+\frac{3}{2}\left(\eta^{qν}_{nltm',M}-\gamma^{qν}_{nltm',M}\right)\right]G^{k-q}_{ht,σ}\end{aligned} \tag{G.31}$$

In order to simplify this last expression further, we have to first expand the two γ_r vertices

$$\begin{aligned}
&\frac{1}{\beta}\sum_{\substack{q\\lhn,t}}\left[\tilde{U}_{mlhn}\right]\left[-\frac{1}{2}\underset{D}{\gamma^{q\nu}_{nltm'}}-\frac{3}{2}\underset{M}{\gamma^{q\nu}_{nltm'}}\right]G^{k-q}_{\substack{ht\\\sigma}}\\
&=\frac{1}{\beta}\sum_{\substack{q\nu'\\lhn,rst}}\left[\tilde{U}_{mlhn}\right]\left[-\frac{1}{2}\chi^{q\nu'\nu',\mathrm{nl}}_{0,nlsr}\underset{D}{F^{\omega\nu'\nu}_{rstm'}}-\frac{3}{2}\chi^{q\nu'\nu',\mathrm{nl}}_{0,nlsr}\underset{M}{F^{\omega\nu'\nu,\mathrm{nl}}_{rstm'}}\right]G^{k-q}_{\substack{ht\\\sigma}}\\
&=\frac{1}{\beta}\sum_{\substack{q\nu'\\lhn,rst}}\left[\tilde{U}_{mlhn}\right]\left[-\frac{1}{2}\left(\chi^{q,\nu'\nu'}_{0,nlsr}-\chi^{\omega,\nu'\nu'}_{0,nlsr}\right)\underset{D}{F^{\omega\nu'\nu}_{rstm'}}-\frac{3}{2}\left(\chi^{q,\nu'\nu'}_{0,nlsr}-\chi^{\omega,\nu'\nu'}_{0,nlsr}\right)\underset{M}{F^{\omega\nu'\nu}_{rstm'}}\right]G^{k-q}_{\substack{ht\\\sigma}}
\end{aligned}\tag{G.32}$$

Now we separate the q-dependent bare susceptibilities from the local ones. This is necessary because the application of symmetry operations onto the full vertices described above require that all 'edges' have the same type of Green's function connected to it.

$$\begin{aligned}
&\frac{1}{\beta}\sum_{\substack{q\nu'\\lhn,rst}}\left[\tilde{U}_{mlhn}\right]\left[\chi^{q,\nu'\nu'}_{0,nlsr}\left(-\frac{1}{2}\underset{D}{F^{\omega\nu'\nu}_{rstm'}}-\frac{3}{2}\underset{M}{F^{\omega\nu'\nu}_{rstm'}}\right)+\chi^{\omega,\nu'\nu'}_{0,nlsr}\left(\frac{1}{2}\underset{D}{F^{\omega\nu'\nu}_{rstm'}}+\frac{3}{2}\underset{M}{F^{\omega\nu'\nu}_{rstm'}}\right)\right]G^{k-q}_{\substack{ht\\\sigma}}\\
&=\frac{1}{\beta}\sum_{\substack{q\nu'\\lhn,rst}}\left[\tilde{U}_{mlhn}\right]\left[\chi^{q,\nu'\nu'}_{0,nlsr}\left(-\frac{1}{2}\underset{D}{F^{\omega\nu'\nu}_{rstm'}}-\frac{3}{2}\underset{M}{F^{\omega\nu'\nu}_{rstm'}}\right)\right]G^{k-q}_{\substack{ht\\\sigma}}\\
&+\frac{1}{\beta}\sum_{\substack{\omega\nu'\\lhn,rst}}\left[\tilde{U}_{mlhn}\right]\left[\chi^{\omega,\nu'\nu'}_{0,nlsr}\left(\frac{1}{2}\underset{D}{F^{\omega\nu'\nu}_{rstm'}}+\frac{3}{2}\underset{M}{F^{\omega\nu'\nu}_{rstm'}}\right)\right]G^{\nu-\omega}_{\substack{ht\\\sigma}}\\
&\overset{\mathrm{CR}}{=}\frac{1}{\beta}\sum_{\substack{q\nu'\\lhn,rst}}\left[\tilde{U}_{mlhn}\right]\left[\chi^{q,\nu'\nu'}_{0,nlsr}\underset{D}{F^{(\nu-\nu')(\nu-\omega)\nu}_{tsrm'}}\right]G^{k-q}_{\substack{ht\\\sigma}}-\frac{1}{\beta}\sum_{\substack{\omega\nu'\\lhn,rst}}\left[\tilde{U}_{mlhn}\right]\left[\chi^{\omega,\nu'\nu'}_{0,nlsr}\underset{D}{F^{(\nu-\nu')(\nu-\omega)\nu}_{tsrm'}}\right]G^{\nu-\omega}_{\substack{ht\\\sigma}}\\
&\overset{\text{relabelling}}{=}\frac{1}{\beta}\sum_{\substack{q\nu'\\lhn,rst}}\left[U_{mlhn}\right]\left[\chi^{q,\nu'\nu'}_{0,nlsr}\underset{D}{F^{\omega\nu'\nu}_{rstm'}}\right]G^{k-q}_{\substack{ht\\\sigma}}-\frac{1}{\beta}\sum_{\substack{\omega\nu'\\lhn,rst}}\left[U_{mlhn}\right]\left[\chi^{\omega,\nu'\nu'}_{0,nlsr}\underset{D}{F^{\omega\nu'\nu}_{rstm'}}\right]G^{\nu-\omega}_{\substack{ht\\\sigma}}\\
&=\frac{1}{\beta}\sum_{\substack{q\nu'\\lhn,rst}}\left[U_{mlhn}\right]\left[\chi^{q,\nu'\nu',\mathrm{nl}}_{0,nlsr}\underset{D}{F^{\omega\nu'\nu}_{rstm'}}\right]G^{k-q}_{\substack{ht\\\sigma}}\\
&=\frac{1}{\beta}\sum_{\substack{q\\lhn,t}}\left[U_{mlhn}\right]\left[\underset{D}{\gamma^{q\nu}_{nltm'}}\right]G^{k-q}_{\substack{ht\\\sigma}}
\end{aligned}\tag{G.33}$$

The crossing symmetry transformation is done with the help of Eq. (F.9). The 'relabelling' transformation is done via relabelling the interaction and the vertex which we already exploited previously and is shown in Fig. G.4.

Gathering all terms with the exception of $\Sigma^{k,V\overline{\text{ph}}}$ (in order to stay consistent with the assumption of no explicit $\mathbf{k}$ and $\mathbf{k}'$ dependence within the non-local interactions) we arrive at the full DΓA self-energy description.

$$\begin{aligned}
\Sigma^{\text{DΓA},k} &= \Sigma^{k,\text{Uloc}} + \Sigma^{k,\text{Vloc}} + \Sigma^{k,\text{ph}} + \Sigma^{k,U\overline{\text{ph}}} + \Sigma^{\mathbf{k}\text{HF}} \\
&= \Sigma^{\text{DMFT},\nu}_{mm'} - \Sigma^{U,\text{loc}}_{\text{HF}} - \frac{1}{\beta}\sum_{\substack{q \\ lhn,t}} [U_{mlhn}] \left[\gamma^{q\nu}_{\substack{nltm' \\ D}}\right] G^{k-q}_{\substack{ht \\ \sigma}} \\
&- \frac{1}{\beta}\sum_{\substack{q \\ lhn,rst}} \left[V^{\mathbf{q}}_{mlhn}\right] \left[\gamma^{q\nu}_{\substack{nltm' \\ D}} + \gamma^{\omega\nu}_{\substack{nltm' \\ D}}\right] G^{k-q}_{\substack{ht \\ \sigma}} \\
&- \frac{1}{\beta}\sum_{\substack{q \\ lhn,t}} \left[U_{mlhn} + V^{\mathbf{q}}_{mlhn}\right] \left[\eta^{q\nu}_{\substack{nltm' \\ D}} - \gamma^{q\nu}_{\substack{nltm' \\ D}}\right] G^{k-q}_{\substack{ht \\ \sigma}} \\
&+ \frac{1}{\beta}\sum_{\substack{q \\ lhn,t}} \left[\tilde{U}_{mlhn}\right] \left[\frac{1}{2}\eta^{q\nu}_{\substack{nltm' \\ D}} + \frac{3}{2}\eta^{q\nu}_{\substack{nltm' \\ M}}\right] G^{k-q}_{\substack{ht \\ \sigma}} \\
&+ \frac{1}{\beta}\sum_{\substack{q \\ lhn,t}} [U_{mlhn}] \left[\gamma^{q\nu}_{\substack{nltm' \\ D}}\right] G^{k-q}_{\substack{ht \\ \sigma}} \\
&+ \sum_{\substack{\mathbf{k}' \\ ln \\ \sigma'}} \left[U_{mlm'n} + V^{\mathbf{0}}_{mlm'n}\right] n^{\mathbf{k}'}_{\substack{ln \\ \sigma'}} - \sum_{\substack{\mathbf{q} \\ hn}} \left[U_{mlhm'} + V^{\mathbf{q}}_{mlhm'}\right] n^{\mathbf{k}-\mathbf{q}}_{\substack{lh \\ \sigma}}
\end{aligned} \tag{G.34}$$

Canceling the local Hartree-Fock terms with $\Sigma^{U,\text{loc}}_{\text{HF}}$ (we only derived the connected part of the DMFT self-energy in $\Sigma^{k,\text{Uloc}}$) and further simplifying the rest we get the final expression

$$\begin{aligned}
\Sigma^{\text{DΓA},k}_{mm'} &= \Sigma^{\text{DMFT},\nu}_{mm'} - \frac{1}{\beta}\sum_{\substack{q \\ lhn,t}} \left[U_{mlhn} + V^{\mathbf{q}}_{mlhn} - \frac{1}{2}\tilde{U}_{mlhn}\right] \left[\eta^{q\nu}_{\substack{nltm' \\ D}}\right] G^{k-q}_{\substack{ht \\ \sigma}} \\
&+ \frac{1}{\beta}\sum_{\substack{q \\ lhn,t}} \left[\tilde{U}_{mlhn}\right] \left[\frac{3}{2}\eta^{q\nu}_{\substack{nltm' \\ M}}\right] G^{k-q}_{\substack{ht \\ \sigma}} \\
&+ \frac{1}{\beta}\sum_{\substack{q \\ lhn,t}} [U_{mlhn}] \left[\gamma^{q\nu}_{\substack{nltm' \\ D}}\right] G^{k-q}_{\substack{ht \\ \sigma}} \\
&- \frac{1}{\beta}\sum_{\substack{q \\ lhn,t}} \left[V^{\mathbf{q}}_{mlhn}\right] \left[\gamma^{\omega\nu}_{\substack{nltm' \\ D}}\right] G^{k-q}_{\substack{ht \\ \sigma}} \\
&+ \sum_{\substack{\mathbf{k}' \\ ln \\ \sigma'}} \left[V^{\mathbf{0}}_{mlm'n}\right] n^{\mathbf{k}'}_{\substack{ln \\ \sigma'}} - \sum_{\substack{\mathbf{q} \\ lh}} \left[V^{\mathbf{q}}_{mlhm'}\right] n^{\mathbf{k}-\mathbf{q}}_{\substack{lh \\ \sigma}}.
\end{aligned} \tag{G.35}$$

Appendix H Momentum-dependent susceptibilities in AbinitioDΓA

As in the derivation of the `AbinitioDΓA` diagrammatic, our full vertex F is not dependent on the momenta $\mathbf{k}$ or $\mathbf{k}'$. We can therefore define the momentum q-dependent susceptibilities generalized to three frequencies, independent of $\mathbf{k}$,$\mathbf{k}'$ (see Fig. H.1)

$$\begin{aligned}
\chi^{q\nu\nu'}_{r,lmm'l'} &= \chi^{q\nu\nu'}_{0,lmm'l'}\delta_{\nu\nu'} + \sum_{\substack{\nu''\nu'''\\ nhh'n'}} \chi^{q\nu\nu''}_{0,lmhn}\delta_{\nu\nu''}F^{q\nu''\nu'''}_{r,nhh'n'}\chi^{q\nu'''\nu'}_{0,n'h'm'l'}\delta_{\nu'''\nu'} \\
&= \chi^{q\nu\nu'}_{0,lmm'l'}\delta_{\nu\nu'} + \sum_{nhh'n'} \chi^{q\nu\nu}_{0,lmhn}F^{q\nu\nu'}_{r,nhh'n'}\chi^{q\nu'\nu'}_{0,n'h'm'l'} \\
&= \chi^{\omega\nu\nu'}_{0,lmm'l'}\delta_{\nu\nu'} + \sum_{nhh'n'} \chi^{\omega\nu\nu}_{0,lmhn}F^{\omega\nu\nu'}_{r,nhh'n'}\chi^{\omega\nu'\nu'}_{0,n'h'm'l'} \\
&+ \chi^{q\nu\nu',\mathrm{nl}}_{0,lmm'l'}\delta_{\nu\nu'} - \sum_{nhh'n'} \chi^{\omega\nu\nu}_{0,lmhn}F^{\omega\nu\nu'}_{r,nhh'n'}\chi^{\omega\nu'\nu'}_{0,n'h'm'l'} + \sum_{nhh'n'} \chi^{q\nu\nu}_{0,lmhn}F^{q\nu\nu'}_{r,nhh'n'}\chi^{q\nu'\nu'}_{0,n'h'm'l'} \\
&= \chi^{\omega\nu\nu'}_{r,lmm'l'} + \chi^{q\nu\nu',\mathrm{nl}}_{0,lmm'l'}\delta_{\nu\nu'} - \sum_{nhh'n'} \chi^{\omega\nu\nu}_{0,lmhn}F^{\omega\nu\nu'}_{r,nhh'n'}\chi^{\omega\nu'\nu'}_{0,n'h'm'l'} + \sum_{nhh'n'} \chi^{q\nu\nu}_{0,lmhn}F^{q\nu\nu'}_{r,nhh'n'}\chi^{q\nu'\nu'}_{0,n'h'm'l'} \\
&= \chi^{\omega\nu\nu'}_{r,lmm'l'} + \chi^{q\nu\nu',\mathrm{nl}}_{0,lmm'l'}\delta_{\nu\nu'} + \sum_{nhh'n'} \chi^{\omega\nu\nu}_{0,lmhn}F^{\omega\nu\nu'}_{r,nhh'n'}\chi^{q\nu'\nu',\mathrm{nl}}_{0,n'h'm'l'} \\
&\qquad + \sum_{nhh'n'} \left[\chi^{q\nu\nu}_{0,lmhn}F^{q\nu\nu'}_{r,nhh'n'} - \chi^{\omega\nu\nu}_{0,lmhn}F^{\omega\nu\nu'}_{r,nhh'n'}\right]\chi^{q\nu'\nu'}_{0,n'h'm'l'}
\end{aligned} \tag{H.1}$$

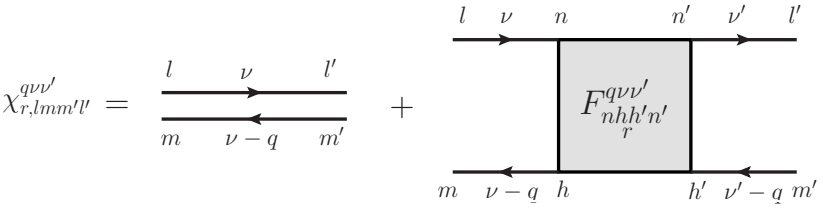

Figure H.1: Diagrammatic representation of the generalized susceptibilities. The implied frequency dependent propagators are obtained via a k-sum where the q dependence is preserved.

The usual $\frac{1}{\beta}$ factors which accompany each fermionic frequency sum are already contained in the first equation. The *physical* susceptibilities can be obtained now by summing over both independent fermionic frequencies, i.e. closing the diagrams on both sides, see Fig. H.2.

$$\begin{aligned}\chi^{q}_{\substack{lmm'l'\\ r}} &= \frac{1}{\beta^2}\sum_{\nu\nu'}\chi^{q\nu\nu'}_{\substack{lmm'l'\\ r}} \\ &= \chi^{\omega}_{\substack{lmm'l'\\ r}} + \chi^{q,\mathrm{nl}}_{0,lmm'l'} + \frac{1}{\beta^2}\sum_{\substack{\nu'\\ h'n'}}\gamma^{\omega\nu'}_{\substack{lmh'n'\\ r}}\chi^{q\nu'\nu',\mathrm{nl}}_{0,n'h'm'l'} + \frac{1}{\beta^2}\sum_{\substack{\nu'\\ h'n'}}\eta^{q\nu'}_{\substack{lmh'n'\\ r}}\chi^{q\nu'\nu'}_{0,n'h'm'l'}\end{aligned} \tag{H.2}$$

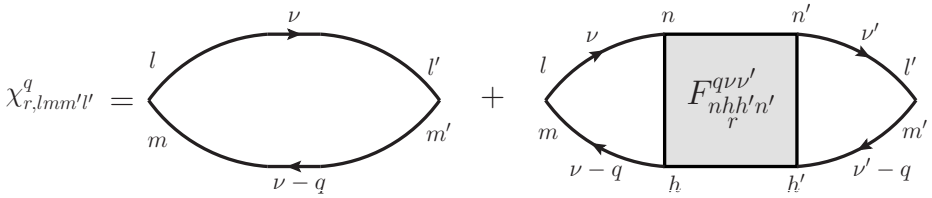

Figure H.2: Diagrammatic representation of the physical susceptibilities. The summation over the fermionic frequencies on the left- (ν) and the right-hand side (ν') is represented by the closure of the diagram.

Appendix I Three-leg implementation in AbinitioDΓA

By implementing a consistent orbital compound index structure in all objects as shown in [24, 22], we generally do not have to worry about them anymore when doing internal linear algebra operations. The orbital summations used throughout the text are recovered by matrix multiplications of these objects and because of that, and for clarity, we will completely drop them in this section.

With the help of two kind of unity matrices in the compound index

$$1^{\nu\nu'} \equiv 1^{\nu\nu'}_{lmm'l'} = \delta_{\nu\nu'}\delta_{ll'}\delta_{mm'} \tag{I.1a}$$

$$\vec{1}^{\nu'} \equiv \sum_{\nu} 1^{\nu\nu'} = \delta_{ll'}\delta_{mm'} \tag{I.1b}$$

we can derive a matrix implementation of the three-leg vertices. The completely local three-leg γ^{ω}_{r} can be calculated via

$$\begin{aligned}
\chi^{\omega\nu'\nu}_{r} &= \chi^{\omega\nu'\nu'}_{0} + \chi^{\omega\nu'\nu'}_{0} F^{\omega\nu'\nu}_{r} \chi^{\omega\nu\nu}_{0} \\
\chi^{\omega\nu'\nu}_{r} \left[\chi^{\omega\nu\nu}_{0}\right]^{-1} &= 1^{\nu'\nu} + \chi^{\omega\nu'\nu'}_{0} F^{\omega\nu'\nu}_{r} \\
\chi^{\omega\nu'\nu}_{r} \left[\chi^{\omega\nu\nu}_{0}\right]^{-1} - 1^{\nu'\nu} &= \chi^{\omega\nu'\nu'}_{0} F^{\omega\nu'\nu}_{r} \\
\sum_{\nu'} \left[\chi^{\omega\nu'\nu}_{r} \left[\chi^{\omega\nu\nu}_{0}\right]^{-1} - 1^{\nu'\nu}\right] &= \sum_{\nu'} \chi^{\omega\nu'\nu'}_{0} F^{\omega\nu'\nu}_{r} = \gamma^{\omega\nu}_{r}.
\end{aligned} \tag{I.2}$$

One 'non-local level' above that is the three-leg γ^{q}_{r} which can be calculated similarly via

$$\begin{aligned}
\gamma^{q\nu}_{r} &= \sum_{\nu'} \chi^{q\nu'\nu',\mathrm{nl}}_{0} F^{\omega\nu'\nu}_{r} \\
&= \sum_{\nu'} \left[\chi^{q\nu'\nu'}_{0} - \chi^{\omega\nu'\nu'}_{0}\right] F^{\omega\nu'\nu}_{r} \\
&= \sum_{\nu'} \left[\chi^{q\nu'\nu'}_{0} \left[\chi^{\omega\nu'\nu'}_{0}\right]^{-1} \chi^{\omega\nu'\nu'}_{0} - \chi^{\omega\nu'\nu'}_{0}\right] F^{\omega\nu'\nu}_{r} \\
&= \sum_{\nu'} \left[\chi^{q\nu'\nu'}_{0} \left[\chi^{\omega\nu'\nu'}_{0}\right]^{-1} - 1^{\nu'\nu'}\right] \chi^{\omega\nu'\nu'}_{0} F^{\omega\nu'\nu}_{r}.
\end{aligned} \tag{I.3}$$

The completely non-local, and most complex, three-leg η_r^q can be derived by

$$
\begin{aligned}
\eta_r^{q\nu} &= \sum_{\nu'} \chi_0^{q\nu'\nu'} F_r^{q\nu'\nu} - \sum_{\nu'} \chi_0^{\omega\nu'\nu'} F_r^{\omega\nu'\nu} \\
&= \sum_{\nu'} \chi_0^{q\nu'\nu'} \sum_{\nu''} \left[F_r^{\omega\nu'\nu''} + \sum_{\nu'''} 2\beta^{-2} V^{\mathbf{q}\nu'\nu'''} \left(1^{\nu'''\nu''} + \chi_0^{\omega\nu'''\nu'''} F_r^{\omega\nu'''\nu''} \right) \delta_{r,D} \right]^{q\nu'\nu''} \\
&\quad \left[\left[1^{\nu''\nu} - \chi_0^{q\nu''\nu'',\mathrm{nl}} F_r^{\omega\nu''\nu} - 2\beta^{-2} \sum_{\nu'''} \chi_0^{q\nu''\nu''} V^{\mathbf{q}\nu''\nu'''} \left(1^{\nu'''\nu} + \chi_0^{\omega\nu'''\nu'''} F_r^{\omega\nu'''\nu} \right) \delta_{r,D} \right]^{-1} \right]^{q\nu''\nu} - \gamma_r^{\omega\nu} \\
&= \sum_{\nu'} \chi_0^{q\nu'\nu'} \sum_{\nu''} \left[F_r^{\omega\nu'\nu''} + 2\beta^{-2} V^{\mathbf{q}\nu'} \left(\vec{1}^{\nu''} + \gamma_r^{\omega\nu''} \right) \delta_{r,D} \right]^{q\nu'\nu''} \\
&\qquad \left[\left[1^{\nu''\nu} - \chi_0^{q\nu''\nu'',\mathrm{nl}} F_r^{\omega\nu''\nu} - 2\beta^{-2} \chi_0^{q\nu''\nu''} V^{\mathbf{q}\nu''} \left(\vec{1}^{\nu} + \gamma_r^{\omega\nu} \right) \delta_{r,D} \right]^{-1} \right]^{q\nu''\nu} - \gamma_r^{\omega\nu} \\
&= \sum_{\nu',\nu''} \left[\chi_0^{\omega\nu'\nu'} F_r^{\omega\nu'\nu''} \right]^{\omega\nu'\nu''} \left[\left[1^{\nu''\nu} - \chi_0^{q\nu''\nu'',\mathrm{nl}} F_r^{\omega\nu''\nu} - 2\beta^{-2} \chi_0^{q\nu''\nu''} V^{\mathbf{q}\nu''} \left(\vec{1}^{\nu} + \gamma_r^{\omega\nu} \right) \delta_{r,D} \right]^{-1} \right]^{q\nu''\nu} \\
&+ \sum_{\nu',\nu''} \left[\chi_0^{q\nu'\nu',\mathrm{nl}} F_r^{\omega\nu'\nu''} + 2\beta^{-2} \chi_0^{q\nu'\nu'} V^{\mathbf{q}\nu'} \left(\vec{1}^{\nu''} + \gamma_r^{\omega\nu''} \right) \delta_{r,D} \right]^{q\nu'\nu''} \\
&\qquad \left[\left[1^{\nu''\nu} - \chi_0^{q\nu''\nu'',\mathrm{nl}} F_r^{\omega\nu''\nu} - 2\beta^{-2} \chi_0^{q\nu''\nu''} V^{\mathbf{q}\nu''} \left(\vec{1}^{\nu} + \gamma_r^{\omega\nu} \right) \delta_{r,D} \right]^{-1} \right]^{q\nu''\nu} - \gamma_r^{\omega\nu} \\
&= \sum_{\nu',\nu''} \left[\chi_0^{\omega\nu'\nu'} F_r^{\omega\nu'\nu''} \right]^{\omega\nu'\nu''} \left[\left[1^{\nu''\nu} - \chi_0^{q\nu''\nu'',\mathrm{nl}} F_r^{\omega\nu''\nu} - 2\beta^{-2} \chi_0^{q\nu''\nu''} V^{\mathbf{q}\nu''} \left(\vec{1}^{\nu} + \gamma_r^{\omega\nu} \right) \delta_{r,D} \right]^{-1} \right]^{q\nu''\nu} \\
&+ \sum_{\nu'} \left[\left[1^{\nu'\nu} - \chi_0^{q\nu'\nu',\mathrm{nl}} F_r^{\omega\nu'\nu} - 2\beta^{-2} \chi_0^{q\nu'\nu'} V^{\mathbf{q}\nu'} \left(\vec{1}^{\nu} + \gamma_r^{\omega\nu} \right) \delta_{r,D} \right]^{-1} - 1^{\nu'\nu} \right]^{q\nu'\nu} - \gamma_r^{\omega\nu} \\
&= \sum_{\nu''} \gamma_r^{\omega\nu''} \left[\left[1^{\nu''\nu} - \chi_0^{q\nu''\nu'',\mathrm{nl}} F_r^{\omega\nu''\nu} - 2\beta^{-2} \chi_0^{q\nu''\nu''} V^{\mathbf{q}\nu''} \left(\vec{1}^{\nu} + \gamma_r^{\omega\nu} \right) \delta_{r,D} \right]^{-1} \right]^{q\nu''\nu} \\
&+ \sum_{\nu''} \left[\vec{1}^{\nu''} \right] \left[\left[1^{\nu''\nu} - \chi_0^{q\nu''\nu'',\mathrm{nl}} F_r^{\omega\nu''\nu} - 2\beta^{-2} \chi_0^{q\nu''\nu''} V^{\mathbf{q}\nu''} \left(\vec{1}^{\nu} + \gamma_r^{\omega\nu} \right) \delta_{r,D} \right]^{-1} - 1^{\nu''\nu} \right]^{q\nu''\nu} - \gamma_r^{\omega\nu} \\
&= \sum_{\nu''} \left[\vec{1}^{\nu''} + \gamma_r^{\omega\nu''} \right] \left[\left[1^{\nu''\nu} - \chi_0^{q\nu''\nu'',\mathrm{nl}} F_r^{\omega\nu''\nu} - 2\beta^{-2} \chi_0^{q\nu''\nu''} V^{\mathbf{q}\nu''} \left(\vec{1}^{\nu} + \gamma_r^{\omega\nu} \right) \delta_{r,D} \right]^{-1} - 1^{\nu''\nu} \right]^{q\nu''\nu}.
\end{aligned}
\tag{I.4}
$$

where in the second to last equation we used

$$\sum_{\nu'} A^{\nu'\nu} = \sum_{\nu'\nu''} 1^{\nu'\nu''} A^{\nu''\nu} = \sum_{\nu''} \vec{1}^{\nu''} A^{\nu''\nu} \tag{I.5}$$

and

$$\sum_{\nu''} \gamma_r^{\omega\nu''} 1^{\nu''\nu} = \gamma_r^{\omega\nu}. \tag{I.6}$$

Summarized, out of the six three-leg vertices ($r \in [M, D]$)

$$\begin{aligned}
\gamma_r^{\omega\nu} &= \sum_{\nu'} \left[\chi_r^{\omega\nu'\nu} \left[\chi_0^{\omega\nu\nu} \right]^{-1} - 1^{\nu'\nu} \right] \\
\gamma_r^{q\nu} &= \sum_{\nu'} \left[\chi_0^{q\nu'\nu'} \left[\chi_0^{\omega\nu'\nu'} \right]^{-1} - 1^{\nu'\nu'} \right] \chi_0^{\omega\nu'\nu'} F_r^{\omega\nu'\nu} \\
\eta_r^{q\nu} &= \sum_{\nu''} \left[\vec{1}^{\nu''} + \gamma_r^{\omega\nu''} \right] \left[\left[1^{\nu''\nu} - \chi_0^{q\nu''\nu'',\mathrm{nl}} F_r^{\omega\nu''\nu} - 2\beta^{-2} \chi_0^{q\nu''\nu''} V^{\mathbf{q}\nu''} \left(\vec{1}^{\nu} + \gamma_r^{\omega\nu} \right) \delta_{r,D} \right]^{-1} - 1^{\nu''\nu} \right],
\end{aligned}$$

we have to construct five for a self-energy calculation (all except $\gamma_M^{q\nu}$) or four for a susceptibility calculation (all except $\gamma_M^{q\nu}$, $\gamma_D^{q\nu}$).

References

[1] J. Bardeen, L. N. Cooper, and J. R. Schrieffer, "Theory of Superconductivity," *Phys. Rev.*, vol. **108**, pp. 1175–1204, (1957).

[2] L. Landau, "The Theory of a Fermi Liquid," *Soviet Physics JETP Vol.* **3***, Number 6*, (1957).

[3] A. A. Abrikosov and I. M. Khalatnikov, "The theory of a fermi liquid (the properties of liquid ^{3}He at low temperatures)," *Reports on Progress in Physics*, vol. **22**, no. 1, p. 329, (1959).

[4] P. Hohenberg and W. Kohn, "Inhomogeneous Electron Gas," *Phys. Rev.*, vol. **136**, pp. B864–B871, (1964).

[5] W. Kohn and L. J. Sham, "Self-Consistent Equations Including Exchange and Correlation Effects," *Phys. Rev.*, vol. **140**, pp. A1133–A1138, (1965).

[6] W. Metzner and D. Vollhardt, "Correlated Lattice Fermions in $d = \infty$ Dimensions," *Phys. Rev. Lett.*, vol. **62**, pp. 324–327, (1989).

[7] A. Georges, "Strongly Correlated Electron Materials: Dynamical Mean-Field Theory and Electronic Structure," *AIP Conference Proceedings*, vol. **715**, no. 1, pp. 3–74, (2004).

[8] M. H. Hettler, M. Mukherjee, M. Jarrell, and H. R. Krishnamurthy, "Dynamical cluster approximation: Nonlocal dynamics of correlated electron systems," *Phys. Rev. B*, vol. **61**, pp. 12739–12756, (2000).

[9] A. I. Lichtenstein and M. I. Katsnelson, "Antiferromagnetism and d-wave superconductivity in cuprates: A cluster dynamical mean-field theory," *Phys. Rev. B*, vol. **62**, pp. R9283–R9286, Oct (2000).

[10] A. Toschi, A. A. Katanin, and K. Held, "Dynamical vertex approximation: A step beyond dynamical mean-field theory," *Phys. Rev. B*, vol. **75**, p. 045118, (2007).

[11] S. Brener, H. Hafermann, A. N. Rubtsov, M. I. Katsnelson, and A. I. Lichtenstein, "Dual fermion approach to susceptibility of correlated lattice fermions," *Phys. Rev. B*, vol. **77**, p. 195105, (2008).

[12] Y. Tokura and N. Nagaosa, "Orbital Physics in Transition-Metal Oxides," *Science*, vol. **288**, no. 5465, pp. 462–468, (2000).

[13] A. Nag and V. Shubha, "Oxide Thermoelectric Materials: A Structure–Property Relationship," *Journal of Electronic Materials*, vol. **43**, no. 4, pp. 962–977, (2014).

[14] G. Aeppli, C. Broholm, J. D. Tusa, S. Hayden, T. Ito, S.-H. Lee, T. Mason, H. Mook, K. Oka, T. Perring, A. Schröder, H. Takagi, and G. Xu, "Magnetic coherence in the transition metal oxides," *Physica B* **237 – 238** *30-35*, (1997).

[15] H. Maeda, Y. Tanaka, M. Fukutomi, and T. Asano, " A New High- T_c Oxide Superconductor without a Rare Earth Element," *Japanese Journal of Applied Physics*, vol. **27**, no. 2A, p. L209, (1988).

[16] A. Ohtomo and H. Y. Hwang, "A high-mobility electron gas at the $LaAlO_3/SrTiO_3$ heterointerface," *Nature volume* **427***, pages 423–426*, (2004).

[17] J. Zhou, Y. Gao, Z. Zhang, H. Luo, C. Cao, Z. C. andLei Dai, and X. Liu, "VO_2 thermochromic smart window for energy savings and generation," *Scientific Reports volume* **3***, Article number: 3029*, (2013).

[18] E. Assmann, P. Blaha, R. Laskowski, K. Held, S. Okamoto, and G. Sangiovanni, "Oxide Heterostructures for Efficient Solar Cells," *Phys. Rev. Lett.*, vol. 110, p. 078701, Feb 2013.

[19] L. Wang, Y. Li, A. Bera, C. Ma, F. Jin, K. Yuan, W. Yin, A. David, W. Chen, W. Wu, W. Prellier, S. Wei, and T. Wu, "Device Performance of the Mott Insulator $LaVO_3$ as a Photovoltaic Material," *Phys. Rev. Applied*, vol. **3**, p. 064015, (2015).

[20] A. Galler, P. Thunström, P. Gunacker, J. M. Tomczak, and K. Held, "Ab initio dynamical vertex approximation," *Phys. Rev. B*, vol. **95**, p. 115107, (2017).

[21] Z. Zhong, M. Wallerberger, J. M. Tomczak, C. Taranto, N. Parragh, A. Toschi, G. Sangiovanni, and K. Held, "Electronics with Correlated Oxides: $SrVO_3/SrTiO_3$ as a Mott Transistor," *Phys. Rev. Lett.*, vol. **114**, p. 246401, (2015).

[22] A. Galler, *Towards an ab initio treatment of materials with local and non-local electronic correlations*. PhD thesis, Vienna University of Technology, 2017.

[23] A. Galler, J. Kaufmann, P. Gunacker, M. Pickem, P. Thunström, J. M. Tomczak, and K. Held, "Towards ab initio Calculations with the Dynamical Vertex Approximation," *Journal of the Physical Society of Japan*, vol. **87**, no. 4, p. 041004, (2018).

[24] A. Galler, P. Thunström, J. Kaufmann, M. Pickem, J. Tomczak, and K. Held, "The AbinitioDΓA Project v1.0: Non-local correlations beyond and susceptibilities within dynamical mean-field theory," *arXiv:1710.06651*, 2017.

[25] Wikimedia Commons, "Simple periodic table chart," Sep, 9th 2017. File: `Simple Periodic Table Chart-en.svg`.

[26] H.-R. Wenk and A. Bulakh, *Minerals: Their Constitution and Origin*. Cambridge University Press, 2004.

[27] E. Pavarini, A. Yamasaki, J. Nuss, and O. K. Andersen, "How chemistry controls electron localization in 3d 1 perovskites: a Wannier-function study," *New J. Phys.* **7** *188*, (2005).

[28] E. Pavarini, *The LDA+DMFT approach to strongly correlated materials*, vol. 1 of *Schriften des Forschungszentrums Jülich : Modeling and Simulation*. Forschungszentrum Jülich GmbH Institute for Advance Simulations, 2011. Record converted from VDB: 12.11.2012.

[29] M. Born and R. Oppenheimer, "Zur Quantentheorie der Molekeln," *Annalen der Physik*, vol. **389**, no. 20, pp. 457–484, (1927).

[30] J. C. Slater, "A Simplification of the Hartree-Fock Method," *Phys. Rev.*, vol. **81**, pp. 385–390, (1951).

[31] L. H. Thomas, "The calculation of atomic fields," *Mathematical Proceedings of the Cambridge Philosophical Society*, vol. **23**, no. 5, p. 542–548, (1927).

[32] K. Burke, J. P. Perdew, and Y. Wang, *Derivation of a Generalized Gradient Approximation: The PW91 Density Functional*, pp. 81–111. Boston, MA: Springer US, 1998.

[33] J. P. Perdew, K. Burke, and M. Ernzerhof, "Generalized Gradient Approximation Made Simple," *Phys. Rev. Lett.*, vol. **77**, pp. 3865–3868, (1996).

[34] K. Kim and K. D. Jordan, "Comparison of Density Functional and MP2 Calculations on the Water Monomer and Dimer," *The Journal of Physical Chemistry*, vol. **98**, no. 40, pp. 10089–10094, (1994).

[35] P. J. Stephens, F. J. Devlin, C. F. Chabalowski, and M. J. Frisch, "Ab Initio Calculation of Vibrational Absorption and Circular Dichroism Spectra Using Density Functional Force Fields," *The Journal of Physical Chemistry*, vol. **98**, no. 45, pp. 11623–11627, (1994).

[36] P. Blaha, K. Schwarz, G.-K.-H. Madsen, D. Kvasnicka, and J. Luitz, "WIEN2k, An Augmented Plane Wave Plus Local Orbitals Program for Calculating Crystal Properties," *Vienna University of Technology, Austria*, 2001. ISBN 3-9501031-1-2.

[37] G. Kresse and J. Hafner, "Ab initio molecular dynamics for liquid metals," *Phys. Rev. B*, vol. **47**, pp. 558–561, (1993).

[38] G. Kresse and J. Furthmüller, "Efficient iterative schemes for ab initio total-energy calculations using a plane-wave basis set," *Phys. Rev. B*, vol. **54**, pp. 11169–11186, (1996).

[39] N. F. Mott, "The Basis of the Electron Theory of Metals, with Special Reference to the Transition Metals," *Proceedings of the Physical Society. Section A*, vol. **62**, no. 7, p. 416, (1949).

[40] Cyrot, M., "Theory of mott transition : Applications to transition metal oxides," *J. Phys. France*, vol. **33**, no. 1, pp. 125–134, (1972).

[41] W. F. Brinkman and T. M. Rice, "Application of Gutzwiller's Variational Method to the Metal-Insulator Transition," *Phys. Rev. B*, vol. **2**, pp. 4302–4304, (1970).

[42] N. Marzari, A. A. Mostofi, J. R. Yates, I. Souza, and D. Vanderbilt, "Maximally localized Wannier functions: Theory and applications," *Rev. Mod. Phys.*, vol. **84**, pp. 1419–1475, (2012).

[43] T. Miyake, F. Aryasetiawan, and M. Imada, "Ab initio procedure for constructing effective models of correlated materials with entangled band structure," *Phys. Rev. B*, vol. **80**, p. 155134, (2009).

[44] F. Aryasetiawan, M. Imada, A. Georges, G. Kotliar, S. Biermann, and A. I. Lichtenstein, "Frequency-dependent local interactions and low-energy effective models from electronic structure calculations," *Phys. Rev. B*, vol. **70**, no. 19, p. 195104, (2004).

[45] T. Miyake and F. Aryasetiawan, "Screened Coulomb interaction in the maximally localized Wannier basis," *Phys. Rev. B*, vol. **77**, no. 8, p. 085122, (2008).

[46] V. I. Anisimov and O. Gunnarsson, "Density-functional calculation of effective Coulomb interactions in metals," *Phys. Rev. B*, vol. **43**, no. 10, pp. 7570–7574, (1991).

[47] E. H. Lieb and F. Wu, "The one-dimensional Hubbard model: a reminiscence," *Physica A: Statistical Mechanics and its Applications*, vol. **321**, no. 1, pp. 1 – 27, (2003). Statphys-Taiwan-2002: Lattice Models and Complex Systems.

[48] A. Georges and G. Kotliar, "Hubbard model in infinite dimensions," *Phys. Rev. B*, vol. **45**, pp. 6479–6483, (1992).

[49] E. Gull, A. J. Millis, A. I. Lichtenstein, A. N. Rubtsov, M. Troyer, and P. Werner, "Continuous-time Monte Carlo methods for quantum impurity models," *Rev. Mod. Phys.*, vol. **83**, pp. 349–404, (2011).

[50] M. Wallerberger, A. Hausoel, P. Gunacker, A. Kowalski, F. G. Nicolaus Parragh, K. Held, and G. Sangiovanni, "w2dynamics: Local one- and two-particle quantities from dynamical mean field theory," *arXiv:1801.10209*, 2018.

[51] K. Held, "Electronic structure calculations using dynamical mean field theory," *Advances in Physics*, vol. **56**, no. 6, pp. 829–926, (2007).

[52] A. Abrikosov, L. Gorkov, and I. Dzyaloshinski, *Methods of quantum field theory in statistical physics*. Dover, 1975.

[53] A. L. Fetter and J. D. Walecka, *Quantum theory of many-particle systems*. Dover, 2002.

[54] R. D. Mattuck, *A guide to Feynman Diagrams in the Many-Body Problem*. Dover, 1992.

[55] G. Rohringer, *New routes towards a theoretical treatment of nonlocal electronic correlations*. PhD thesis, Vienna Unitversity of Technology, 2013.

[56] G. Rohringer, H. Hafermann, A. Toschi, A. A. Katanin, A. E. Antipov, M. I. Katsnelson, A. I. Lichtenstein, A. N. Rubtsov, and K. Held, "Diagrammatic routes to non-local correlations beyond dynamical mean field theory," *arXiv:1705.00024*, 2017.

[57] T. Matsubara, "A New Approach to Quantum-Statistical Mechanics," *Progress of Theoretical Physics*, vol. **14**, no. 4, pp. 351–378, (1955).

[58] D. Vollhardt, "Dynamical mean-field theory for correlated electrons," *Annalen der Physik*, vol. **524**, no. 1, pp. 1–19, (2012).

[59] J. Tomczak, *Spectral and optical properties of correlated materials*. PhD thesis, Ecole Polytechnique, Palaiseau, 2007.

[60] M. Jarrell and J. Gubernatis, "Bayesian inference and the analytic continuation of imaginary-time quantum Monte Carlo data," *Physics Reports*, vol. **269**, no. 3, pp. 133 – 195, (1996).

[61] K. S. D. Beach, R. J. Gooding, and F. Marsiglio, "Reliable Padé analytical continuation method based on a high-accuracy symbolic computation algorithm," *Phys. Rev. B*, vol. **61**, pp. 5147–5157, (2000).

[62] M. H. Hettler, A. N. Tahvildar-Zadeh, M. Jarrell, T. Pruschke, and H. R. Krishnamurthy, "Nonlocal dynamical correlations of strongly interacting electron systems," *Phys. Rev. B*, vol. **58**, pp. R7475–R7479, (1998).

[63] G. Rohringer, A. Valli, and A. Toschi, "Local electronic correlation at the two-particle level," *Phys. Rev. B*, vol. **86**, p. 125114, (2012).

[64] K.-M. Tam, H. Fotso, S.-X. Yang, T.-W. Lee, J. Moreno, J. Ramanujam, and M. Jarrell, "Solving the parquet equations for the Hubbard model beyond weak coupling," *Phys. Rev. E*, vol. **87**, p. 013311, (2013).

[65] A. Sekiyama, H. Fujiwara, S. Imada, S. Suga, H. Eisaki, S. I. Uchida, K. Takegahara, H. Harima, Y. Saitoh, I. A. Nekrasov, G. Keller, D. E. Kondakov, A. V. Kozhevnikov, T. Pruschke, K. Held, D. Vollhardt, and V. I. Anisimov, "Mutual Experimental and Theoretical Validation of Bulk Photoemission Spectra of $Sr_{1-x}Ca_xVO_3$," *Phys. Rev. Lett.*, vol. **93**, p. 156402, (2004).

[66] I. H. Inoue, O. Goto, H. Makino, N. E. Hussey, and M. Ishikawa, "Bandwidth control in a perovskite-type $3d^1$-correlated metal $Ca_{1-x}Sr_xVO_3$. I. Evolution of the electronic properties and effective mass," *Phys. Rev. B*, vol. **58**, pp. 4372–4383, Aug (1998).

[67] J. Kuneš, R. Arita, P. Wissgott, A. Toschi, H. Ikeda, and K. Held, "Wien2wannier: From linearized augmented plane waves to maximally localized Wannier functions," *Computer Physics Communications*, vol. **181**, no. 11, pp. 1888 – 1895, (2010).

[68] N. W. Ashcroft and D. N. Mermin, *Festkörperphysik*. Oldenbourg Verlag, 2012.

[69] I. A. Nekrasov, K. Held, G. Keller, D. E. Kondakov, T. Pruschke, M. Kollar, O. K. Andersen, V. I. Anisimov, and D. Vollhardt, "Momentum-resolved spectral functions of $SrVO_3$ calculated by LDA + DMFT," *Phys. Rev. B*, vol. **73**, p. 155112, (2006).

[70] J. Kanamori, "Superexchange interaction and symmetry properties of electron orbitals," *Journal of Physics and Chemistry of Solids*, vol. **10**, no. 2, pp. 87 – 98, (1959).

[71] A. Georges, L. de' Medici, and J. Mravlje, "Strong Correlations from Hund's Coupling," *Annual Review of Condensed Matter Physics*, vol. **4**, no. 1, pp. 137–178, (2013).

[72] T. Ribic, E. Assmann, A. Tóth, and K. Held, "Cubic interaction parameters for t_{2g} Wannier orbitals," *Phys. Rev. B*, vol. **90**, p. 165105, (2014).

[73] J. Kaufmann, P. Gunacker, and K. Held, "Continuous-time quantum Monte Carlo calculation of multiorbital vertex asymptotics," *Phys. Rev. B*, vol. **96**, p. 035114, Jul (2017).

[74] N. Mott, "Metal-Insulator Transition," *Rev. Mod. Phys.*, vol. **40**, pp. 677–683, (1968).

[75] K. Yoshimatsu, T. Okabe, H. Kumigashira, S. Okamoto, S. Aizaki, A. Fujimori, and M. Oshima, "Dimensional-Crossover-Driven Metal-Insulator Transition in $SrVO_3$ Ultrathin Films," *Phys. Rev. Lett.*, vol. **104**, p. 147601, (2010).

[76] K. Masaki, Y. Kohei, M. Taichi, K. Miho, S. Enju, Y. Ryu, M. Makoto, F. Atsushi, H. Koji, and K. Hiroshi, "Emergence of quantum critical behavior in metallic quantum-well states of strongly correlated oxides," *Scientific Reports* **7***, 16621*, (2017).

[77] P. Gunacker, M. Wallerberger, E. Gull, A. Hausoel, G. Sangiovanni, and K. Held, "Continuous-time quantum Monte Carlo using worm sampling," *Phys. Rev. B*, vol. **92**, p. 155102, (2015).

[78] S. Gull, *Maximum Entropy and Bayesian Methods*. Kluwer Academic Publishers, Dordrecht, 1989.

[79] J. M. Tomczak, P. Liu, A. Toschi, G. Kresse, and K. Held, "Merging GW with DMFT and non-local correlations beyond," *The European Physical Journal Special Topics*, vol. **226**, no. 11, pp. 2565–2590, (2017).

[80] L. Hedin, "New Method for Calculating the One-Particle Green's Function with Application to the Electron-Gas Problem," *Phys. Rev.*, vol. **139**, pp. A796–A823, (1965).

[81] F. Aryasetiawan and O. Gunnarsson, "The GW method," *Reports on Progress in Physics*, vol. **61**, no. 3, p. 237, (1998).

[82] T. Moriya, *Spin Fluctuations in Itinerant Electron Magnetism*. Springer-Verlag Berlin Heidelberg, 1985.

[83] T. Schäfer, S. Ciuchi, M. Wallerberger, P. Thunström, O. Gunnarsson, G. Sangiovanni, G. Rohringer, and A. Toschi, "Nonperturbative landscape of the Mott-Hubbard transition: Multiple divergence lines around the critical endpoint," *Phys. Rev. B*, vol. **94**, p. 235108, (2016).